

AD-A100 798

TECHNICAL
LIBRARY

AD

MEMORANDUM REPORT ARBRL-MR-03088
(Supersedes IMR No. 670)

HELICOPTER AND CABLE DROP TESTS OF A
MULTI-SENSOR YAWSONDE INSTRUMENTED
SADARM MODEL

V. Oskay
W. H. Mermagen

March 1981



US ARMY ARMAMENT RESEARCH AND DEVELOPMENT COMMAND
BALLISTIC RESEARCH LABORATORY
ABERDEEN PROVING GROUND, MARYLAND

Approved for public release; distribution unlimited.

DTIC QUALITY INSPECTED 3

Destroy this report when it is no longer needed.
Do not return it to the originator.

Secondary distribution of this report by originating
or sponsoring activity is prohibited.

Additional copies of this report may be obtained
from the National Technical Information Service,
U.S. Department of Commerce, Springfield, Virginia
22161.

The findings in this report are not to be construed as
an official Department of the Army position, unless
so designated by other authorized documents.

*The use of trade names or manufacturers' names in this report
does not constitute endorsement of any commercial product.*

UNCLASSIFIED

SECURITY CLASSIFICATION OF THIS PAGE (When Data Entered)

REPORT DOCUMENTATION PAGE		READ INSTRUCTIONS BEFORE COMPLETING FORM
1. REPORT NUMBER MEMORANDUM REPORT ARBRL-MR-03088	2. GOVT ACCESSION NO.	3. RECIPIENT'S CATALOG NUMBER
4. TITLE (and Subtitle) HELICOPTER AND CABLE DROP TESTS OF A MULTI-SENSOR YAWSONDE INSTRUMENTED SADARM MODEL		5. TYPE OF REPORT & PERIOD COVERED Final
		6. PERFORMING ORG. REPORT NUMBER
7. AUTHOR(s) V. Oskay W. H. Mermagen	8. CONTRACT OR GRANT NUMBER(s)	
9. PERFORMING ORGANIZATION NAME AND ADDRESS US Army Ballistic Research Laboratory ATTN: DRDAR-BLL Aberdeen Proving Ground, MD 21005	10. PROGRAM ELEMENT, PROJECT, TASK AREA & WORK UNIT NUMBERS 1X463628B276	
11. CONTROLLING OFFICE NAME AND ADDRESS US Army Armament Research & Development Command US Army Ballistic Research Laboratory ATTN: DRDAR-BL Aberdeen Proving Ground, MD 21005	12. REPORT DATE MARCH 1981	
	13. NUMBER OF PAGES 124	
14. MONITORING AGENCY NAME & ADDRESS (if different from Controlling Office)	15. SECURITY CLASS. (of this report) Unclassified	
	15a. DECLASSIFICATION/DOWNGRADING SCHEDULE	
16. DISTRIBUTION STATEMENT (of this Report) Approved for public release; distribution unlimited.		
17. DISTRIBUTION STATEMENT (of the abstract entered in Block 20, if different from Report)		
18. SUPPLEMENTARY NOTES Supersedes BRL IMR No. 670 dated January 1980.		
19. KEY WORDS (Continue on reverse side if necessary and identify by block number) Multi-Sensor Yawsondes Parachute Payloads Drop Tests Flight Dynamics Special Instrumentation		
20. ABSTRACT (Continue on reverse side if necessary and identify by block number) (caw) A series of helicopter and cable drops of a yawsonde-instrumented SADARM model were made at Sandia Laboratories in Albuquerque, NM. The program was designed to determine the flight behavior of the parachute/warhead system under conditions which would resemble both a real flight environment and a feasibility firing environment. It was hoped that the program would refine the cable drop technique for use in later live firings. About ninety percent of the helicopter and cable drops resulted in		

UNCLASSIFIED

SECURITY CLASSIFICATION OF THIS PAGE(When Data Entered)

20. ABSTRACT

successful deployment of the vortex-ring parachute and proper operation of the system. Tests with the 2.13-metre parachute show that steady-state spin is achieved about four seconds after release for both cable and helicopter drops. The average spin rate observed with this parachute is 4.7 rps \pm 0.1 rps. The yawsonde results showed that this particular model/parachute combination has a bi-modal yaw behavior. The slow mode has a frequency equal to the pendular frequency of the system (about 1.0 Hz). This mode seems to be excited by external forces such as wind shear. The fast mode has a frequency about equal to the steady-state spin rate (about 4.8 Hz) and this mode appears to be excited by the dynamics of the parachute/payload system. The fast mode does not appear to be damped. From the yawsonde data, the amplitude of yaw seems to be about 5.0 degrees.

Use of 1.83-metre parachute and smaller torque disk with this payload appears to increase the duration of the transitional time to about 7.5 seconds. Also, the average value of the steady-state spin is increased to 6.0 rps. The bi-modal behavior of the system remains unchanged although with the smaller parachute the frequency of the fast mode is increased to about 6 Hz. The slow mode remains unchanged.

UNCLASSIFIED

SECURITY CLASSIFICATION OF THIS PAGE(When Data Entered)

TABLE OF CONTENTS

	<u>Page</u>
LIST OF FIGURES	4
LIST OF TABLES	8
I. INTRODUCTION	9
II. MULTI-SENSOR SADARM MODELS.	10
III. CALIBRATION DATA	13
IV. TEST PROGRAM	16
A. Test Windows.	17
B. Helicopter Drops.	17
C. Cable Drops	21
V. TEST RESULTS	23
A. Transitional Behavior of the VRP.	23
B. Steady-State Spin Behavior.	26
C. Dynamic Behavior of the Warhead	28
VI. DISCUSSION	29
REFERENCES	58
LIST OF SYMBOLS	59
APPENDIX A	61
DETERMINATION OF SENSOR INSTALLATION ANGLES	
APPENDIX B	69
ADDITIONAL YAWSONDE PLOTS FOR CABLE DROPS	
APPENDIX C	101
TESTCASES FOR RESONANT MOTION	
DISTRIBUTION LIST	121

LIST OF FIGURES

<u>Figure</u>		<u>Page</u>
1	Photograph of original SADARM Model	31
2	Photograph of new SADARM Model	32
3	Schematic of Yawsonde Telemeter	33
4	Cross-Section of SADARM Yawsonde Model	34
5	Photograph of Lunar-Motion Calibrator	35
6	Dependence of SIGMA-N on Roll Angle for Sensor 1	36
7	Dependence of SIGMA-N on Roll Angle for Sensor 3	37
8	Dependence of SIGMA-N on Roll Angle for Sensor 5	38
9	Dependence of SIGMA-N on Roll Angle for Sensor 7	39
10	Altitude of Sun at Albuquerque, NM (12-6-78)	40
11	Spin Versus Time for Cable Drop 7 (from Yaw Sensors) .	41
12	Spin Versus Time for Cable Drop 7 (from Spin Sensors) .	42
13	Spin Versus Time for Cable Drop 18	43
14a	Spin Versus Time for Helicopter Drop 10 (3-15 sec) . .	44
14b	Spin Versus Time for Helicopter Drop 10 (14-25 sec) . .	45
14c	Spin Versus Time for Helicopter Drop 10 (24-35 sec) . .	46
14d	Spin Versus Time for Helicopter Drop 10 (35-46 sec) . .	47
15a	Spin Versus Time for Helicopter Drop 27 (2-12 sec) . .	48
15b	Spin Versus Time for Helicopter Drop 27 (11-27 sec) . .	49
16	Yaw Versus Time for Cable Drop 7	50
17	Yaw Versus Time for Cable Drop 18	51
18a	Yaw Versus Time for Helicopter Drop 10 (3-15 sec) . .	52
18b	Yaw Versus Time for Helicopter Drop 10 (14-25 sec) . .	53
18c	Yaw Versus Time for Helicopter Drop 10 (24-35 sec) . .	54

LIST OF FIGURES (continued)

<u>Figure</u>		<u>Page</u>
18d	Yaw Versus Time for Helicopter Drop 10 (35-46 sec)	55
19a	Yaw Versus Time for Helicopter Drop 27 (2-12 sec)	56
19b	Yaw Versus Time for Helicopter Drop 27 (11-20 sec)	57
A1	Canister Coordinate System	64
A2	Tilted Measurement System	65
A3	The Solar Vector in the Measurement Coordinate System	66
A4	Solar Aspect Angle as a Function of Roll Angle with γ as Parameter	67
B1	Spin Versus Time for Cable Drop 2	71
B2	Spin Versus Time for Cable Drop 5	72
B3	Spin Versus Time for Cable Drop 6	73
B4	Spin Versus Time for Cable Drop 8	74
B5	Spin Versus Time for Cable Drop 9	75
B6	Spin Versus Time for Cable Drop 10	76
B7	Spin Versus Time for Cable Drop 13	77
B8	Spin Versus Time for Cable Drop 14	78
B9	Spin Versus Time for Cable Drop 16	79
B10	Spin Versus Time for Cable Drop 17	80
B11	Spin Versus Time for Cable Drop 19	81
B12	Spin Versus Time for Cable Drop 27	82
B13	Yaw Versus Time for Cable Drop 2	83
B14	Yaw Versus Time for Cable Drop 5	84
B15	Yaw Versus Time for Cable Drop 6	85

LIST OF FIGURES (continued)

<u>Figure</u>		
B16	Yaw Versus Time for Cable Drop 8	86
B17	Yaw Versus Time for Cable Drop 9	87
B18	Yaw Versus Time for Cable Drop 10	88
B19	Yaw Versus Time for Cable Drop 13	89
B20	Yaw Versus Time for Cable Drop 14	90
B21	Yaw Versus Time for Cable Drop 16	91
B22	Yaw Versus Time for Cable Drop 17	92
B23	Yaw Versus Time for Cable Drop 19	93
B24	Yaw Versus Time for Cable Drop 27	94
B25	Spin Versus Time for Cable Drop 28	95
B26	Spin Versus Time for Cable Drop 30	96
B27	Yaw Versus Time for Cable Drop 28	97
B28	Yaw Versus Time for Cable Drop 30	98
B29	Spin Versus Time for Cable Drop 25	99
B30	Yaw Versus Time for Cable Drop 25	100
C1	Yaw Versus Time - Testcase 1 (Linear SIGMA, Quadratic PHI)	105
C2	Yaw Versus Time - Testcase 1 (Quadratic SIGMA, Linear PHI)	106
C3	Yaw Versus Time - Testcase 1 (Quadratic SIGMA, Quadratic PHI)	107
C4	Yaw Versus Time - Testcase 2 (Linear SIGMA, Quadratic PHI)	108
C5	Yaw Versus Time - Testcase 2 (Quadratic SIGMA, Linear PHI)	109
C6	Yaw Versus Time - Testcase 2 (Quadratic SIGMA, Quadratic PHI)	110

LIST OF FIGURES (continued)

<u>Figure</u>		<u>Page</u>
C7	Yaw Versus Time - Testcase 3 (Linear SIGMA, Quadratic PHI)	111
C8	Yaw Versus Time - Testcase 3 (Quadratic SIGMA, Linear PHI)	112
C9	Yaw Versus Time - Testcase 3 (Quadratic SIGMA, Quadratic PHI)	113
C10	Yaw Versus Time - Testcase 4 (Linear SIGMA, Quadratic PHI)	114
C11	Yaw Versus Time - Testcase 4 (Quadratic SIGMA, Linear PHI)	115
C12	Yaw Versus Time - Testcase 4 (Quadratic SIGMA, Quadratic PHI)	116
C13	Spin Versus Time - Testcase 4 (Linear SIGMA, Quadratic PHI)	117
C14	Spin Versus Time - Testcase 4 (Quadratic SIGMA, Linear PHI)	118
C15	Spin Versus Time - Testcase 4 (Quadratic SIGMA, Quadratic PHI)	119

LIST OF TABLES

<u>Table</u>		<u>Page</u>
1	SADARM Solar Cell Alignments	12
2	Mass Properties of SADARM Models	12
3	Calibration Data for SADARM Unit 3	14
4	Calibration Data for SADARM Unit 4	15
5	Altitude of the Sun at Albuquerque, NM (12-6-78) . .	18
6	Helicopter Drop Test Configurations	19
7	Log of SADARM Helicopter Drops	20
8	Log of SADARM Cable Drops	22
9	Parachute Performance from Cable Drops	24
10	Parachute Performance from Helicopter Drops	25

I. INTRODUCTION

During the past several years, the ARRADCOM has been developing a new improved sensing munition called SADARM (Sense And Destroy ARMor). The individual components which make up this munition have been tested separately and a theoretical system analysis has been performed.¹ The SADARM weapon consists of a self-forging-fragment warhead and a millimeter-wave radiometer contained within a canister which is suspended from a vortex-ring parachute (VRP). The axis of the warhead is kept at about 30° to the line of descent. The vortex-ring parachute forces the warhead to spin at a rate proportional to the descent velocity. As a result, the axis of the warhead traces out a helical path on the ground during descent. The antenna of the microwave radiometer is assembled so that the detector beam leads the warhead axis along the helical ground path. When the radiometer detects a metal surface on the ground, the firing logic is activated and the warhead functions.

Knowledge of the roll rate of the warhead as well as the amplitudes and frequencies of the motion of the system is important to a proper design of the firing logic and has bearing on the hit probability of the weapon. One method to determine the dynamic behavior of the system is to observe it under steady-state conditions in a vertical wind tunnel. During such tests, it is also possible to match the VRP to a particular payload. The Fluid Mechanics Branch of the Applied Sciences Division and the Electronics Devices Section of the Munitions Systems Division of the Large Caliber Weapon Systems Laboratory (LCWSL), ARRADCOM, at Dover, NJ, have been using the Air Force Vertical Tunnel Facility at Wright-Patterson AFB, Dayton, OH, for this purpose. Unfortunately, vertical wind tunnel tests have several shortcomings. They are performed under a constant dynamic head which corresponds to a steady-state descent of the system. Therefore, no dynamic behavior under unsteady conditions can be observed. Moreover, the directional instability of the vertical jet of the tunnel makes it necessary to position the parachute manually to keep it within the jet. Such manually induced disturbances may or may not simulate wind shear effects, but they cannot be used with any confidence to estimate the damping capabilities of the system. Finally, the test data consist of a movie film which is rather tedious to measure. Although a pair of orthogonal cameras were used on occasion, most of the test program used a single camera providing angular information only along one plane.

Because of the shortcomings of the vertical wind tunnel tests, the LCWSL asked the BRL to instrument two SADARM models with yawsondes.²

1. *P.H. Dietz, B.H. Rodin, and R.A. McGee, "SADARM System Simulation (U)", Ballistic Research Laboratory Report ARBRL-MR-02856, August 1978. AD C015654L.*
2. *W.H. Mermagen, V. Oskay, and J.W. Bradley, "Yawsonde Tests of SADARM Warhead at Sol Se Mete Canyon, Albuquerque, NM", Ballistic Research Laboratory Memorandum Report ARBRL-MR-02918, May 1979. AD B038263L.*

Originally, it had been planned that models would be dropped from a helicopter. In reality, the initial drop tests of instrumented models were made at the Aerial Cable Test Facility of Sandia Laboratories in the Sol Se Mete Canyon, Albuquerque, New Mexico. Due to technical, environmental, and analytical difficulties, the test results were not conclusive.²

Aerojet Electrosystem Company of Azusa, CA was under contract to LCWSL to perform a concept demonstration test with a live system during early 1979. In preparation for the demonstration tests, it became important to perform additional drop tests of instrumented SADARM models both from the Cable Facility and from helicopters to determine their dynamic behavior. Several major modifications to both the models and the test procedures were made based on the results of the previous test program. This report describes the second generation instrumented SADARM model, the test program, and some of the data.

II. MULTI-SENSOR SADARM MODELS

The instrumented SADARM model used during the first test program had four solar cells located at equally spaced intervals on its cylindrical surface², see Figure 1. Each solar sensor slit had been installed at an angle of 30° with respect to the axis of symmetry of the warhead rather than with respect to the system roll axis. As a result, two solar sensors could detect large amplitude yawing motions but were limited in accuracy. The other two solar cells had good measurement accuracy but were limited in the yawing amplitudes they could observe. This combination of solar cell characteristics limited both the test window and the usefulness of the data. During the analysis of the yawsonde records from the previous program, it was noticed that the yawing motion obtained from only one pair of sensors did not seem correct since both the yaw and the spin could vary during a single roll period (about 200 milliseconds). The condition of both yaw and spin changing during a measurement period violates the usual basic assumptions of the yawsonde reduction algorithm^{3,4}. An algorithm to reduce yawsonde data with large-amplitude yawing motions had been developed by Murphy⁵ but even this improvement required averaging over several revolutions with one pair of solar cells. If the data from all four sensors were used simultaneously, then only one revolution is needed

3. *W.H. Mermagen and W.H. Clay, "The Design of a Second Generation Yawsonde," Ballistic Research Laboratory Memorandum Report 2368, April 1974. AD 780064.*
4. *W.H. Mermagen, "Measurements of Dynamical Behavior of Projectiles over Long Flight Paths," Journal of Spacecraft and Rockets, Vol. 8, No. 4, April 1971, pp. 310-385.*
5. *C.H. Murphy, "Effect of Large High-Frequency Angular Motion of a Shell on the Analysis of its Yawsonde Records," Ballistic Research Laboratory Memorandum Report 2581, February 1976, AD B009421L.*

for the algorithm. This technique was used successfully in the previous program for the one test where all four sensors produced solar pulse data.²

Since the results of previous tests were limited and since a different size payload canister was to be used for the live demonstration tests, it was decided to build a new instrumented model and incorporate features which would minimize the previously encountered problems. This second generation model had eight solar cells arranged about its cylindrical surface in two tiers, Figure 2. The upper tier contained four sensors installed at equally spaced intervals and oriented with respect to the spin axis so as to provide yaw measurements. The orientation angles were selected to provide maximum angular sensitivity with an operational test window as wide as possible. The lower tier contained the remaining four sensors, also equally spaced but offset with respect to the upper tier. The lower four sensors were installed so that the slits would be parallel to the model roll axis and were intended to measure the spin of the system with a minimum of yaw modulation on the spin data. The optimum alignment of each sensor with respect to the warhead axis of symmetry was theoretically determined, see Appendix A, and a theoretical calibration curve for each yaw data channel was computed. The solar cell installation angles are given in Table 1:

The outputs of pairs of solar cells were made to modulate separate voltage controlled oscillators (VCO's) in such a fashion that the pulses would not overlap. Since the sensors were closely spaced about the periphery of the model, at certain angles of yaw the pulses from a yaw sensor could precede the pulses from the preceding spin sensor. To avoid ambiguity, the polarity of the pulses from one sensor into a given VCO were made positive while the pulses from the other sensor into the same VCO were made negative. The resultant telemeter, shown schematically in Figure 3, contained eight sensors, four VCO's (with hybrid amplifiers), a mixer-amplifier, and an L-Band transmitter. Rechargeable Nickel-Cadmium batteries with a voltage-regulator formed the power supply and a scimitar antenna was used to radiate the radio-frequency signal to the ground. The electronics were potted in polyurethane foam to protect against impact and to permit ready removal in case of failure.

Another constraint of the design was to match the mass properties of the Aerojet design so that no scaling or adjustment of the yawsonde data would be needed in predicting the behavior of the Aerojet system. The most stringent requirement for the design was that the polar and transverse moments of inertias be equal to within one percent. Figure 4 shows a sketch of the final design for the instrumented SADARM models. A comparison of the mass properties of the required design, Aerojet Mass Model No. 002, and the two BRL-built units is given in Table 2.

TABLE 1. SADARM Solar Cell Alignments

<u>Solar Cell Number</u>	<u>Usage</u>	<u>Polarity</u>	<u>VCO Frequency (kHz)</u>	<u>Alignment Angle</u>
1	Yaw	+	93	+14°
2	Spin	+	70	-30°
3	Yaw	+	52.5	-56°
4	Spin	+	40	0°
5	Yaw	-	52.5	+56°
6	Spin	-	40	+30°
7	Yaw	-	93	-14°
8*	Spin	-	70	0°

*On the same side as the clevis and in line with it.

TABLE 2. Mass Properties of SADARM Models

	<u>Weight (Kg)</u>	<u>c.g. (mm from top)</u>	<u>Moments of Inertia (Kg-m²)</u>		
			<u>Polar</u>	<u>Transverse I</u>	<u>Transverse II</u>
Design Goal	15.42	93.2	.09511	.09511	.09511
Aerojet Model	15.42	93.88	.10149	.10222	.10409
BRL Model No. 3	15.68	97.16	.10402	.10536	.10532
BRL Model No. 4	15.56	96.82	.10371	.10527	.10517

Note: Transverse Moment of Inertia I is along the clevis axis whereas Transverse II is normal to it.

III. CALIBRATION DATA

The SADARM warhead, constrained to an inclination of 30° with respect to the roll axis, executes lunar motion during descent. That is, as the warhead rotates about the spin axis, one face is always pointing toward the spin axis. Consequently, a different calibration procedure from the standard yawsonde calibration is required. The usual yawsonde calibration⁶ is done by a rotation of the yawsonde about its axis of symmetry, taking note of the roll angles at which the sensors see the light beam for various orientations of the light with respect to the sonde. A calibration for lunar motion, however, requires that the model be rotated about an axis which is not the axis of symmetry (in the case of SADARM - 30° off the axis of symmetry).

For the SADARM calibration, a special fixture was designed to perform a lunar motion calibration. Figure 5 is a photograph of one of the BRL SADARM models mounted on the special calibrator. An existing Schlieren optical system was used to provide a parallel light beam 30-cm in diameter, large enough for the sensors to remain within the beam during all calibration angles. The instrumented SADARM model was mounted on a machine indexing head at 30° tilt angle to simulate the drop conditions of the unit. The indexing head was capable of being rotated about its axis while tilting toward and away from the light source so that the model will perform a lunar motion within the light beam. The tilt angle between the rotational axis of the indexing head and the light beam corresponds to the complementary solar aspect angle SIGMA-N which is the angle between the sun and a normal to the system roll axis. During the calibration, for each value of SIGMA-N (or indexing-head tilt angle), the model is rotated 360° so that each sensor would see the light source. The roll angles at which the sensors detect the light for that value of SIGMA-N are recorded. A listing of these roll angles for each sensor as functions of SIGMA-N form the raw calibration data. Tables 3 and 4 contain these data for SADARM yawsonde units 3 and 4, respectively.

6. W.H. Clay, "A Precision Yawsonde Calibration Technique", Ballistic Research Laboratory Memorandum Report 2263, January 1973, AD 758158.

TABLE 3. Calibration Data for SADARM Unit 3

Solar Cell	Angles of Maximum Signal							
	1	2	3	4	5	6	7	8
VCO Freq.	93	70	52.5	40	52.5	40	93	70
<u>SIGMA-N</u>								
0	63.0	6.7	340.7	277.1	217.1	187.3	131.8	97.3
5	59.5	6.85	342.4	278.5	210.9	187.3	135.1	96.3
10	55.6	7.3	345.9	278.3	207.75	187.35	138.5	96.4
15	52.4	7.3	348.8	278.0	204.7	187.3	142.0	96.9
20	48.3	6.4	352.25	278.2	201.3	187.6	145.6	96.85
25	43.7	6.2	355.5	277.3		187.4	149.8	97.1
30	39.8	6.7	359.5	277.3		186.8	153.7	96.9
35	33.6	6.2	363.5	276.1		186.8	159.3	97.1
40	27.85	6.65	370.3	277.2		186.5	164.9	96.75
45	19.25	6.7				186.15	173.0	97.0
50	6.3	5.95				185.75	181.5	96.15
55	-21.3	6.4				184.7	195.45	96.7
60		4.8				184.4		95.9
65		4.85				184.6		94.35
70		3.85				181.8		94.6
75		2.15						94.25

TABLE 4. Calibration Data for SADARM Unit 4

Solar Cell	Angles of Maximum Signal							
	1	2	3	4	5	6	7	8
VCO Freq.	93	70	52.5	40	52.5	40	93	70
<u>SIGMA-N</u>								
0	58.85	4.7	336.0	274.5	212.6	184.3	129.7	94.5
5	56.0	4.8	339.4	274.3	209.55	184.1	132.7	94.2
10	52.75	4.7	342.4	273.9	206.15	184.2	135.7	94.5
15	49.3	4.8	346.1	274.1	202.3	184.3	139.4	94.35
20	45.7	4.95	349.55	274.1	198.8	184.6	142.7	94.3
25	41.5	4.65	353.25	273.75	194.5	184.55	146.8	94.3
30	37.4	4.8	357.8	273.9	189.9	184.0	150.8	94.1
35	32.5	5.35	362.55	273.2	184.8	183.55	155.6	94.5
40	26.9	6.3	368.05	274.35	178.3	183.2	161.05	94.6
45	18.6	6.3	375.3	274.2		182.0	169.3	94.75
50	5.5	5.9		272.9		182.8	179.1	94.4
55	-19.35	6.4				181.5	191.95	94.5
60		6.3				182.3		94.1
65		7.15				181.7		93.95
70		10.6				178.0		93.8
75		11.0				177.0		93.6

The data in Tables 3 and 4 show that the roll angle is almost independent of SIGMA-N for the spin sensors (2, 4, 6 and 8) as expected. The slight functional dependence is due to imprecision in the installation of the sensors and the fact that the sensors have a finite field of view. The functional behaviors of the yaw sensors (1, 3, 5 and 7) are seen in the graphs of Figures 6 - 9. The calibration data from SADARM unit 4 are shown as open circles while the dashed curves are the predicted calibrations computed according to Appendix A. The agreement is quite good and the differences are attributed to the precision of installation of the sensors. The full functional range of the theoretical calculation was not achieved because of the low level of light available during calibration. Finally, it should be noted that sensor 5 of unit 3 (see Table 3) could not be calibrated past SIGMA-N of 20° due to the low light sensitivity of that sensor.

The roll angle versus SIGMA-N calibration data are used with an extended Murphy's algorithm to reduce the flight data. A conventional yawsonde reduction could also be done using pairs of sensors such as 1 and 3 or 1 and 5. This method would be valid if the roll rate is reasonably constant during a revolution and the yaw varies only slightly during the same period. The raw calibration data would then be adjusted in the following manner. The fractional difference (x/y) for each pair of sensors considered is formed by the difference between roll angles for those two sensors divided by 360° at each value of SIGMA-N. These fractional differences are then used as functions of SIGMA-N and compared to the time difference in flight data for the sensors in question divided by the roll period. It has already been shown² that this approach does not work well for the SADARM system.

IV. TEST PROGRAM

The SADARM drop tests described in this report were done to provide a preliminary evaluation of the dynamic behavior of the 223 mm (8.8 inches) model used with a 2.13 m (7-foot) vortex-ring parachute in both canyon and open environments. The SADARM-concept live demonstration was scheduled to be performed under canyon conditions using the active warhead. It was important to determine the system behavior under a minimal environmental influence and the effects of the canyon environment on system performance.

Helicopter drops from a 915 m (3000-foot) height were included in the tests to measure the system behavior without the influence of the canyon environment. The helicopter drops were done over an open, high desert terrain. The canyon drops were done at the Aerial Cable Test Facility, SLA. Since the operation of the yawsonde depends on

available sunlight, the time of day and the weather conditions were critical factors in the successful performance of the test program. Because of these weather and sun position requirements, five working days were scheduled for each test phase although only twenty drops at each site were planned.

A. Test Windows

The data shown in Figures 6 - 9 indicate that the calibrations become non-linear for SIGMA-N larger than 40° . The sensors themselves cannot detect the sun if SIGMA-N is greater than about 60° . Tables 3 and 4 show that the spin sensors can detect the sun at values of SIGMA-N up to 75° . Unfortunately, the functional dependence of SIGMA-N on roll angle for the spin sensors is quite strong and small fluctuations in roll angle give large variations in SIGMA-N. Thus, the spin sensors are not appropriate for obtaining yaw determinations despite the apparent attractiveness of the extremely wide coverage these sensors provide.

The unperturbed trajectory of a SADARM drop is vertical; therefore, the solar aspect angle for zero yaw is the same as the elevation (or altitude) of the sun above the horizon. Table 5 shows the elevation of the sun at half-hour intervals throughout the day at Albuquerque, NM for 6 December 1978. The elevation of the canyon wall (which varies in height with azimuth) for various times of day (i.e., azimuthal positions of the sun) is also tabulated. Figure 10 shows these data graphically. As seen in Table 5, the maximum altitude of the sun is 32.6° at the test site in early December. This is well within the observation range of the SADARM yawsondes and it is possible to test the yawsonde-instrumented models on flat terrain anytime during the working day. During canyon drops, however, the local elevation of the canyon walls must be considered lest they block the sun. The elevation of the canyon walls, as seen in Table 5 and Figure 10*, indicate that the tests should be performed between 0900 and 1500 MST.

B. Helicopter Drops

After the original yawsonde test program, LCWSL and Aerojet made several changes to the basic test model. These changes involved moments of inertia and parachute dimensions and resulted in three different test configurations as shown in Table 6.

*Data provided by D.S. McDonald of Aerojet Electrosystems Company of Azusa, California.

TABLE 5. Altitude of the Sun at Albuquerque, NM
(12-6-78)

ZULU	TIME	MST	ELEVATION ANGLE (DEG)	
			SOLAR	CANYON WALLS
1500		0800	9.8	19.6
1530		1830	14.6	19.0
1600		0900	19.0	18.5
1630		0930	22.9	18.2
1700		1000	26.3	17.5
1730		1030	29.0	16.5
1800		1100	31.0	14.2
1830		1130	32.2	10.5
1900		1200	32.6	7.8
1930		1230	32.0	7.0
2000		1300	30.6	6.5
2030		1330	28.4	6.5
2100		1400	25.5	7.6
2130		1430	22.0	14.5
2200		1500	17.9	17.2
2230		1530	13.4	18.8
2300		1600	8.6	20.0
2330		1630	3.4	24.0
2400		1700	-2.0	25.6

TABLE 6. Helicopter Drop Test Configurations

Configuration	Number of Drops	$I_x = I_y$	VRP	Cup	BRL Unit
I	10	Yes	2.13m	.20 m	3
II	5	No	2.13m	.17 m	4
III	5	Yes	1.83m	.17 m	4

All drops will be made from 915 m height.

The helicopter drops were scheduled to take place during the week of 4 December 1978. On 4 December, five preliminary drops were made to check instrumentation as well as the release technique. For the laser tracker data to have a correct range reference, it was required that the test be started at a pre-surveyed point. From the pre-surveyed point the model is tracked to the drop site and then to impact. The only release method which could be used was a parachute bag attached to the helicopter's external, quick-release mechanism. Test drops of instrumented models were performed on December 5th and 8th. Poor weather prevented testing on December 6th and 7th.

Table 7 contains a log of the helicopter drops. The extended test window made it possible to perform 21 drops during the two test days. Transmitted data were obtained for all drops but on three of the drops the parachute did not deploy. The deployment failure of drop 16 can be attributed to high winds prevalent on the 8th of December. Because of the winds, the remainder of the drops on that date were done from an altitude of 610 meters. During drop 18 it was not possible to release the parachute at the preselected drop altitude but, by helicopter maneuvering, it was possible to release the model during helicopter descent. The payload was almost lost. The modified link used during drops 24 and 26 was designed by LCWSL engineers in an attempt to reduce payload oscillations. The modification effectively changes the plane of application of the VRP torque from one parallel to the clevis axis to a plane normal to that axis.

TABLE 7. Log of SADARM Helicopter Drops

<u>Date</u>	<u>Drop Number</u>	<u>Unit Number</u>	<u>Drop Time (MST)</u>	<u>VRP Size(m)</u>	<u>Cup Size(m)</u>	<u>Remarks</u>
12-5-78	6A	3	-----	2.13	.20	No release
	6B	3	11:10	2.13	.20	
	7	4	11:31	2.13	.17	Poor drop
	8	4	12:27	2.13	.20	
	9	3	13:06	2.13	.17	
	10	4	13:26	2.13	.20	
	11	3	13:53	2.13	.17	
	12	4	14:26	2.13	.20	Poor drop
	13	3	15:34	2.13	.17	Cloudy sky
	14	4	16:02	2.13	.20	Cloudy sky
	15	3	16:29	2.13	.17	Cloudy sky
12-8-78	16	3	11:17	2.13	.20	Poor drop, high winds
	17	4	11:45	2.13	.20	Reduce height to 610 m
	18	3	-----	2.13	.20	Release on descent
	19	4	12:37	2.13	.20	
	20	3	12:56	2.13	.20	
	21	4	13:25	2.13	.20	
	22	3	13:49	2.13	.20	
	23	4	14:50	1.83	.17	
	24	3	15:04	2.13	.20	Modified link
	25	4	15:23	1.83	.17	
	26	3	16:09	2.13	.20	Modified link
	27	4	16:35	1.83	.17	

C. Cable Drops

A test program using configurations similar to those shown in Table 6 was also planned for the cable site. Since the maximum drop height from the cable fixture is about 200 m, LCWSL engineers decided to use a pre-deployed vortex-ring parachute. The pre-deployed chute would also eliminate the deployment problems encountered in the May 1978 test series². A log of the cable drops is shown in Table 8.

A total of 37 drops were made at the Aerial Cable Facility of SLA during 11 - 13 December 1978. Eight of these drops used an uninstrumented mass model built by Aerojet Electrosystems Company. This model is designated AJ2 in Table 8. All drops with AJ2 used a 2.13 m parachute and a 0.20 m cup. All drops seemed to perform successfully. The purpose of these drops was to extend the statistical base for the pre-deployed launch condition. The remaining drops used two BRL-instrumented models. The yawsondes transmitted properly during all drops but three parachutes did not perform properly. These poor deployments may be in part attributable to the gusty wind environment of the canyon. A fourth unit deployed late in the drop.

The canyon environment presents several other difficulties in addition to the wind problem. There is always a possibility that the model will impact the canyon walls. The ground near the impact area is replete with trenches to contain instrumentation cables. These trenches, covered with steel plates, make the canyon impact area more hazardous for model survival than the helicopter drop area. SLA attempted to minimize this danger by using a catcher attached to a truck. Unfortunately, the unpredictability of the canyon winds made the catcher an additional hazard. Several transmitter antennas were damaged upon impact and had to be replaced during the test. The only major damage occurred when Unit 3 hit the edge of the catcher at the end of drop 10. The eight screws holding the canister top cover were sheared off and the transmitter-antenna cable was severed. Fortunately, the transmitter was not damaged and the unit was repaired overnight. Another unexpected problem occurred during drop 8 when the receiver of the laser tracker was inadvertently exposed to the sun. The intensity of the solar radiation damaged the tracker photomultiplier. Thus, most of the photographic coverage for 12 December was obtained with hand-held cameras. The laser tracker was operational only for drops 24 - 27.

The modified link used during drops 28 and 30 was the same one used during the helicopter drops 24 and 26. The sleeve used during drops 32 - 37 was the result of an effort to minimize the wind effects on the VRP at the moment of release. The panels of the pre-deployed parachute are subject to wind buffeting prior to and during release. The sleeve is designed to encase the parachute prior to release. Unfortunately, the limited number of drops with the sleeve did not permit an assessment of the effectiveness of the device, particularly in light of the fact that wind gusts as high as 30 mph were recorded on December 13th.

TABLE 8. Log of SADARM Cable Drops

<u>Date</u>	<u>Drop Number</u>	<u>Unit Number</u>	<u>Drop Time (MST)</u>	<u>VRP Size (m)</u>	<u>Cup Size (m)</u>	<u>Remarks</u>
12-11-78	1	AJ2	11:10	2.13	.20	
	2	3	11:51	2.13	.20	
	3	4	12:12	2.13	.17	Poor drop
	4	3	12:39	2.13	.20	Questionable drop
	5	4	13:04	2.13	.17	
	6	3	13:35	2.13	.20	
	7	4	13:53	2.13	.20	
	8	3	14:27	2.13	.17	
	9	4	14:45	2.13	.20	
	10	3	15:05	2.13	.17	
12-12-78	11	AJ2	15:22	2.13	.20	
	12	AJ2	15:37	2.13	.20	
	13	4	10:14	2.13	.20	
	14	3	10:31	2.13	.17	
	15	4	10:47	2.13	.20	
	16	3	11:02	2.13	.17	
	17	4	11:17	2.13	.20	
	18	3	11:44	1.83	.17	
	19	4	12:03	2.13	.20	
	20	3	12:18	1.83	.17	
	21	4	12:47	1.83	.17	
	22	3	13:02	2.13	.20	
	23	4	13:17	1.83	.17	
	24	3	13:31	2.13	.20	
	25	4	13:49	1.83	.17	
	26	3	14:03	2.13	.20	
	27	4	14:19	2.13	.20	
	28	3	14:34	2.13	.20	Modified link
12-13-78	29	4	14:50	2.13	.17	Poor Drop
	30	3	15:08	2.13	.20	Modified link
	31	AJ2	15:20	2.13	.20	
	32	AJ2	15:30	2.13	.20	Sleeve Drop
	33	AJ2	11:25	2.13	.20	
	34	AJ2	11:45	2.13	.20	Sleeve Drop
	35	AJ2	12:12	2.13	.20	Sleeve Drop
	36	4	12:28	2.13	.20	Sleeve Drop, Poor Drop
	37	3	12:54	2.13	.20	Sleeve Drop

V. TEST RESULTS

The test program produced large quantities of yawsonde, photographic, and laser tracker data. These data, in a somewhat reduced form, can give an indication of the performance of the prototype SADARM system. Ultimately it would be desireable to obtain the ground trace of the SADARM seeker for each drop, but the data reduction and analysis to reach this goal is formidable; therefore, only yawsonde results will be presented in this report. Data will be presented on:

- (a) the VRP behavior with respect to transition time to steady state,
- (b) the steady-state spin behavior of the system and
- (c) the steady-state yawing behavior of the warhead.

The primary purpose of the test program was to measure the behavior of the SADARM system with a 223 mm payload under the canyon environment so that performance information could be obtained prior to a live warhead demonstration. Thus, the steady state performance at the cable site is of primary interest. The comparison of the cable site transitional behavior to that of helicopter drops is of engineering interest since helicopter drops may more realistically simulate the deployment from an artillery shell.

A. Transitional Behavior of the VRP

The transitional regime for the SADARM experiment is the time between parachute release and steady state conditions. After the parachute is released, a finite time elapses during which the VRP deploys and begins to spin. The spin gradually increases until steady state is achieved. The time at which the parachute begins to spin can be observed from the yawsonde data, for those units instrumented with sondes. Similarly, the yawsonde data also show when steady state spin has been achieved. At the test site, SLA provided discriminators and a strip chart recorder so that the data from each yawsonde sensor could be displayed during the drop. Time zero was taken as the time when the explosive cutter on the cable fixture was initiated to release the parachute. Until the model begins to spin, only random pulses will issue from the yawsonde solar cells. After the parachute starts to spin, a regular pattern of pulses will be observed and the time between these pulses will change slowly until steady-state. Thus, the site records provide the times for start of spin and for steady-state. Tables 9 and 10 are tabulations of these observed times for both cable and helicopter drops, respectively. The time to steady state spin is the average of data from all four spin sensors.

A close examination of Tables 9 and 10 shows several interesting features of parachute deployment:

TABLE 9. Parachute Performance From Cable Drops

Date	Drop No.	Unit No.	VRP (m)	Cup (m)	First Signal T _f (sec)		Steady State T _s (sec)	Impact Time(sec)	$\Delta t = T_s - T_f$ (sec)
12-11-78	1	AJ2	2.13	.20			3.80	11.1	1.85
	2	3	2.13	.20	1.95				---
	3	4	2.13	.17	2.56			9.1	---
	4	3	2.13	.20	1.55		4.53	10.4	2.98
	5	4	2.13	.17	1.27		4.50	11.1	3.23
	6	3	2.13	.20	1.25		2.75	11.4	1.50
	7	4	2.13	.20	1.38		3.80	11.8	2.42
	8	3	2.13	.17	1.88		3.69	11.5	1.81
	9*	4	2.13	.20	0.17(?)		3.77(?)	10.9(?)	3.60
	10	3	2.13	.17	1.45		3.52	11.4	2.07
	11	AJ2	2.13	.20					
	12	AJ2	2.13	.20					
12-12-78	13	4	2.13	.20	1.52		3.68	11.9	2.16
	14	3	2.13	.17	1.14		3.00	11.5	1.86
	15	4	2.13	.20	1.59		4.46	11.8	2.87
	16	3	2.13	.17	1.30		3.28	11.7	1.98
	17	4	2.13	.20	1.52		5.13	12.0	3.61
	18	3	1.83	.17	1.61		5.79	10.4	4.18
	19	4	2.13	.20	1.24		5.16	11.5	3.92
	20	3	1.83	.17	1.37		4.65	10.7	3.28
	21	4	1.83	.17	1.56		6.52	10.8	4.96
	22	3	2.13	.20	1.44		5.42	11.9	3.98
	23	4	1.83	.17	2.62		6.72	11.0	4.10
	24	3	2.13	.20	1.17		4.84	11.3	3.67
	25	4	1.83	.17	2.34		6.40	10.3	4.06
	26	3	2.13	.20	0.94		4.57	11.4	3.63
	27	4	2.13	.20	1.33		4.59	11.6	3.26
	28**	3	2.13	.20	1.58		4.24	11.6	2.66
	29	4	2.13	.17	1.41			8.6	---
	30**	3	2.13	.20	1.29		4.09	11.7	2.80

* No Release Signal on SLA chart.

** Modified Link.

† Sleeve Drop.

TABLE 10. Parachute Performance From Helicopter Drops

Date	Drop No.	Unit No.	VRP (m)	Cup (m)	First Signal, T _f (sec)	Steady State, T _s (sec)	Impact Time(sec)	$\Delta t = T_s - T_f$ (sec)
12-5-78	6	3	2.13	.20	2.43	3.73	---	1.30
	7	4	2.13	.17	1.96	12.23	31.8	12.21
	8	4	2.13	.20	3.79	4.99	56.1	1.20
	9	3	2.13	.17	7.78	9.58	60.8	1.80
	10	4	2.13	.20	2.20	4.05	59.6	1.85
	11	3	2.13	.17	2.20	3.45	56.0	1.25
	12	4	2.13	.20	3.52	---	30.2	---
	13	3	2.13	.17	0.44	2.21	56.0	1.77
	14	4	2.13	.20	2.23	4.44	57.8	2.21
	15	3	2.13	.17	2.34	4.04	55.9	1.70
	16	3	2.13	.20	5.44	---	28.9	---
12-8-78	17*	4	2.13	.20	1.97	3.00	38.9	1.03
	18**	3	2.13	.20	2.66	4.04	35.1	1.38
	19	4	2.13	.20	14.98	16.48	45.9	1.50
	20	3	2.13	.20	1.82	3.32	35.6	1.50
	21	4	2.13	.20	2.95	4.00	39.7	1.05
	22	3	2.13	.20	9.47	12.76	44.1	3.29
	23	4	1.83	.17	2.13	3.06	36.6	1.16
	24†	3	2.13	.20	1.90	3.86	31.5	2.22
	25	4	1.83	.17	1.64	3.39	35.8	1.09
	26†	3	2.13	.20	2.30	3.97	32.7	2.44
	27	4	1.83	.17	1.53	---	---	---

* Drop altitude reduced to 610 m from 915 m due to high winds.

** Released during helicopter descent. No record.

† Modified link.

(1) The start of spin, determined from the first observed yawsonde pulse, is much more consistent at the cable site than for the helicopter drops. The standard deviation in start time for the 2.13-metre parachute at the cable site is 0.24 second compared to 0.72 second for the helicopter tests. This difference is partially attributed to the automatic release mechanism at the cable facility in comparison to the manual release on the helicopter. The difference is even more pronounced for three specific helicopter drops where the starting times were 7.78, 9.47 and 14.98 seconds.

(2) The average time to the start of spinning motion is the second difference between the two sites. At the cable site, the average time was 1.41 seconds. The helicopter drops showed an average 2.23 seconds before the initial detection of yawsonde pulses. This could be attributed to two factors: the initial air density for the helicopter drops was lower because of the increased altitude and the helicopter release was from a bag while the cable drops were from a pre-deployed configuration.

(3) The time required to reach steady-state spin also seems to be a function of test site. These times are shown as Δt in the Tables. At the cable site, steady-state spin is achieved within 2.8 seconds after the beginning of spin, on the average. On the other hand, less than 1.5 seconds is required to steady-state spin at the helicopter site. At both sites, however, it is interesting to note that the time from release to steady-state spin is about four (4) seconds.

All the above observations apply to the 2.13-metre VRP. Some 1.83-metre VRP's were also tested, but it is difficult to draw any conclusions because of the limited number of drops (3 at the helicopter site and 5 at the cable site). It is possible, however, to state that the smaller VRP takes longer to reach steady-state spin after the beginning of rotation. This increased time is about 1.5 seconds at both test sites and is due to the lower torque transmitted to the payload by the combination of smaller VRP and torque disk.

B. Steady-State Spin Behavior

Preliminary analyses of the yawsonde data from most of the cable drops and two helicopter drops (numbers 10 and 27) have been made. This section discusses the spin behavior. The next section will treat the flight behavior. Data from cable drops 7 and 18 and helicopter drops 10 and 27 will be used to demonstrate the salient aspects of the system's performance. The remaining yawsonde plots are shown in Appendix B.

The spin of the model can be determined in two ways: data from the spin sensors can give the spin directly or data from the yaw sensors

can produce the spin after treatment with Murphy's algorithm⁷. Figure 11 shows the spin data from the yaw sensors for cable drop 7. The spin is not observed until VRP had developed sufficient torque to drive the payload. Thus, the spin data do not start at the release time but several seconds later. Once the system begins to spin, some time is required to reach steady state (the region between 3 and 4 seconds). After 4 seconds into the flight a steady-state spin of 4.7 rps is observed. The data show a periodic modulation of the spin similar to the modulations which have been observed before⁵ whenever yaw sensors are used to compute spin. A unique peculiarity of these data, however, is that the modulation is at the same rate as the average spin rate. Figure 12 shows a similar plot of spin obtained from the spin sensors. The average spin rate is still 4.7 rps but the amplitude of the modulation is reduced. Nevertheless, the rate of the spin modulation is the same as the average spin rate.

Figure 13 shows the spin history of cable drop 18. For this drop, a 1.83-metre VRP was used. Several differences are obvious when compared to the previous two plots. The initial data point occurs at about 4 seconds into the flight indicating that the smaller parachute would require higher dynamic pressures than the 2.13-metre VRP to develop similar torque values. Secondly, the smaller parachute requires a longer drop time to reach the steady state conditions. The elapsed time is over 6 seconds. Finally, the average value of steady-state spin is about 6.0 rps, once more, indicating that the smaller parachute needs higher drop velocities to achieve the required torque since the spin rate of a VRP is linearly proportional to its descent velocity.

Figures 14a through 14d show the spin history of the helicopter drop 10 for the first 45 seconds of its flight. For this test, the model was released at 915 metres and a 2.13-metre VRP was used. The initial data point does not occur until 3 - 4 seconds into the drop. The steady state is achieved at about 5 seconds. The average spin rate is 4.8 rps. This value of spin persists throughout the remainder of the drop. The spin data from this helicopter drop also show a persistent modulation of the spin at a frequency equal to the average spin rate. In addition, a slow frequency modulation of some amplitude is also observed to occur sporadically. The slow modulation rate appears to be between 0.5 and 1.0 Hz.

The spin history corresponding to a helicopter drop with 1.83-metre VRP, drop number 27, is shown in Figures 15a and 15b for the first

7. J.W. Bradley, W.H. Mermagen, and V. Oskay, "Yawsonde Reduction for Slow-Rolling Vehicles." Proceedings of AIAA Atmospheric Flight Mechanics Conference, August 1979.

20 seconds of this model's descent. Due to the prevailing wind conditions, this drop was made from 610-metre altitude. Figure 15a shows that the first data point is observed at about 2 seconds and the steady-state spin is reached about 4.5 seconds into the drop. The average steady-state value of spin is 5.9 rps. Once more, the spin history is dominated by a fast frequency modulation at the same rate as the average spin. Similar to the spin of helicopter drop 10, it is possible to detect a low frequency modulation as well, although for this drop it is not as pronounced.

C. Dynamic Behavior of the Warhead

A yawsonde measures the flight behavior of a test vehicle in a plane defined by the sun and the roll axis of the model³⁻⁵. The measurement made by the yawsonde is the complementary solar aspect angle, σ_N , between the solar ray and the normal to the roll axis. While these measurements provide a good qualitative indication of the model's behavior, and some bounds on the motion can be established, a complete picture of the model's motion requires elaborate analysis based on a mathematical model for the mechanics of the system. Such a model does not exist, as yet, for the SADARM system.

Figure 16 shows σ_N as a function of flight time for the cable drop 7. There are no yawsonde data prior to 3 seconds since a minimum of one revolution in roll is required. A bi-modal behavior of the payload/parachute system is observed in this plot. The fast yaw rate is seen to be at 4.8 Hz, quite close to the average spin rate of 4.7 rps. The peak-to-peak amplitude of this component is about 5 degrees. The slow frequency mode is about 1.25 Hz which corresponds to the pendular rate of the parachute/warhead system. The slow mode also has a peak-to-peak amplitude of 5 degrees.

Flight behavior of the cable drop 18 is shown in Figure 17. Although there appears to be yawsonde data prior to 6.5 seconds, no credence could be placed to this portion of the plot since the system had not achieved steady-state conditions as yet. The region of the data between 7 and 10 seconds again shows the bi-modal behavior of this system. In contrast to the cable drop 7, this drop is dominated by the fast frequency (6.0 Hz) mode. The measured maximum amplitude of this mode is 14 degrees peak-to-peak. Around 9 seconds, a sizable slow mode appears. It is expected that this is due to the system traversing a region of wind shear near the canyon floor. The large amplitude of the fast mode shown in this plot appears to be a peculiarity of drop rather than the warhead with the 1.83-metre VRP (see Appendix B).

Figures 18a through 18d are the yawsonde results for helicopter drop 10. The data cover the first 45 seconds of the drop. As was the

case with the cable drops, the plots show a bi-modal behavior. A small amplitude (about 2 degrees peak-to-peak) fast mode persists throughout the entire drop. The frequency of this mode is somewhat less than 5 Hz and is comparable to the average spin rate of 4.8 rps. The fast mode amplitude appears to remain constant during the drop. The amplitude of the slow mode varies considerably. The peak-to-peak amplitude fluctuates from 6 degrees at 13, 33, and 41 seconds to 13 degrees at 19 and 34 seconds. The slow mode frequency seems to lie between 0.5 and 1.0 Hz.

The yawing motion of the helicopter drop 27 (using 1.83-metre VRP) is depicted in Figures 19a and 19b for the first 20 seconds of the drop. Once more, the motion indicated prior to 5 seconds should be ignored since the system had not achieved its steady behavior as yet. The motion between 5 and 20 seconds is again bi-modal. Similar to helicopter drop 10, this flight also shows a persistent small amplitude fast mode. The slow frequency mode is the prominent feature of the motion. But for this round, the maximum peak-to-peak amplitude remained below 12 degrees.

At present, drops 10 and 27 are the only helicopter drops which have been reduced. On the other hand, yawsonde data from most of the cable drops were reduced. Those data are colated in Appendix B.

VI. DISCUSSION

Because of a favorable altitude of the winter sun, it was possible to perform a large number of test drops at both the helicopter and cable sites. The predeployed parachute setup at the cable site worked well about 90 percent of the time. The bag release system for the helicopter drops worked reliably over 80 percent of the time. Some of the failures in helicopter drops can be attributed to the release mechanism while other failures are attributable to unfavorable prevalent wind conditions.

All the successful drops of the 2.13-metre VRP at the cable site required an average of 1.4 ± 0.25 seconds to start spinning. The helicopter drops required a longer time, about 2.25 ± 0.75 seconds. This difference in spin start time may be due to the difference in initial air density between the helicopter and the cable drops. As a result, a higher drop velocity is needed from the helicopter to achieve the same dynamic head as the cable-site drops. However, this increased drop velocity results in a shorter time to reach steady-state conditions after the start of spin (1.5 seconds for the helicopter versus 2.8 seconds for cable drops). This combination results in a total time to steady-state after release of 3.8 seconds for helicopter drops and 4.2 seconds for cable drops. The times in both cases are average with a standard deviation of 0.75 second.

The spin data for both cable and helicopter drops show a rapid spin-up to steady-state values. The data (Figures 11, 12, and Appendix B) show small-amplitude spin oscillations. The 2.13-metre parachute drops gave spin rates between 4.5 and 4.8 rps.

The motion of the parachute/warhead combination has two observable frequencies. The slow frequency is at about 1 Hertz and should correspond to the pendular frequency of the system. It is conjectured that this component is excited by winds during the descent of the warhead. The second, fast frequency is approximately equal to the system spin rate. This mode appears to have a constant amplitude throughout the drop while the amplitude of the slow mode varies. For each drop, the average solar aspect angle corresponds closely with the altitude of the sun for the time of day that the drop was made. It should be noted that, for no yawing motion, the solar aspect angle σ_N is the altitude (or elevation) of the sun at the time of drop. Changes in the attitude of the model result in oscillations about this value.

Since the yawing motion seems to have a component at the spin rate, the question of whether the instrumentation can observe such a motion arose. A further question on the accuracy of the yaw amplitude measurements should also be considered for this case. To determine the system measurement capability and accuracy, several test cases were generated on the computer (see Appendix C) and reduced using Murphy's extended algorithm. The test cases show that the present SADARM instrumentation can detect motions with frequencies equal to the spin rate. If the test case motion has an amplitude of 5 degrees peak-to-peak, the ability of the instrumentation and the computational algorithm to replicate the motion seems to have an accuracy of about ± 1 degree. At present, the cause of the fast frequency motion is not known. Some probable dynamic models are being investigated.

ACKNOWLEDGEMENTS

The efforts of W.H. Clay and S. Kushubar of the Launch and Flight Division, BRL, in measuring and reducing the yawsonde data contributed significantly to the results obtained in this program. The assistance of Sandia Laboratories during the field test phase of the program is gratefully acknowledged.

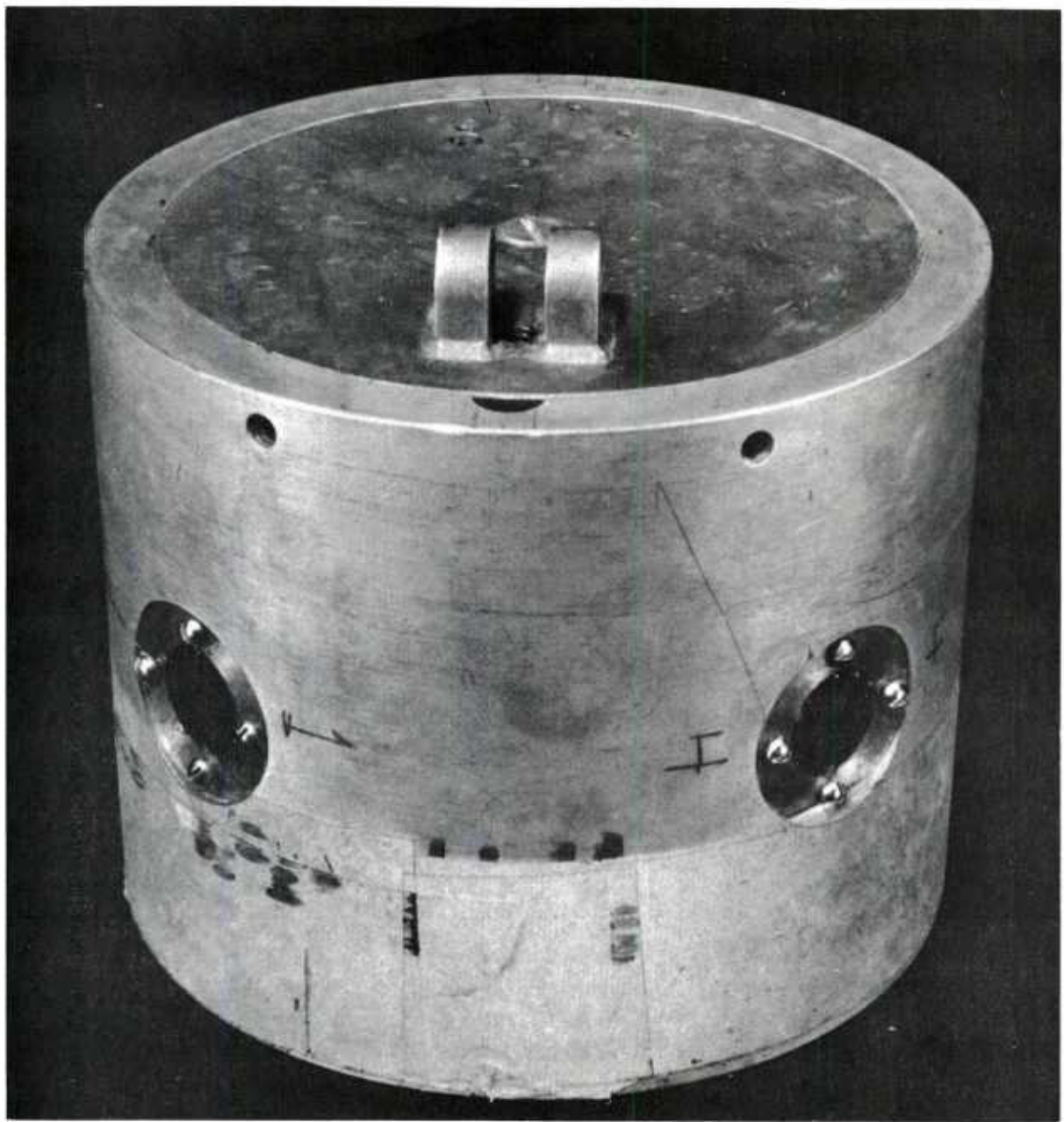


Fig. 1. Photograph of original SADARM Model



Fig. 2. Photograph of new SADARM Model

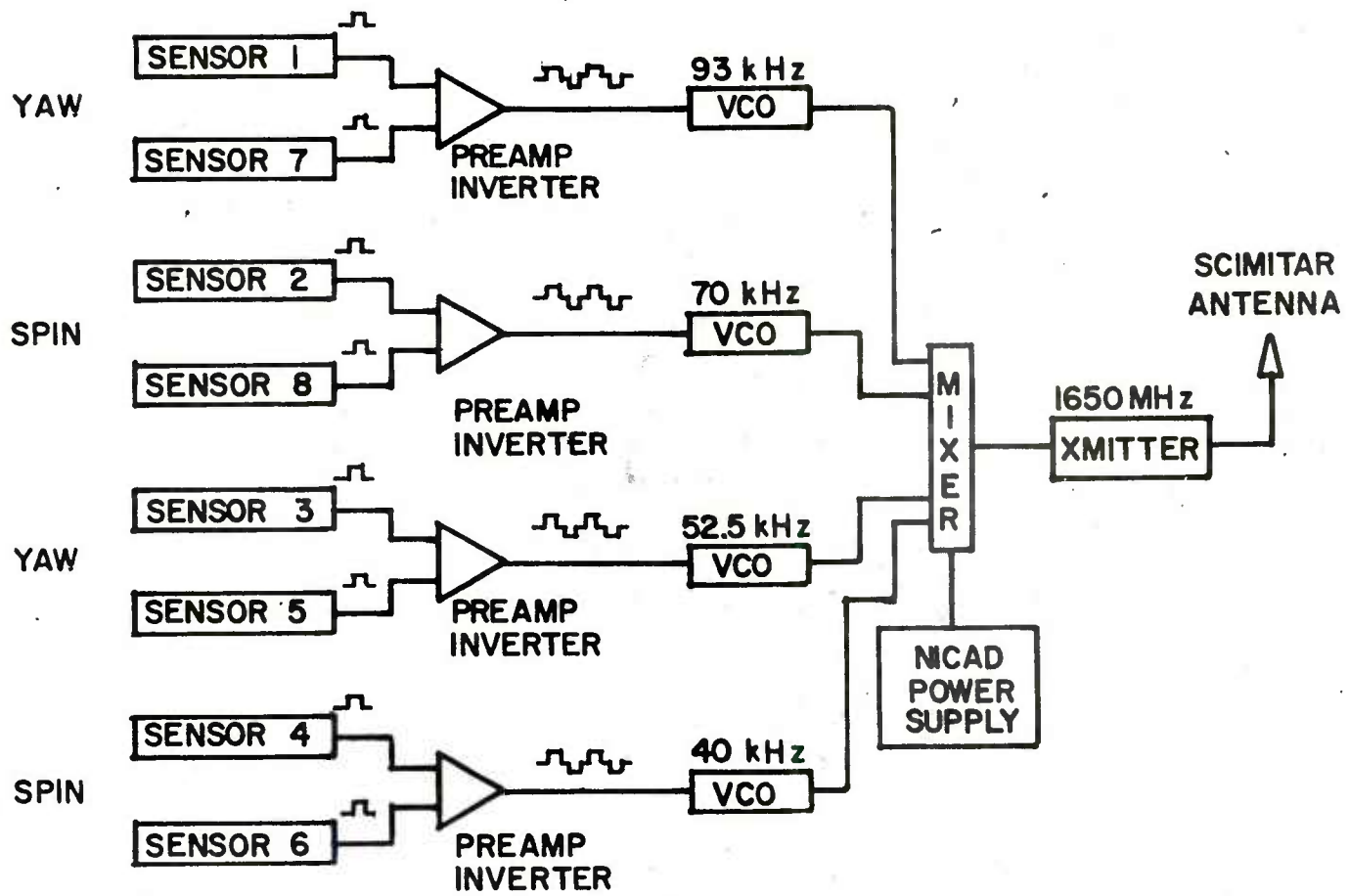


Fig. 3. Schematic of Yawsonde Telemeter

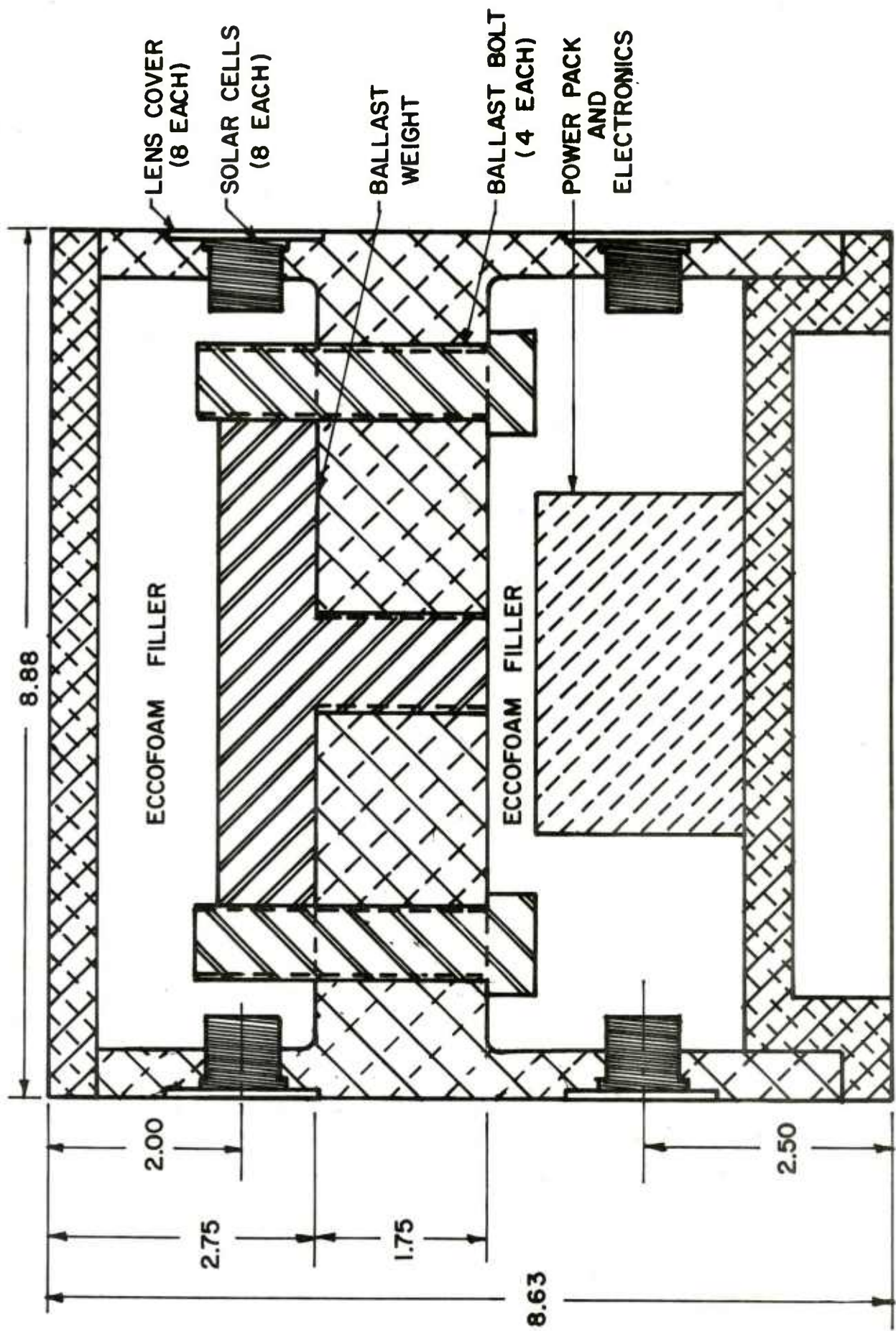


FIGURE 4. CROSS-SECTION OF SADARM YAWSONDE MODEL

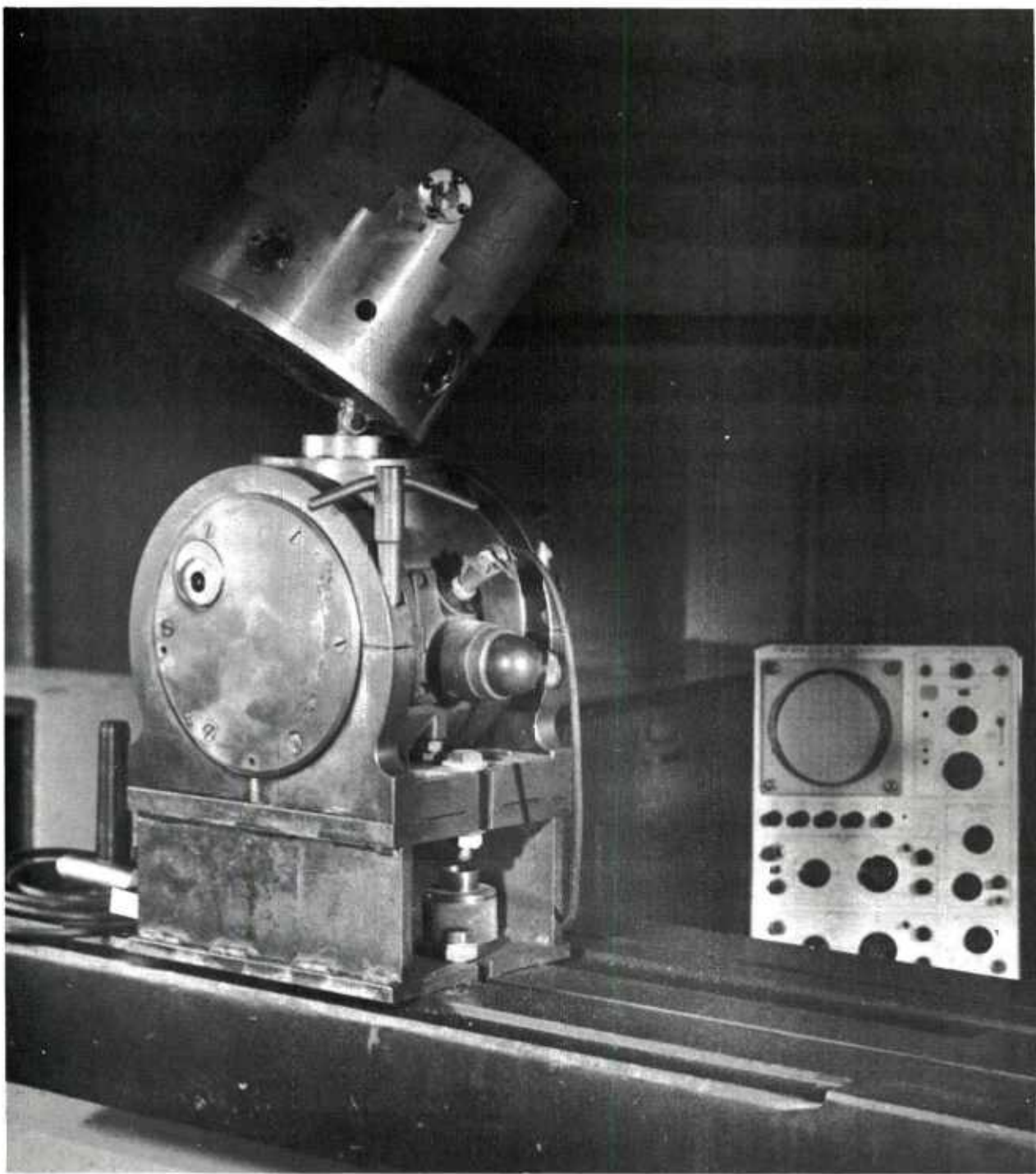


Fig. 5. Photograph of Lunar-Motion Calibrator

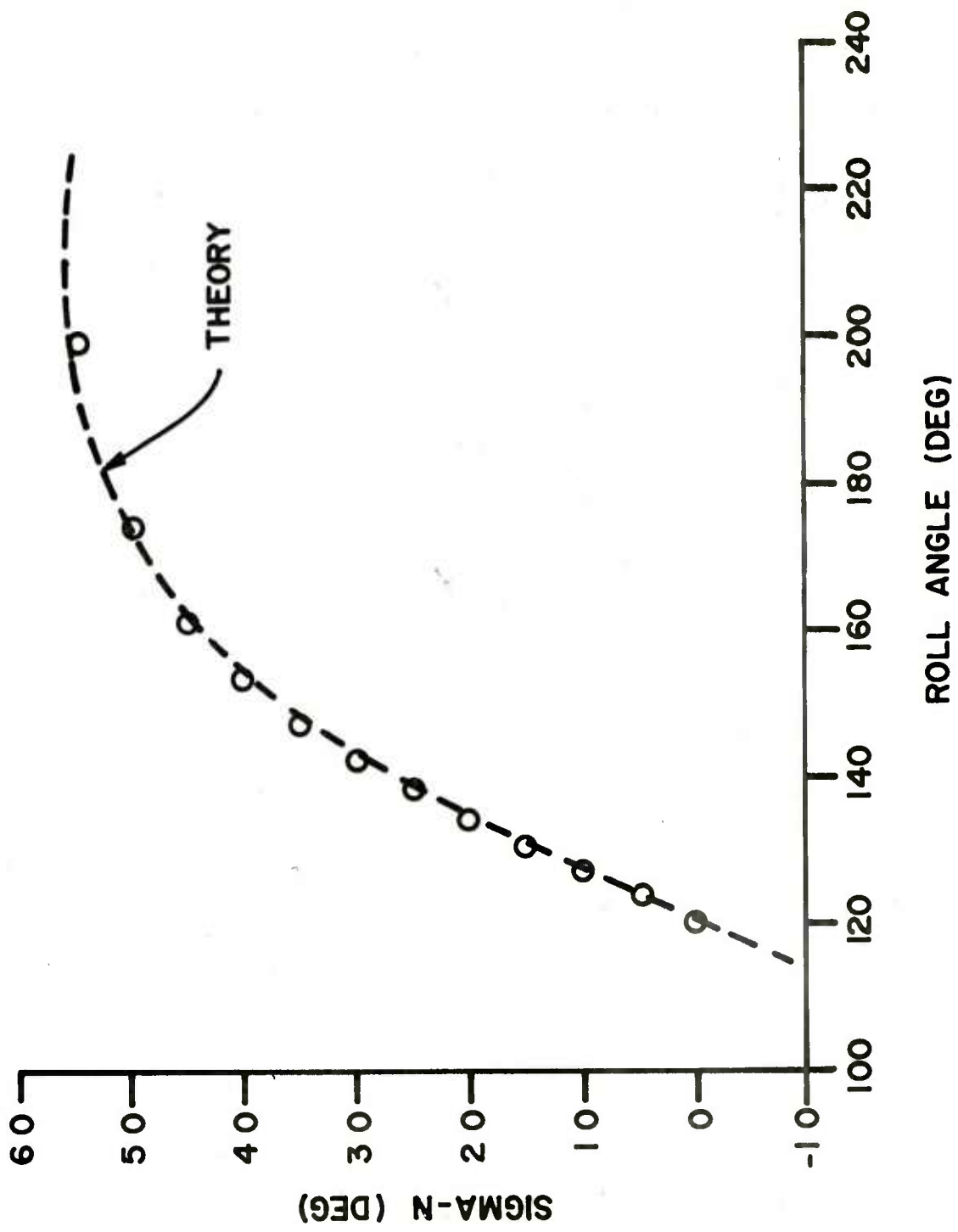


FIGURE 6. DEPENDENCE OF SIGMA-N ON ROLL ANGLE FOR SENSOR 1

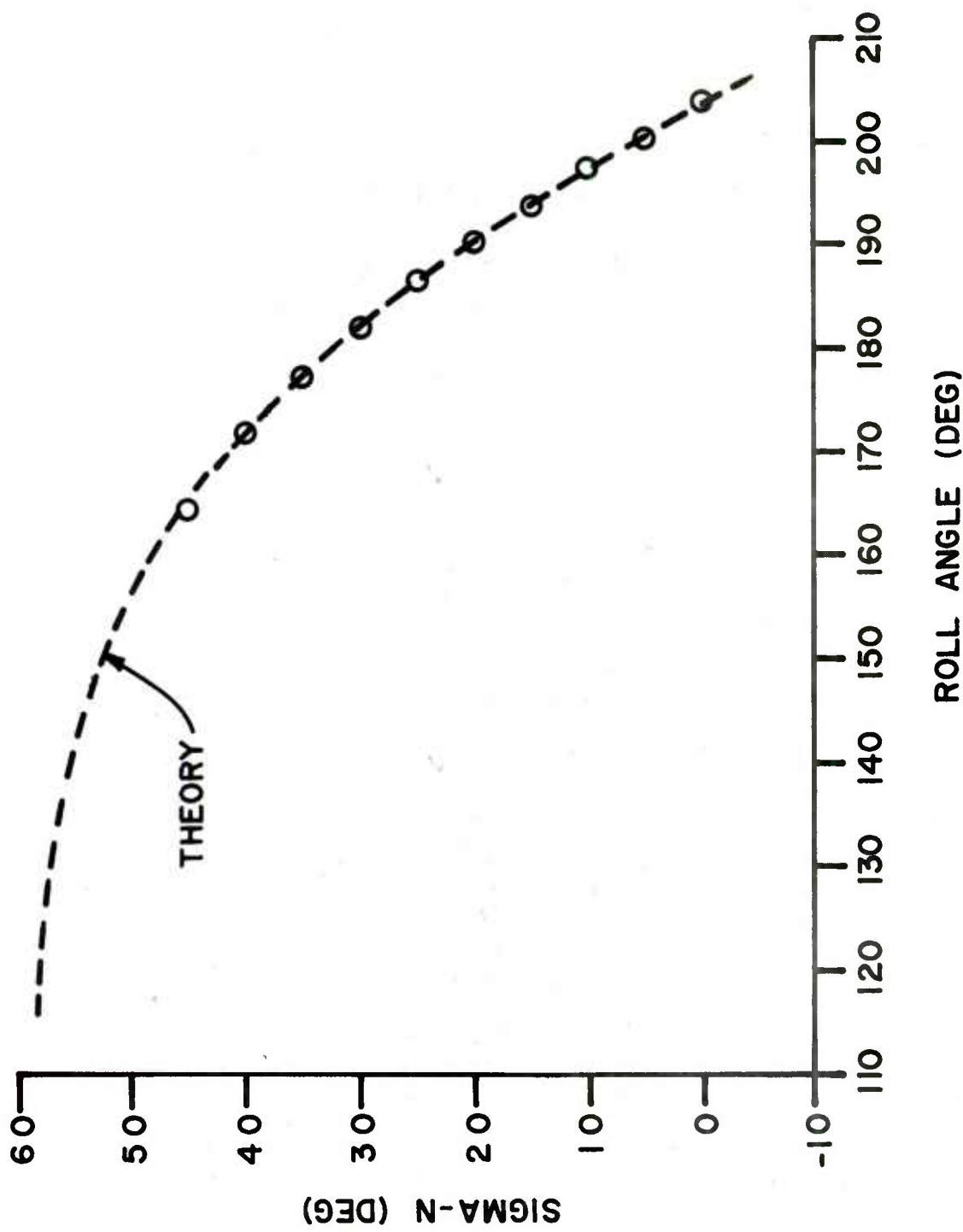


FIGURE 7. DEPENDENCE OF Σ_N ON ROLL ANGLE FOR SENSOR 3

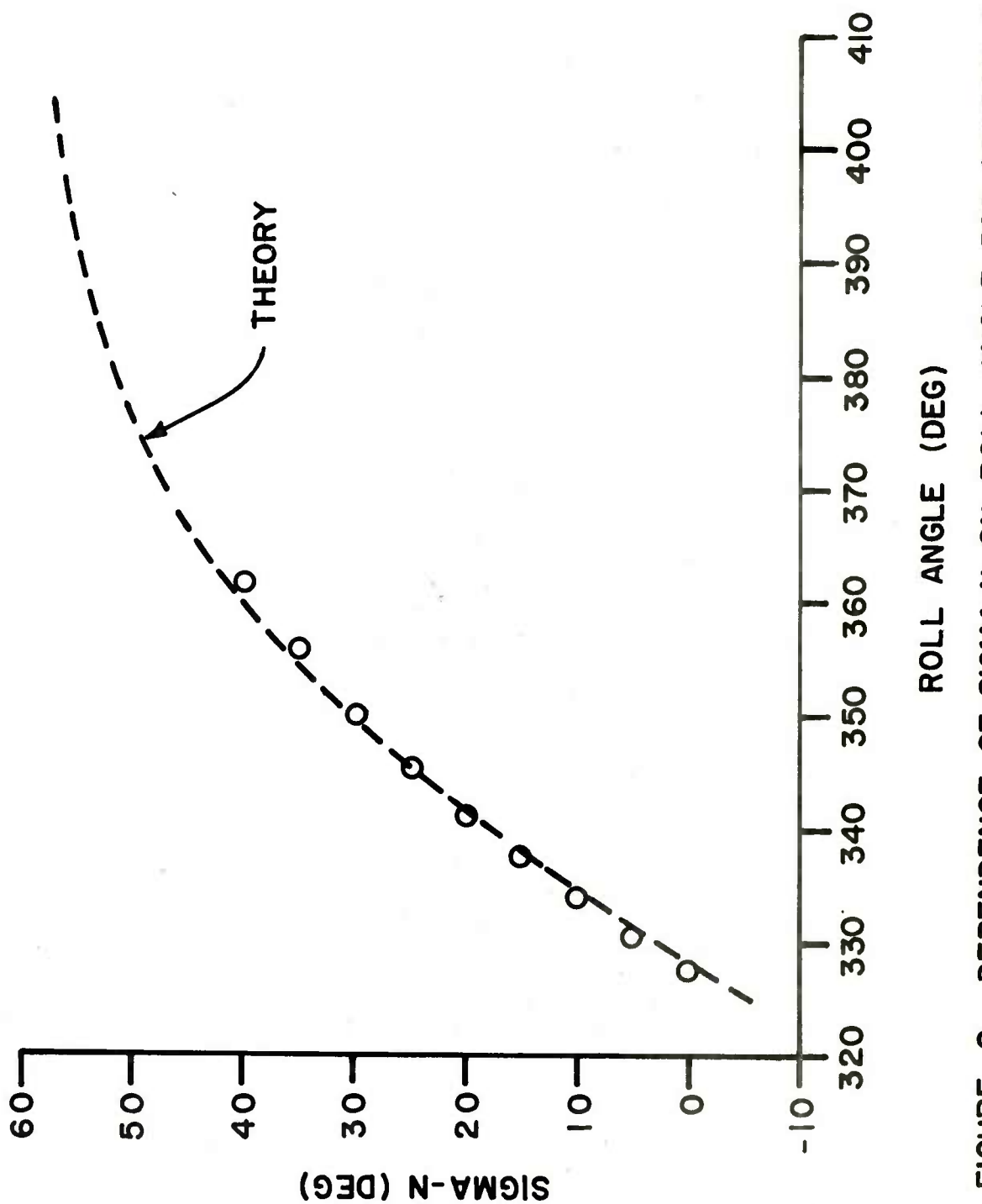


FIGURE 8. DEPENDENCE OF SIGMA-N ON ROLL ANGLE FOR SENSOR 5

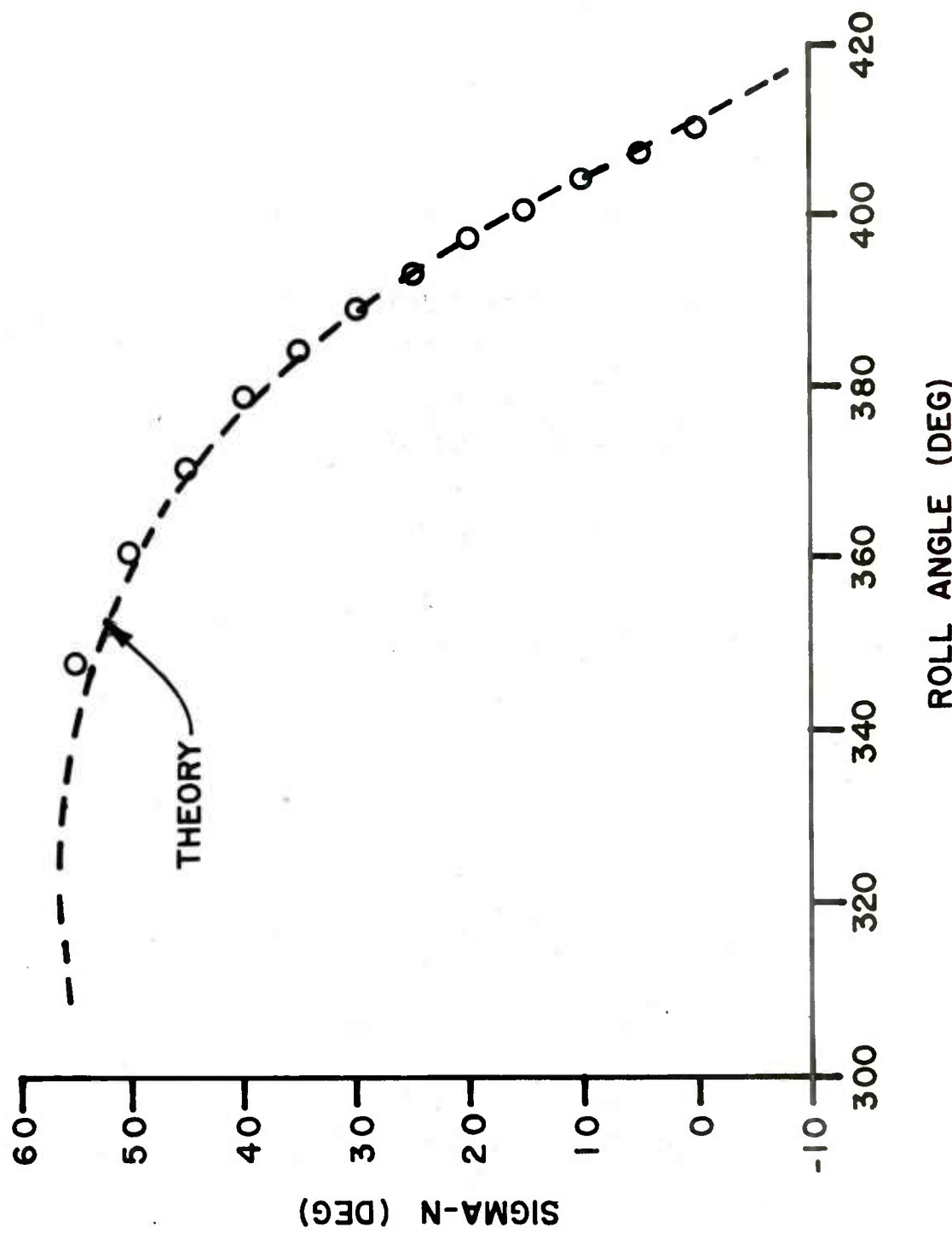


FIGURE 9. DEPENDENCE OF SIGMA-N ON ROLL ANGLE FOR SENSOR 7

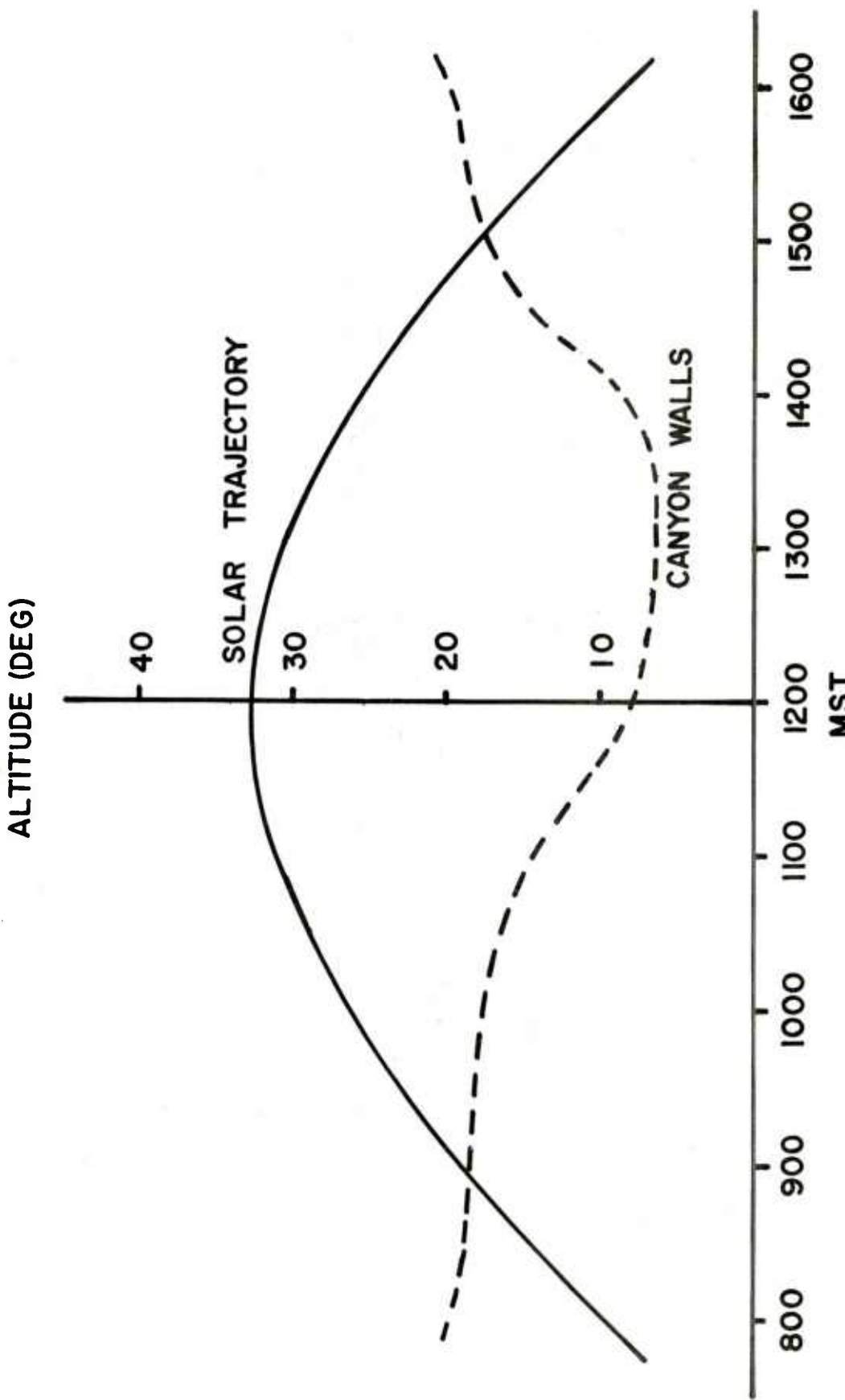


FIGURE 10. ALTITUDE OF SUN AT ALBUQUERQUE, N.M. (12-6-78)

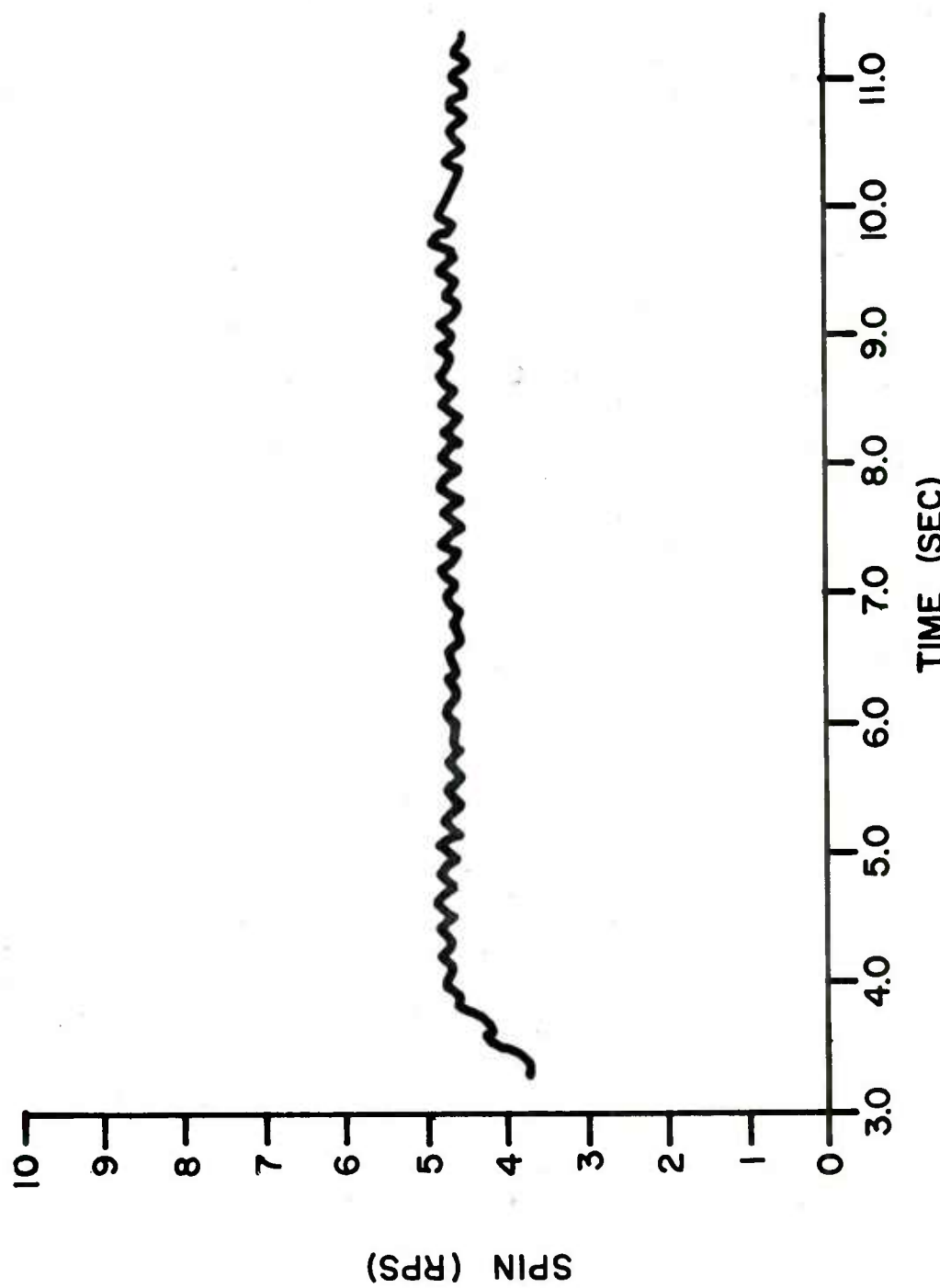


FIGURE II . SPIN VERSUS TIME FOR CABLE DROP 7 (FROM YAW SENSORS)

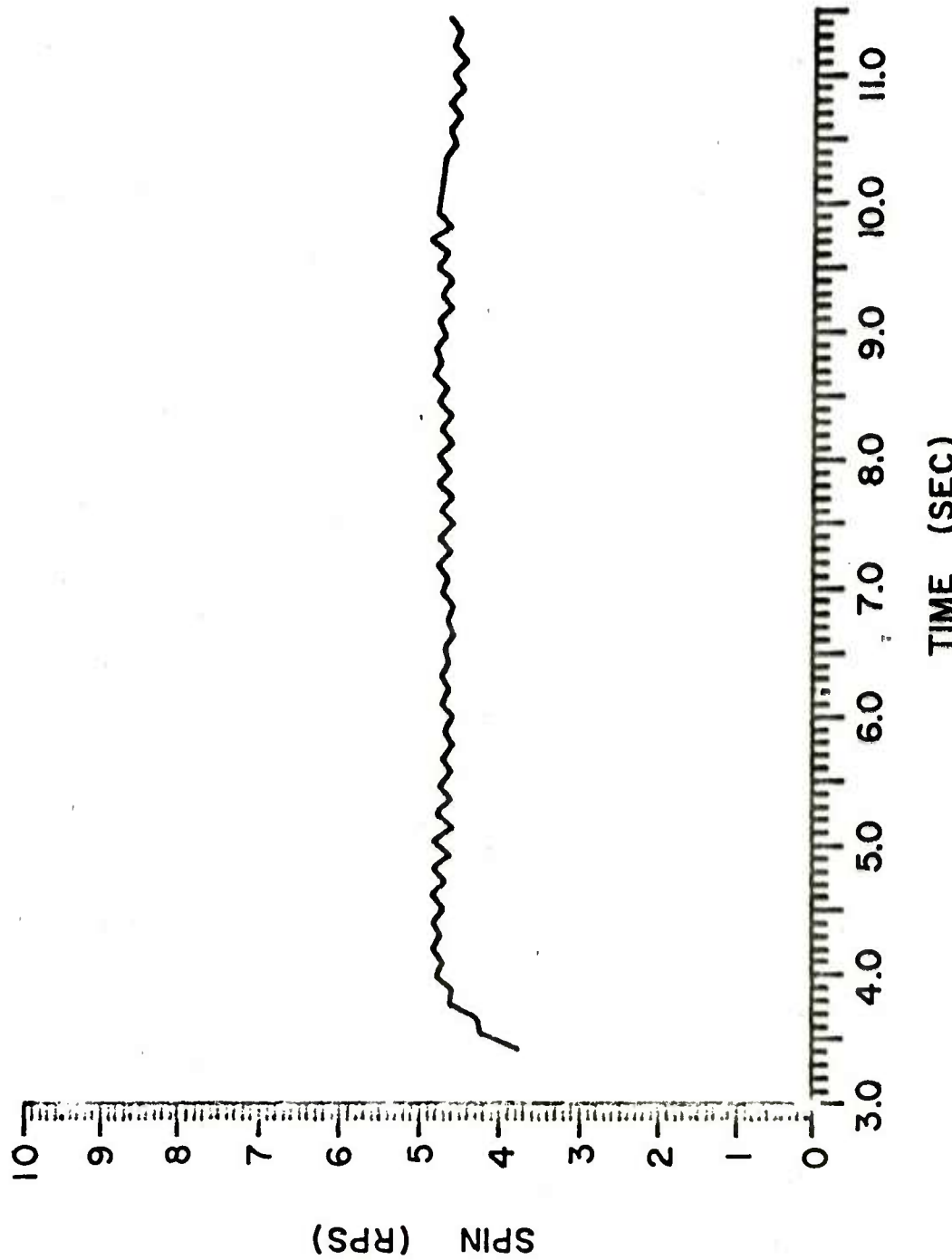


FIGURE 12. SPIN VERSUS TIME FOR CABLE DROP 7(FROM SPIN SENSORS)

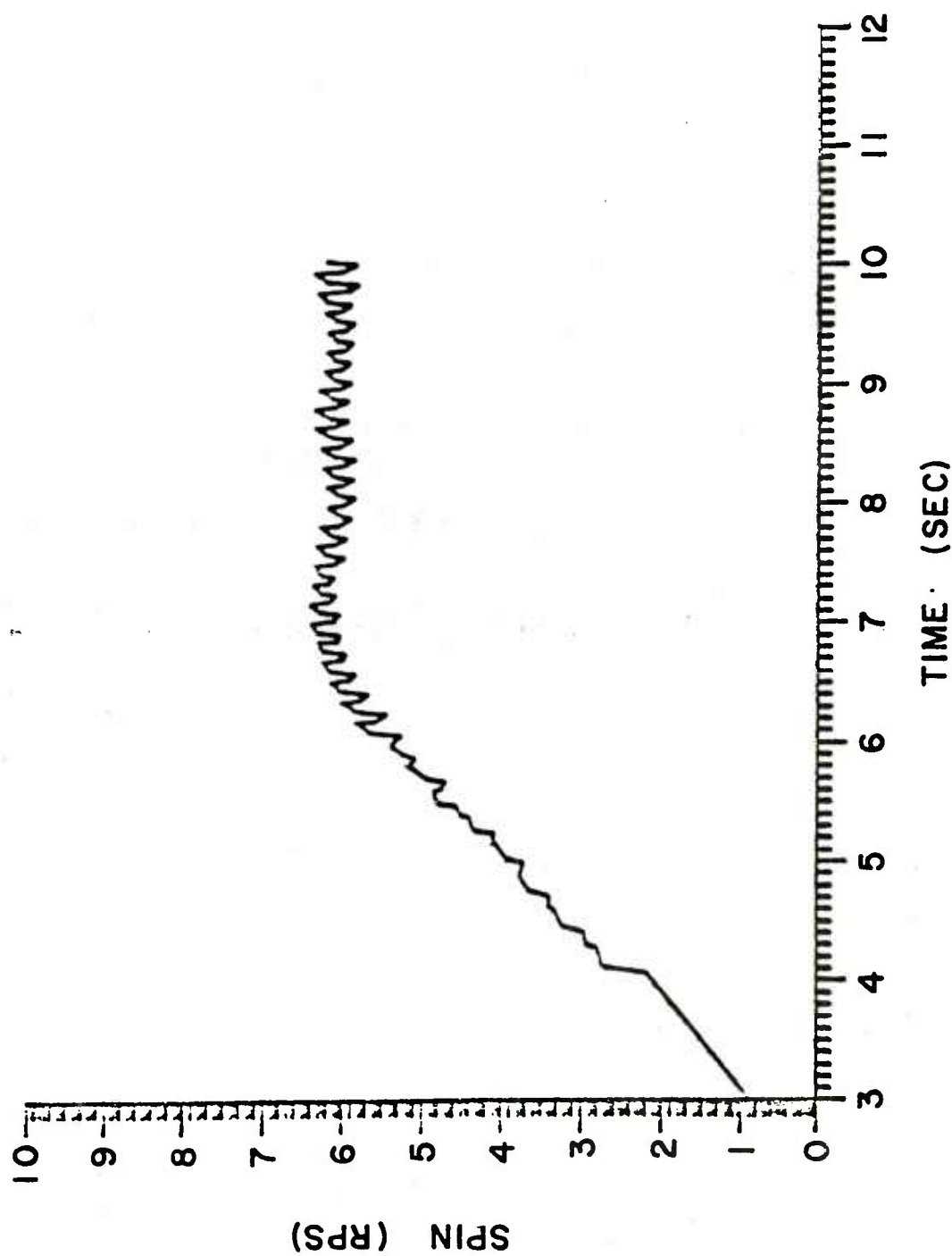


FIGURE 13. SPIN VERSUS TIME FOR CABLE DROP 18

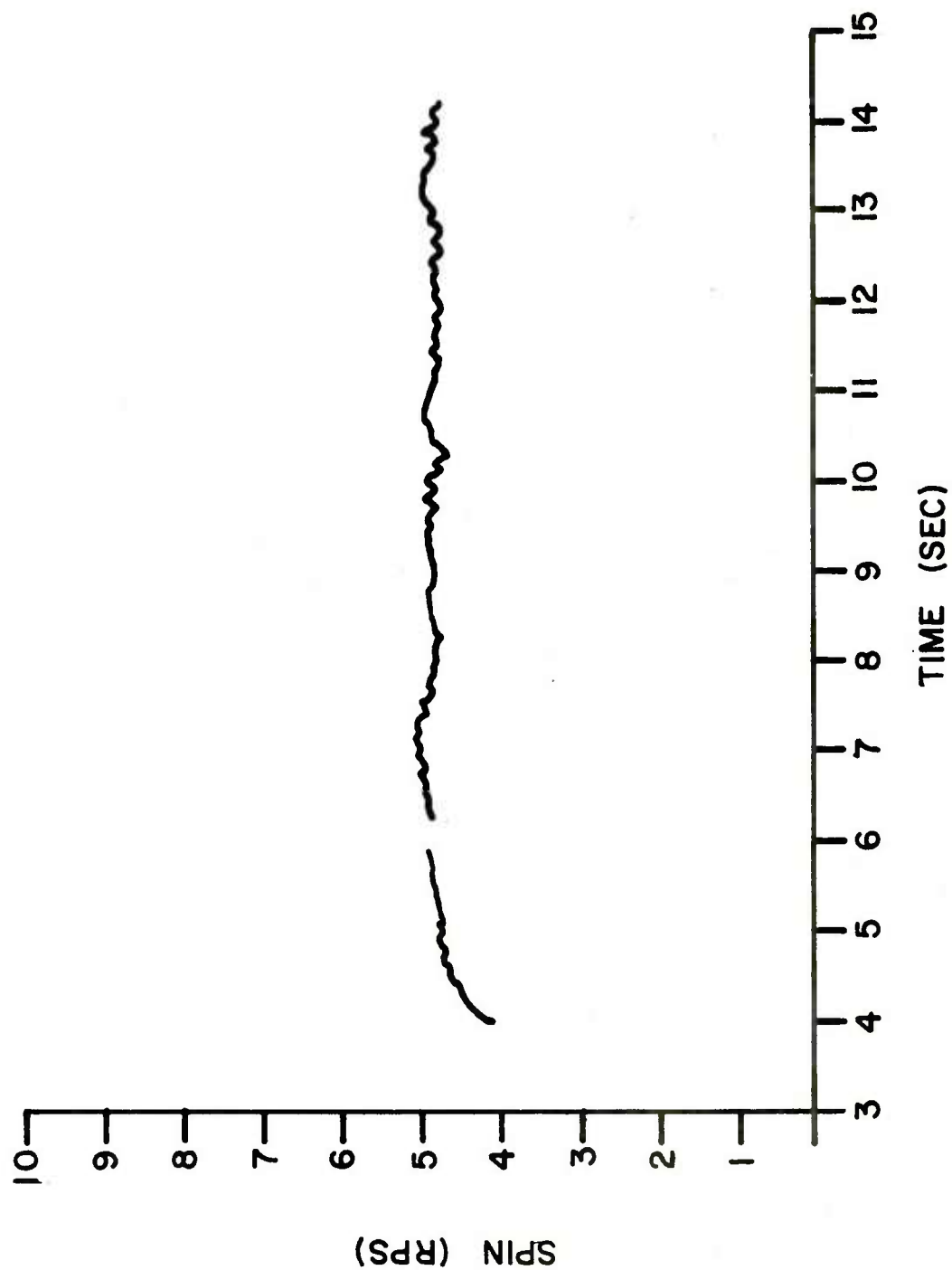


FIGURE 14 A. SPIN VERSUS TIME FOR HELICOPTER DROP 10 (3-15 SEC)

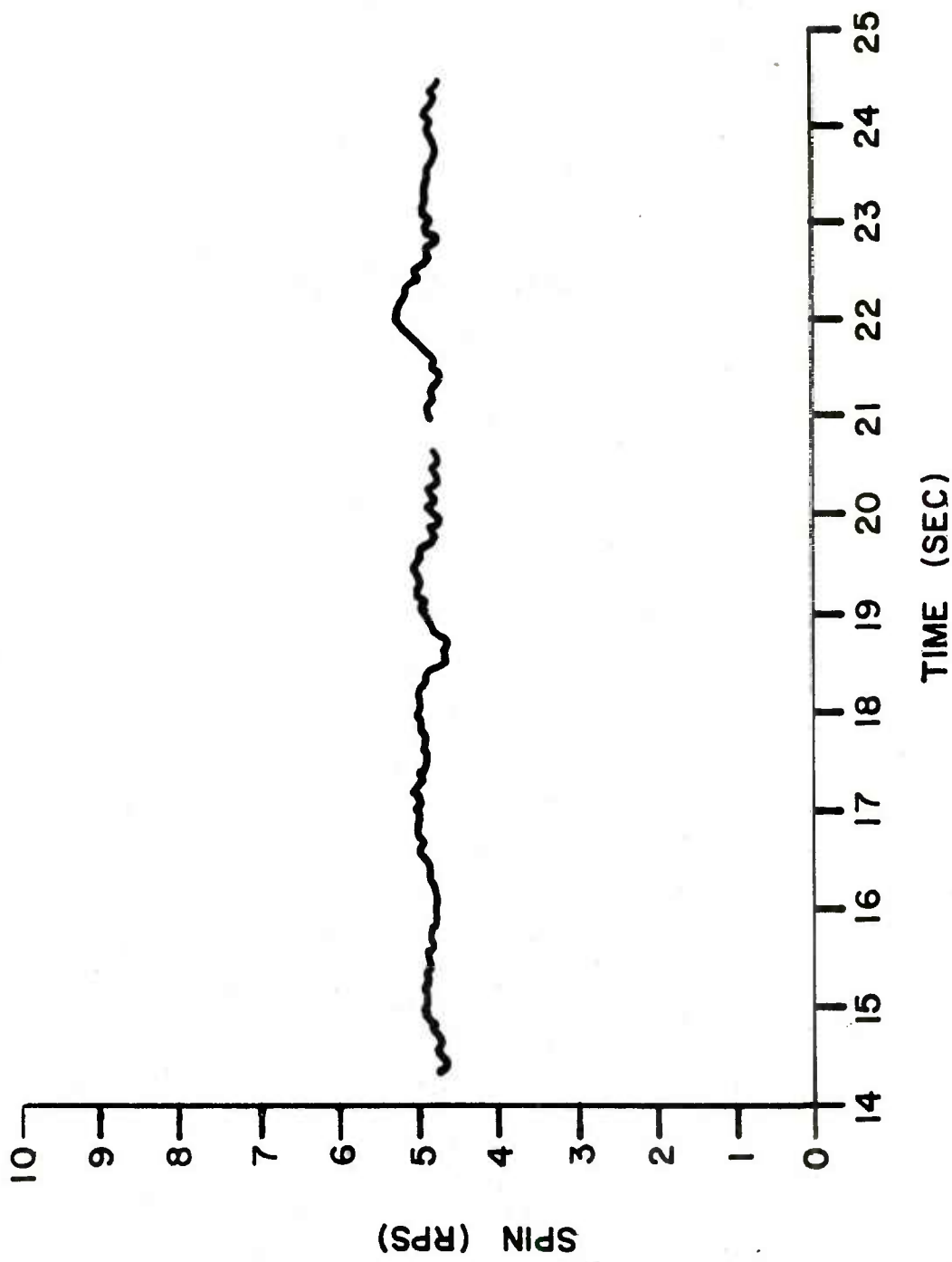


FIGURE 14B. SPIN VERSUS TIME FOR HELICOPTER DROP 10 (14-25 SEC)

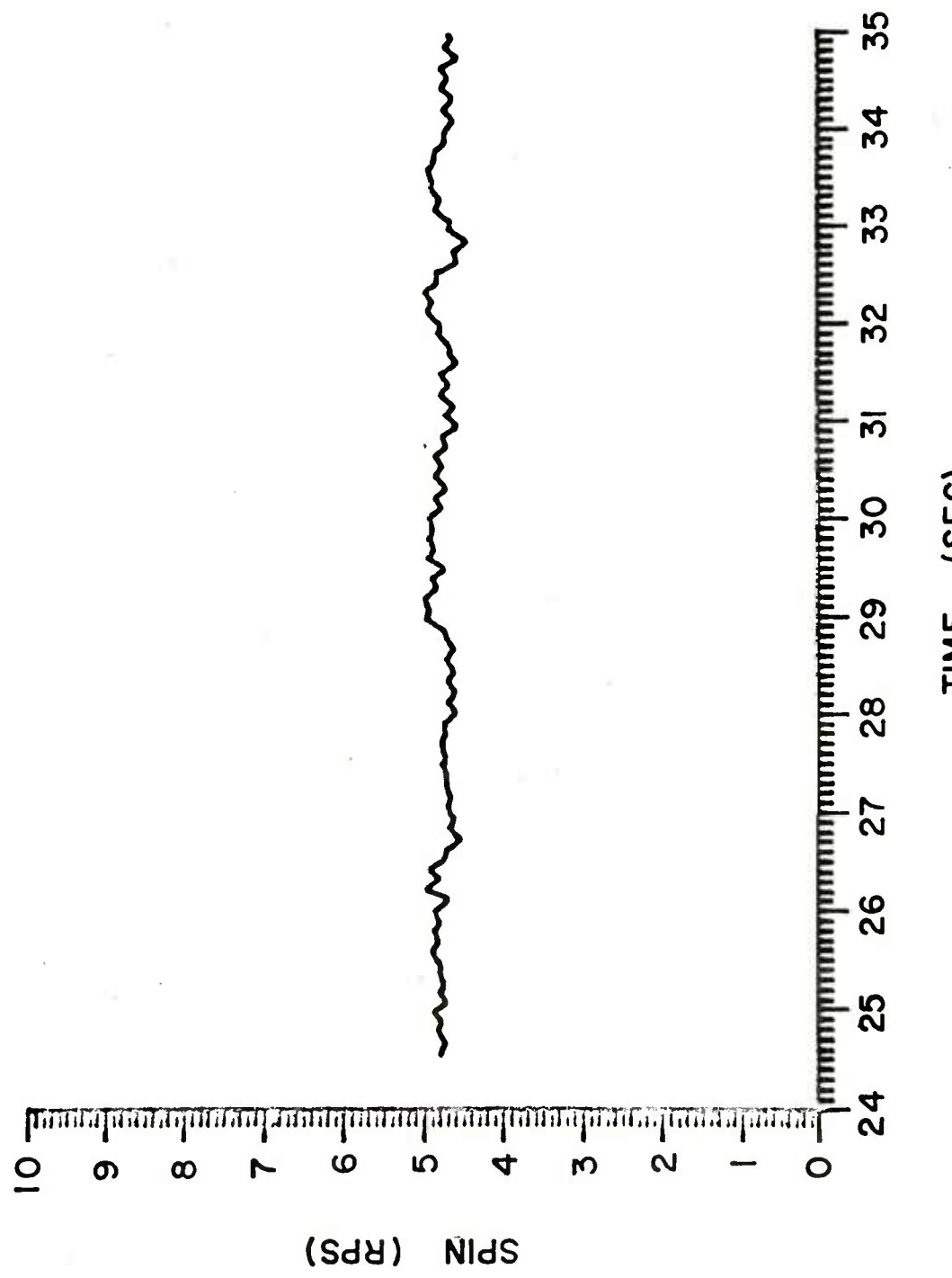


FIGURE I4C. SPIN VERSUS TIME FOR HELICOPTER DROP 10 (24-35 SEC)

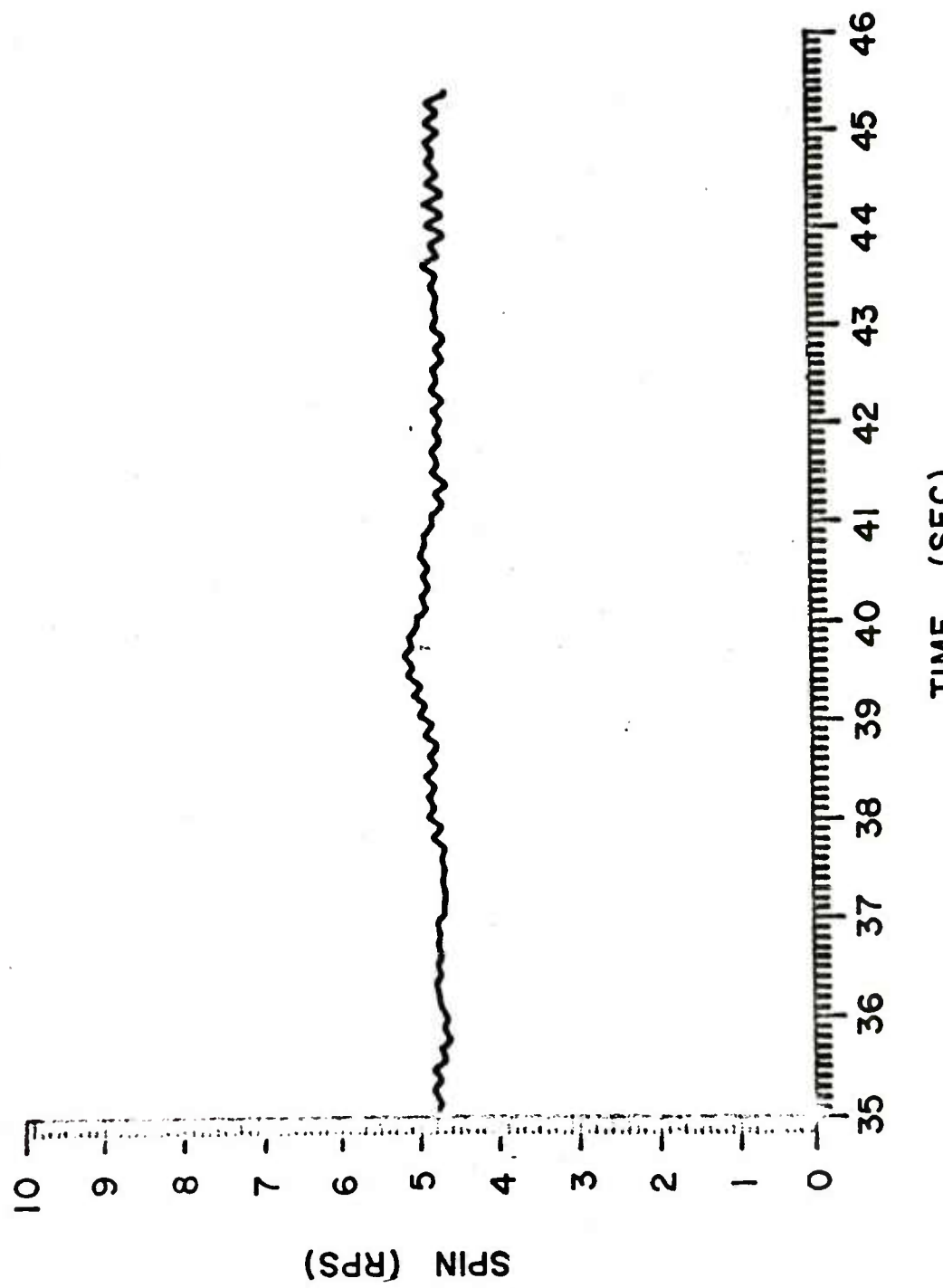


FIGURE 14D. SPIN VERSUS TIME FOR HELICOPTER DROP 10(35-46 SEC)

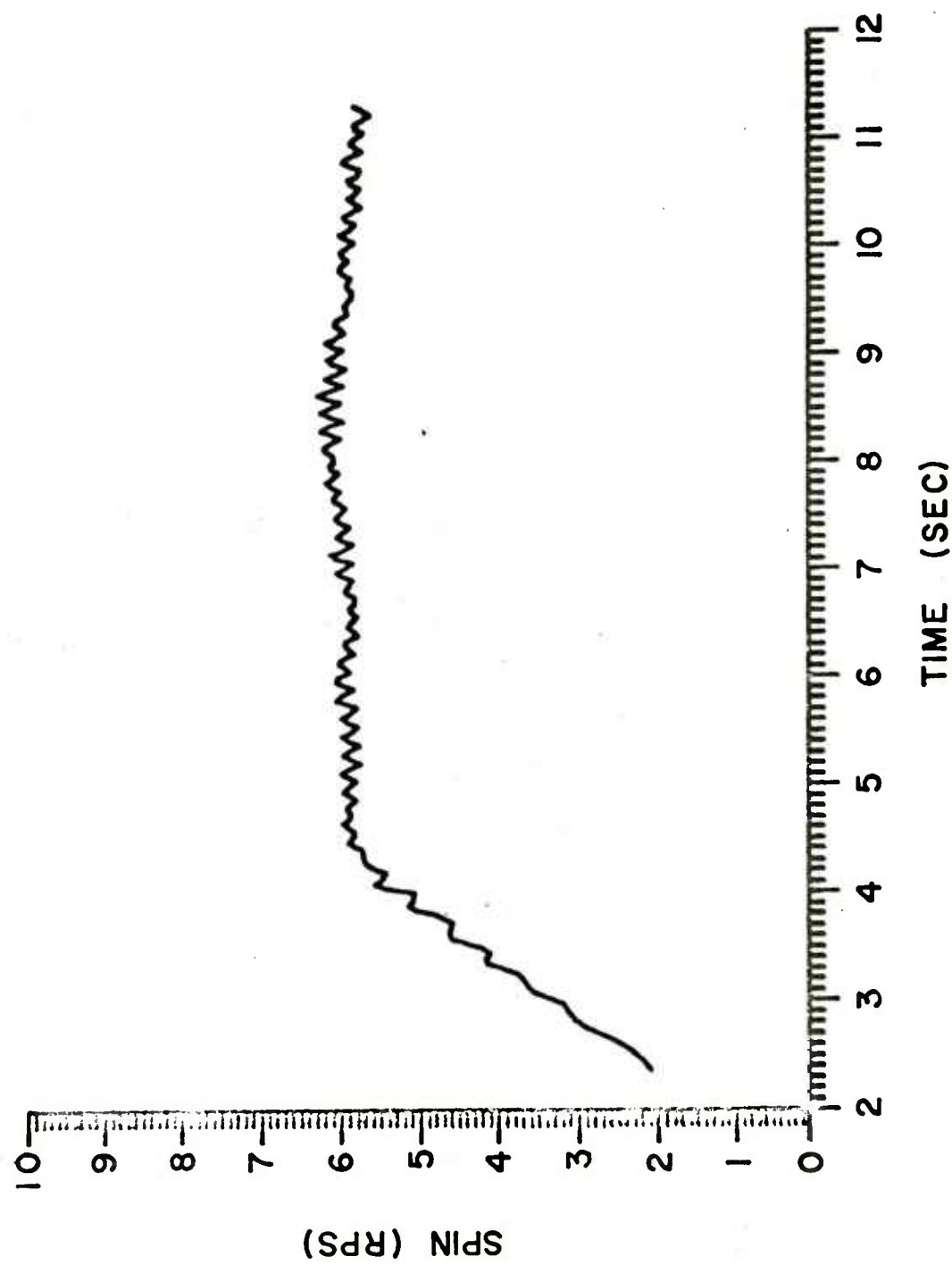


FIGURE 15A. SPIN VERSUS TIME FOR HELICOPTER DROP 27(2-12 SEC)

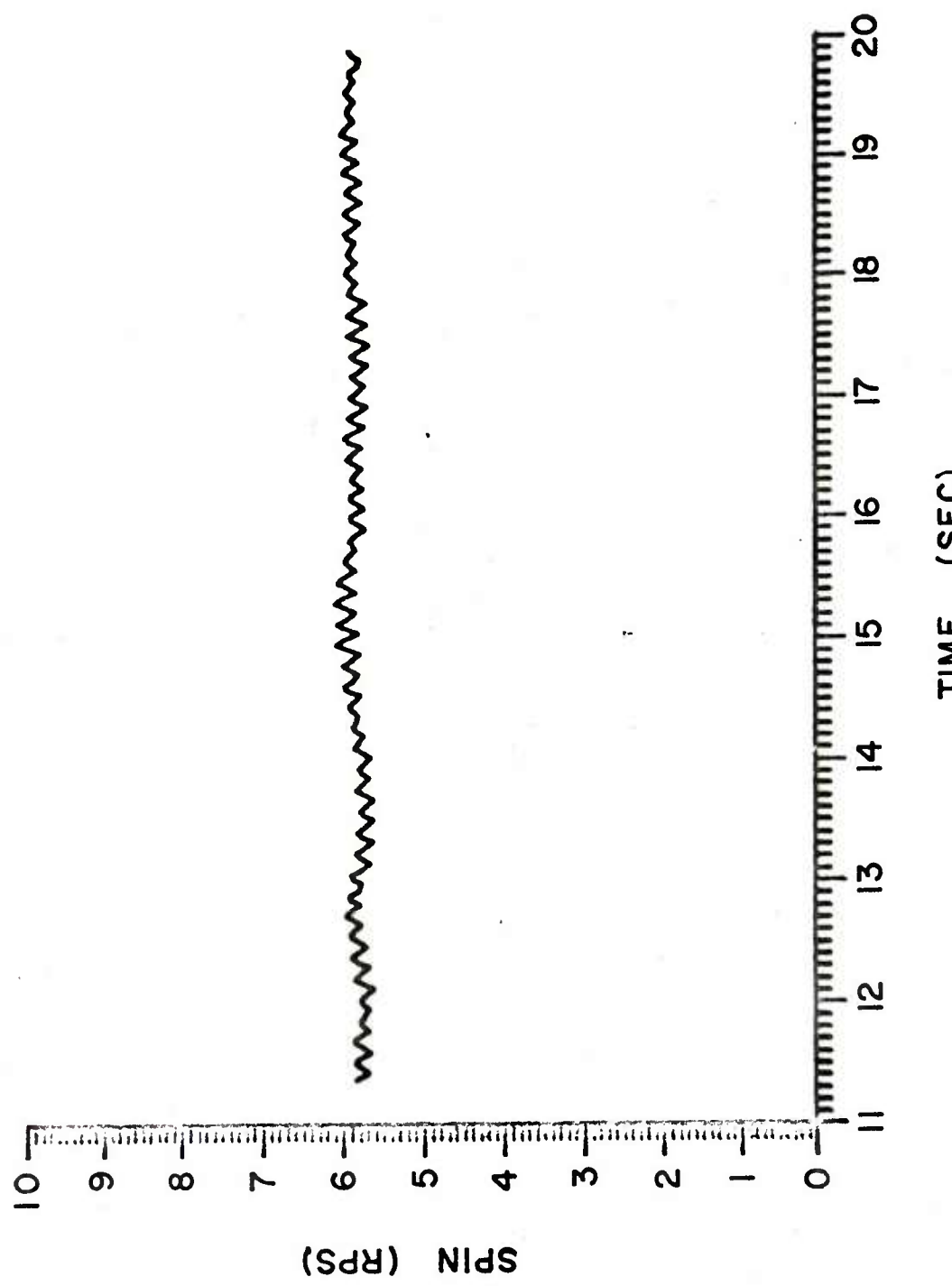
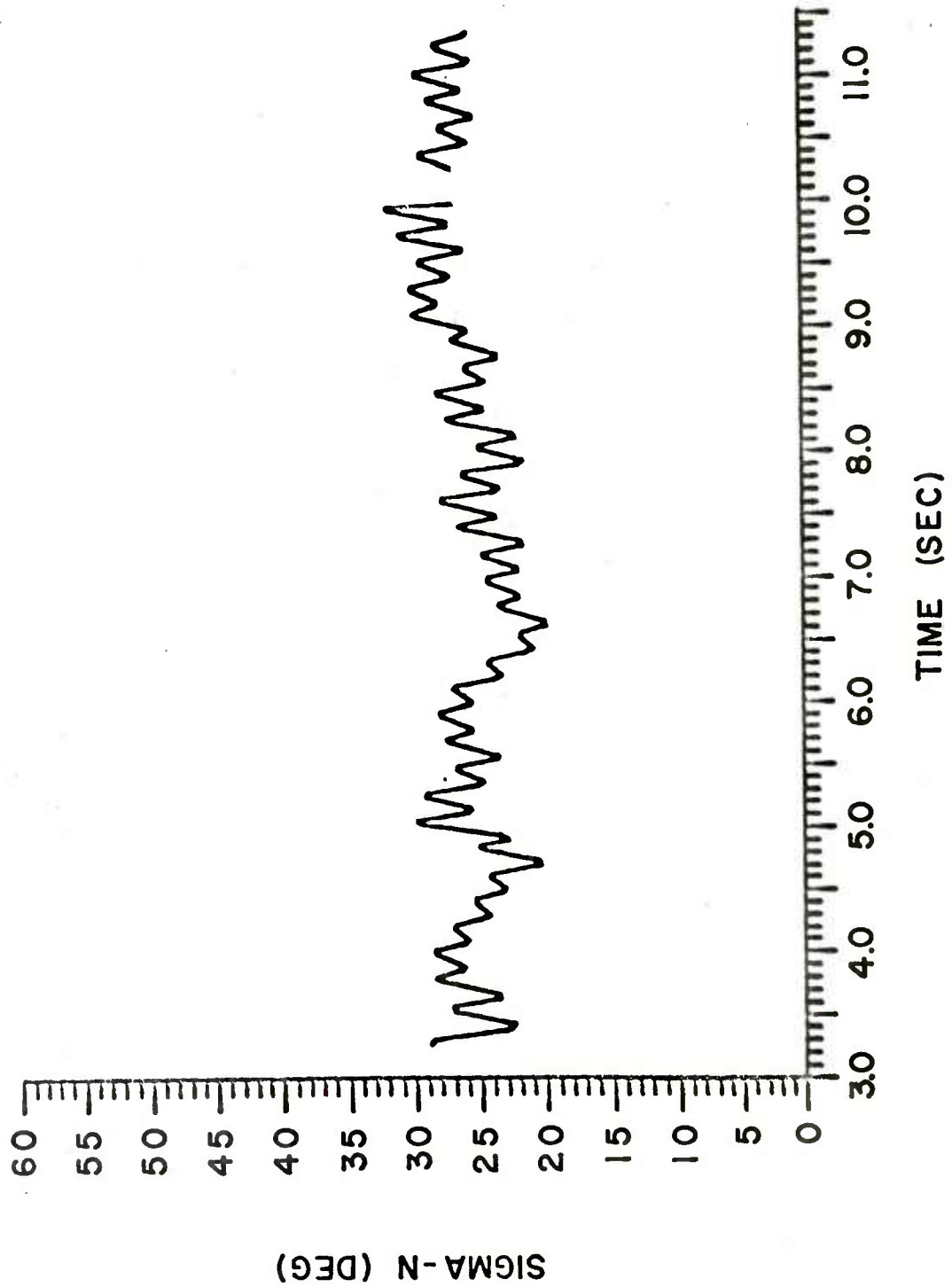


FIGURE 15B. SPIN VERSUS TIME FOR HELICOPTER DROP 27(II-27 SEC)



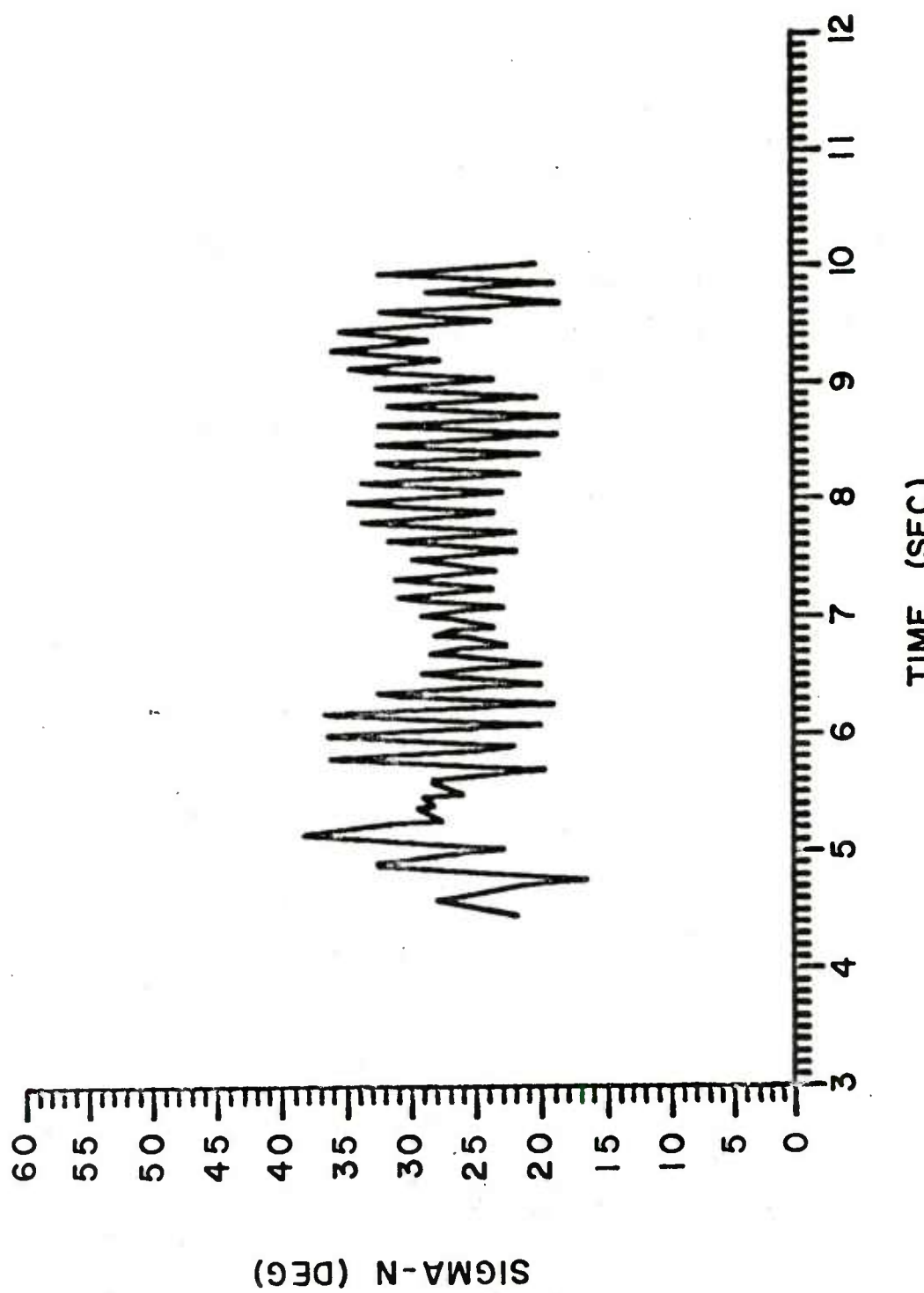


FIGURE 17. YAW VERSUS TIME FOR CABLE DROP 18

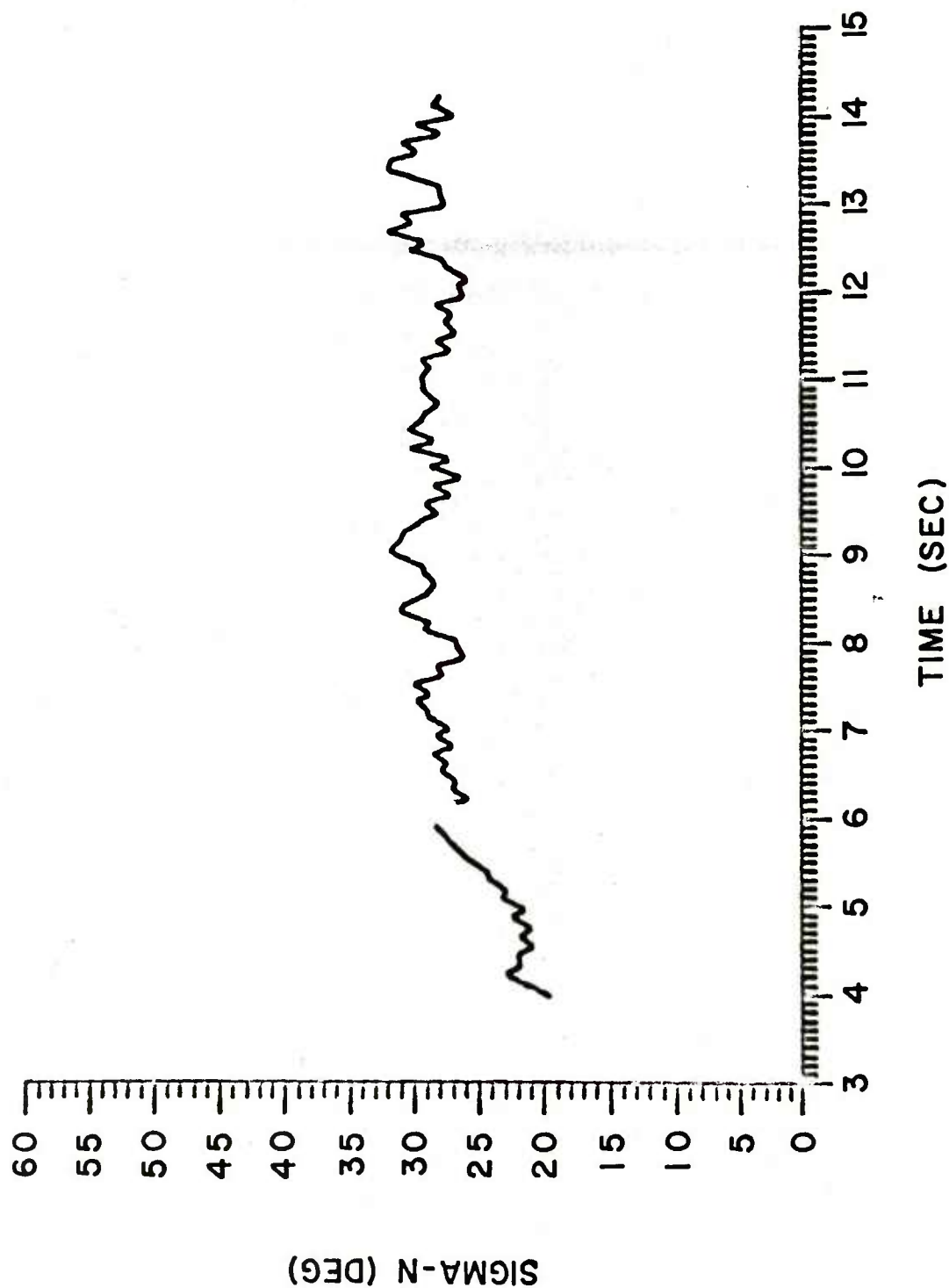


FIGURE 18A. YAW VERSUS TIME FOR HELICOPTER DROP 10 (3-15 SEC)

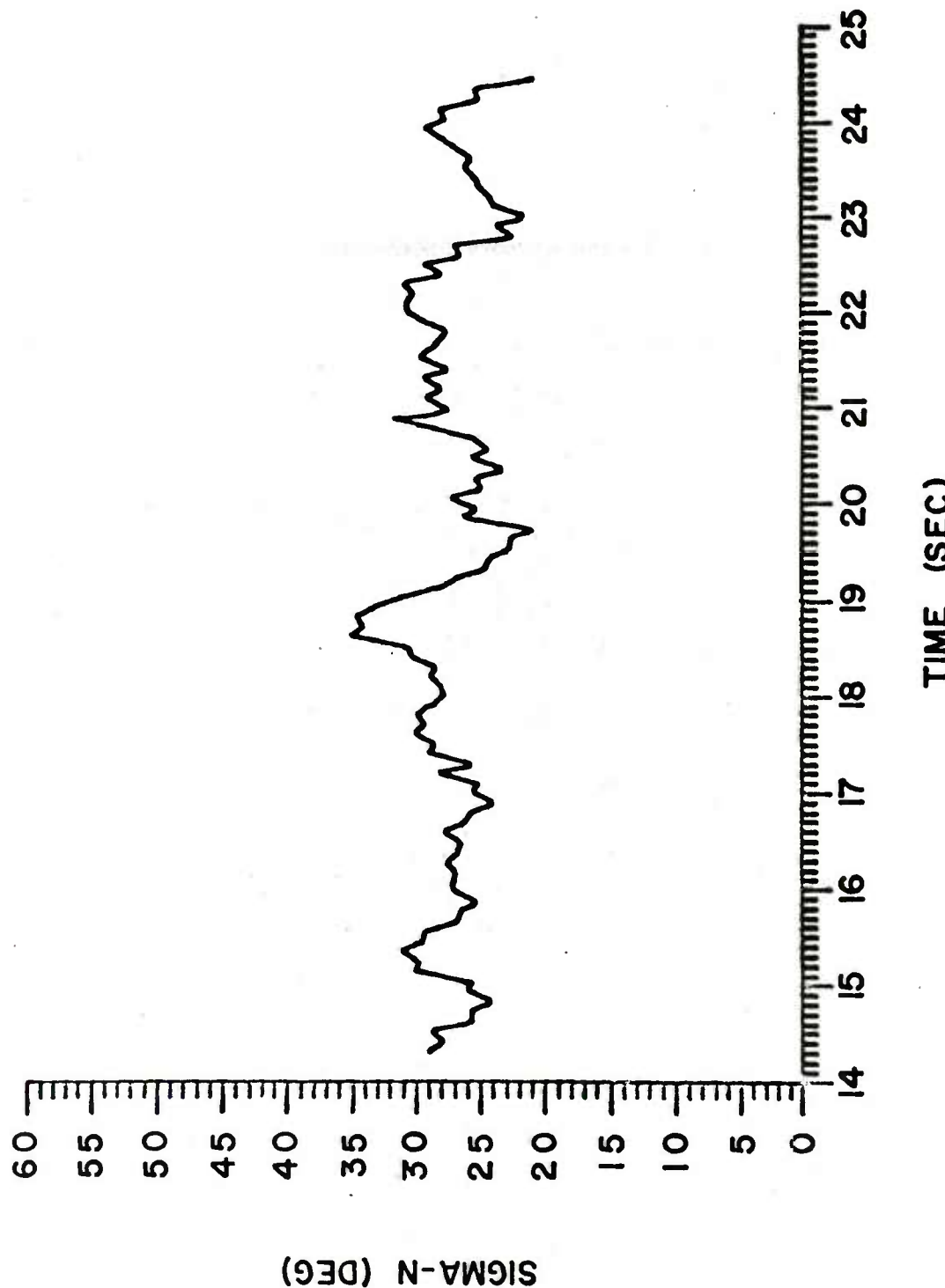


FIGURE 18B. YAW VERSUS TIME FOR HELICOPTER DROP 10 (14-25 SEC)

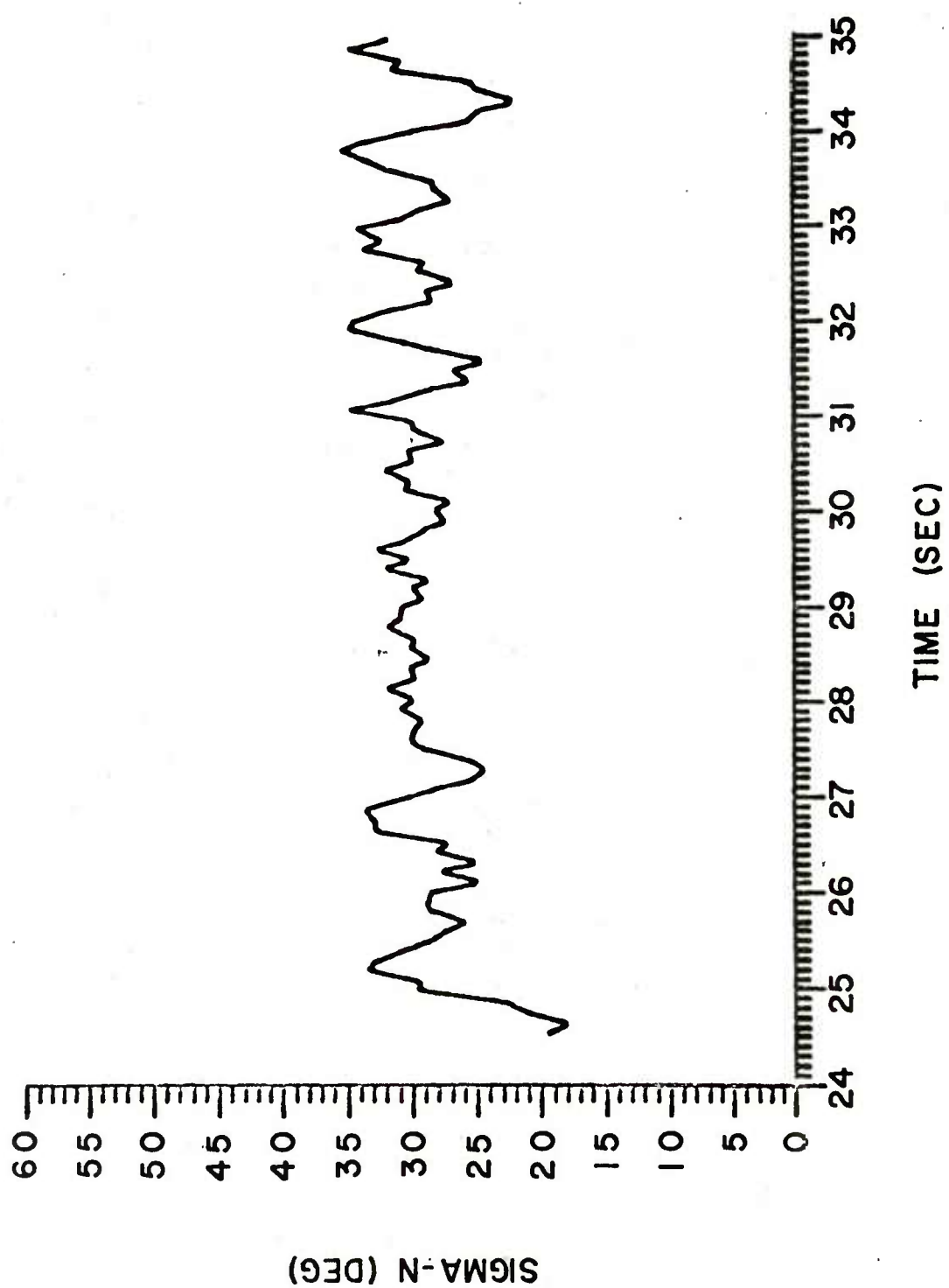


FIGURE 18C. YAW VERSUS TIME FOR HELICOPTER DROP 10(24-35 SEC)

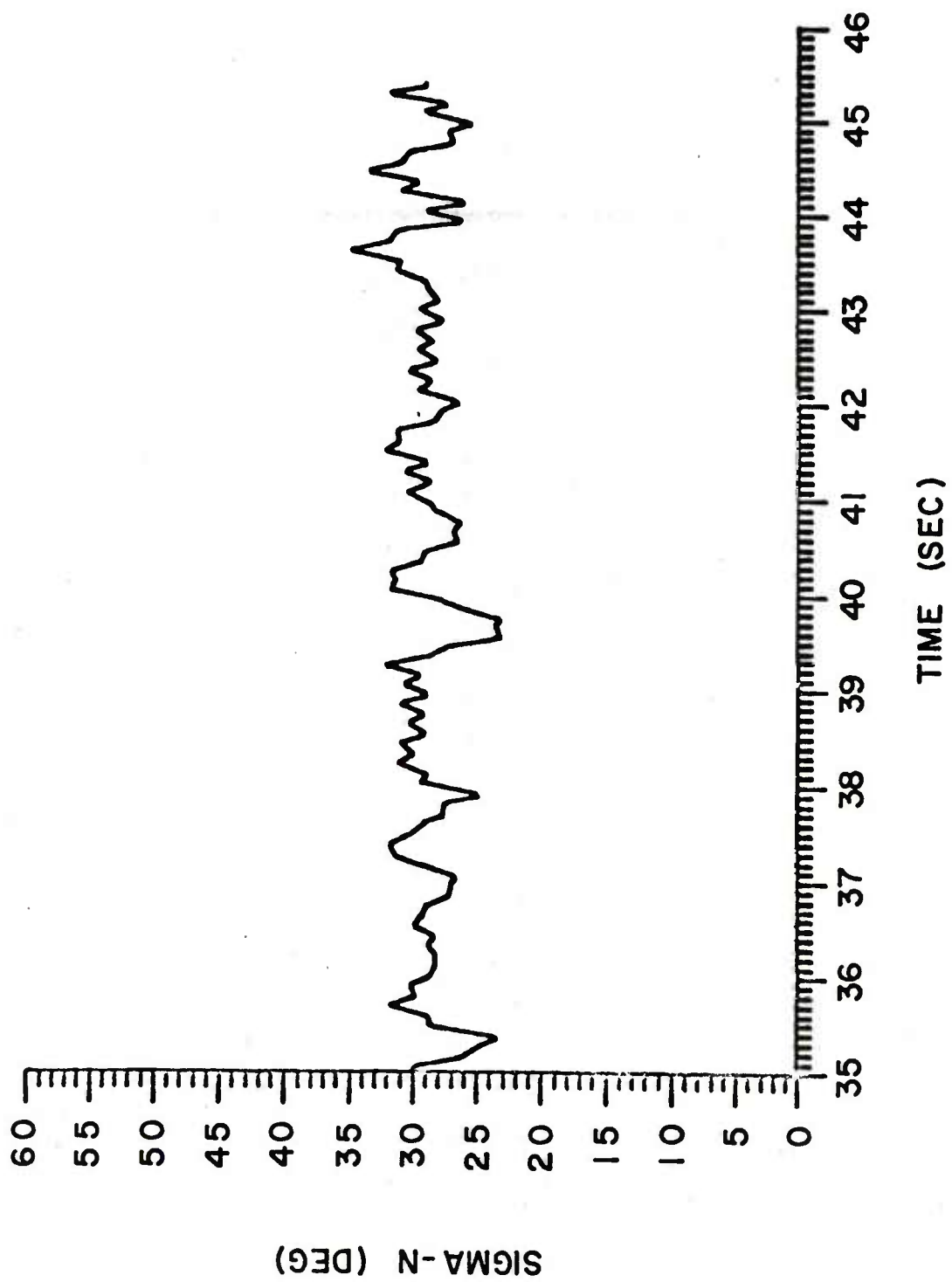


FIGURE 18D. YAW VERSUS TIME FOR HELICOPTER DROP 10 (35-46 SEC)

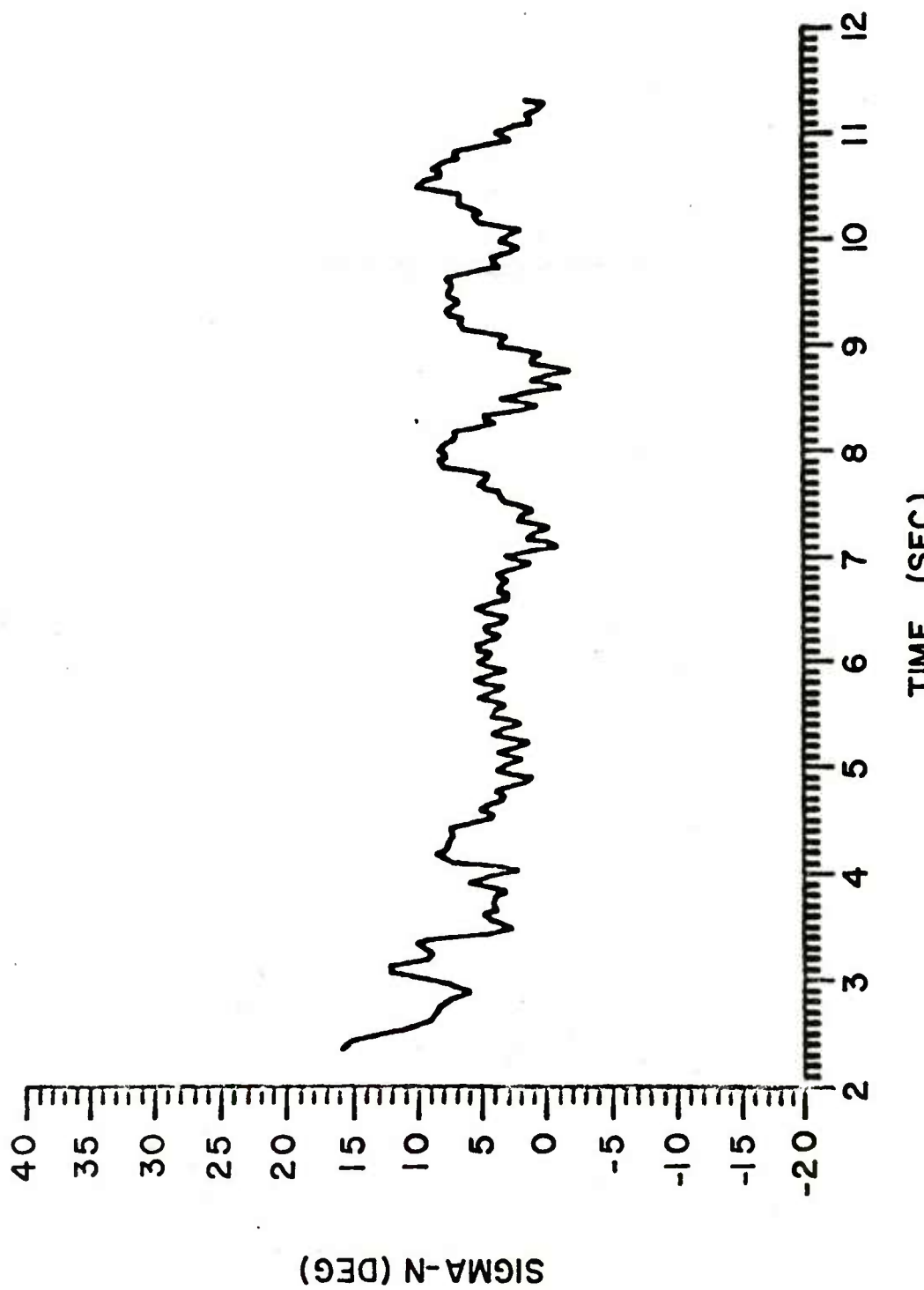


FIGURE 19A. YAW VERSUS TIME FOR HELICOPTER DROP 27(2-12 SEC)

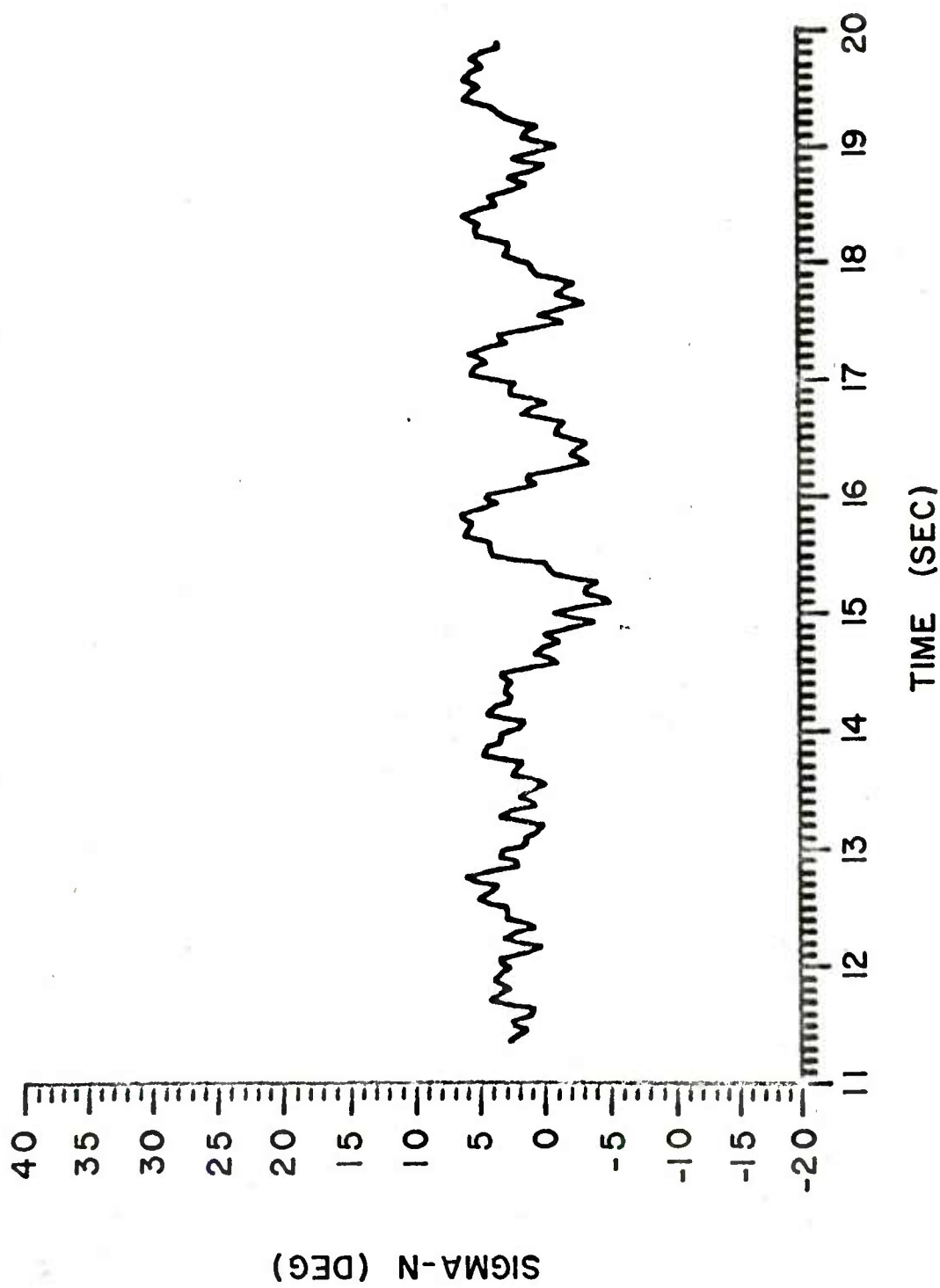


FIGURE 19B. YAW VERSUS TIME FOR HELICOPTER DROP 27 (11-20 SEC)

REFERENCES

1. P.H. Dietz, B.H. Rodin, and R.A. McGee, "SADARM System Simulation (U)", Ballistic Research Laboratory Report ARBRL-MR-02856, August 1978, AD C015654L.
2. W.H. Mermagen, V. Oskay, and J. Bradley, "Yawsonde Tests of SADARM Warhead at Sol Se Mete Canyon, Albuquerque, New Mexico," Ballistic Research Laboratory Memorandum Report ARBRL-MR-02918, May 1979. AD B038263L.
3. W.H. Mermagen and W.H. Clay, "The Design of a Second Generation Yawsonde", Ballistic Research Laboratory Memorandum Report 2368, April 1974. AD 780064.
4. W.H. Mermagen, "Measurements of Dynamical Behavior of Projectiles over Long Flight Paths", Journal of Spacecraft and Rockets, Vol. 8, No. 4, April 1971, pp. 380-385.
5. C.H. Murphy, "Effect of Large High-Frequency Angular Motion of a Shell on the Analysis of Its Yawsonde Records", Ballistic Research Laboratory Memorandum Report 2581, February 1976. AD B009421L.
6. W.H. Clay, "A Precision Yawsonde Calibration Technique", Ballistic Research Laboratory Memorandum Report 2263, January 1973. AD 758158.
7. J.W. Bradley, W.H. Mermagen, and V. Oskay, "Yawsonde Reduction for Slow-Rolling Vehicles," Proceedings of the AIAA Atmospheric Flight Mechanics Conference, August 1979.

LIST OF SYMBOLS

a	damping coefficient of solar aspect angle (Appendix C)
l,m,n	directional cosines of Z' axis (Appendix A)
t	time
x	required roll angle, or elapsed time, between sightings of two sensors
y	angular distance, or elapsed time between two sightings with same sensor (approximately 360° or one roll period)
x/y	fractional difference
A	transformation matrix from un-primed to primed coordinates (Appendix A)
A,B	coefficients relating σ_N to ϕ_s (Appendix A)
\bar{N}_1	unit vector along positive X-axis (Appendix A)
\bar{N}_2	unit vector along the sensor slit (Appendix A)
\bar{P}	vector perpendicular to the optical plane of sensor slit (Appendix A)
\bar{S}	unit vector from the origin of the primed axes to the sun (Appendix A)
T	spin period (Appendix C)
X,Y,Z	canister coordinate system (Appendix A)
X',Y',Z'	measurement coordinate system (Appendix A)
γ	sensor angle with respect to canister axis (Appendix A)
θ	angular position of a sensor on the canister with respect to the clevis (Appendix A)
σ	solar aspect angle
σ_c	altitude of the sun (Appendix C)
σ_f	fast component of solar aspect angle modulation (Appendix C)

LIST OF SYMBOLS (continued)

σ_s	slow component of solar aspect angle modulation (Appendix C)
σ_N	$= \frac{\pi}{2} - \sigma$, complementary solar aspect angle
τ_c	average spin period (Appendix C)
τ_o	amplitude of spin period modulation (Appendix C)
ϕ	canister inclination with respect to spin axis; canister roll angle (Appendix A)
ϕ_s	angular location of the sun in the primed coordinates (Appendix A)
$\dot{\phi}$	canister spin rate
ω_f	circular rate of fast component (Appendix C)
ω_s	circular rate of slow component (Appendix C)
ω_τ	spin period modulation frequency (Appendix C)

APPENDIX A

DETERMINATION OF SENSOR INSTALLATION ANGLES

The second SADARM test canister was designed to include eight solar sensors, four to be installed as spin sensors and four as yaw sensors. Since the canister is suspended from the parachute at some inclination ϕ with respect to the roll axis of the system, it is not at all obvious how to install the individual sensors to obtain roll or yaw measurements. In order to obtain a roll rate measurement, the sensor slit must be installed parallel to the roll axis. For maximum σ_N coverage, the yaw sensors must be installed at some angle

γ with respect to the canister axis which will provide a mostly linear calibration in a wide field of view. The natural system for the yaw and roll rate measurements is the parachute/canister coordinate system. The natural system for installing sensors is the cylindrical canister coordinate system.

We define a coordinate system centered on the canister so that the Z-axis is along the axis of symmetry and the X-axis passes through any sensor slit. Let \bar{N}_1 be a unit vector along the positive X-axis and let \bar{N}_2 be a unit vector along the sensor slit. In the canister coordinate system, these unit vectors have components

$$\bar{N}_1 = (1, 0, 0)$$

$$\bar{N}_2 = (0, \sin\gamma, \cos\gamma)$$

where γ is the inclination of the slit from the Z-axis. Positive γ is measured from the Z-axis to the Y-axis. A vector perpendicular to the optical plane of the slit, then, is

$$\bar{P} = \bar{N}_1 \times \bar{N}_2$$

which has components in the canister system

$$\bar{P} = (0, -\cos\gamma, \sin\gamma)$$

Figure A1 shows the canister coordinate system. The measurement coordinate system is defined by tilting the Z-axis at angles ϕ and θ to form a primed coordinate system. The new Z-prime axis is the axis of rotation of the canister/parachute system. Figure A2 shows the relationship between the two coordinate systems.

To transfer from the canister to the tilted coordinate system, consider the transformation

$$\begin{pmatrix} x' \\ y' \\ z' \end{pmatrix} = A \begin{pmatrix} x \\ y \\ z \end{pmatrix}$$

If the direction cosines of the Z' axis are l, m, n then

$$l = \sin\phi\cos\theta$$

$$m = \sin\phi\sin\theta$$

$$n = \cos\phi$$

The transformation matrix A can be written as

$$A = \begin{bmatrix} \sqrt{1-l^2} & \frac{-lm}{\sqrt{1-l^2}} & \frac{-ln}{\sqrt{1-l^2}} \\ 0 & \frac{n}{\sqrt{1-l^2}} & \frac{m}{\sqrt{1-l^2}} \\ l & m & n \end{bmatrix}$$

Transforming the components of the perpendicular vector \bar{P} , we have

$$\bar{P}' = A\bar{P}$$

and, after some algebra

$$\bar{P}' = (P_1, P_2, P_3)$$

where

$$\begin{aligned} P_1 &= \left(\frac{lm}{\sqrt{1-l^2}} \right) \cos\gamma - \left(\frac{ln}{\sqrt{1-l^2}} \right) \sin\gamma \\ P_2 &= \left(\frac{n}{\sqrt{1-l^2}} \right) \cos\gamma - \left(\frac{m}{\sqrt{1-l^2}} \right) \sin\gamma \\ P_3 &= -m\cos\gamma + n\sin\gamma \end{aligned}$$

Define \bar{S} as a unit vector directed from the origin of the primed coordinate system (the measurement system) to the sun. Let σ be the angle between \bar{S} and the Z' -prime and let ϕ_S be the angle between the projection of \bar{S} onto the X' -prime, Y' -prime plane and the X' -prime axis. The angles are shown in Figure A3. The solar sensor is illuminated by the sun when the unit scalar vector and the optical plane of the sensor are coplanar. This is true when

$$\bar{S} \cdot \bar{P}' = 0$$

Thus,

$$\begin{aligned} \sin\sigma \cos\phi_S & \left[\left(\frac{\ell m}{\sqrt{1-\ell^2}} \right) \cos\gamma - \left(\frac{\ell n}{\sqrt{1-\ell^2}} \right) \sin\gamma \right] \\ -\sin\sigma \sin\phi_S & \left[\left(\frac{n}{\sqrt{1-\ell^2}} \right) \cos\gamma + \left(\frac{m}{\sqrt{1-\ell^2}} \right) \sin\gamma \right] \\ + \cos\sigma (n \sin\gamma - m \cos\gamma) & = 0 \end{aligned}$$

For design purposes, $\sigma_N = \pi/2 - \sigma$ is a more convenient variable. The above equation can be solved for σ_N in terms of the remaining angles:

$$\tan\sigma_N = A \cos\phi_S + B \sin\phi_S$$

where

$$A = \frac{-\sin\phi \cos\theta (\sin\phi \sin\theta - \tan\gamma \cos\phi)}{(\tan\gamma \cos\phi - \sin\phi \sin\theta) \sqrt{1 - \sin^2\phi \cos^2\theta}}$$

$$B = \frac{\cos\phi + \tan\gamma \sin\phi \sin\theta}{(\tan\gamma \cos\phi - \sin\phi \sin\theta) \sqrt{1 - \sin^2\phi \cos^2\theta}}$$

The angles ϕ and θ are given by the tilt of the canister and the location of the sensor in question. The above equations can be used to determine the optimum value of γ for the proper variation of σ_N with ϕ_S depending on whether a roll or yaw orientation is required.

Figure A4 shows how the function σ_N varies with ϕ_S with γ as a parameter, for a given location θ of the sensor slit.

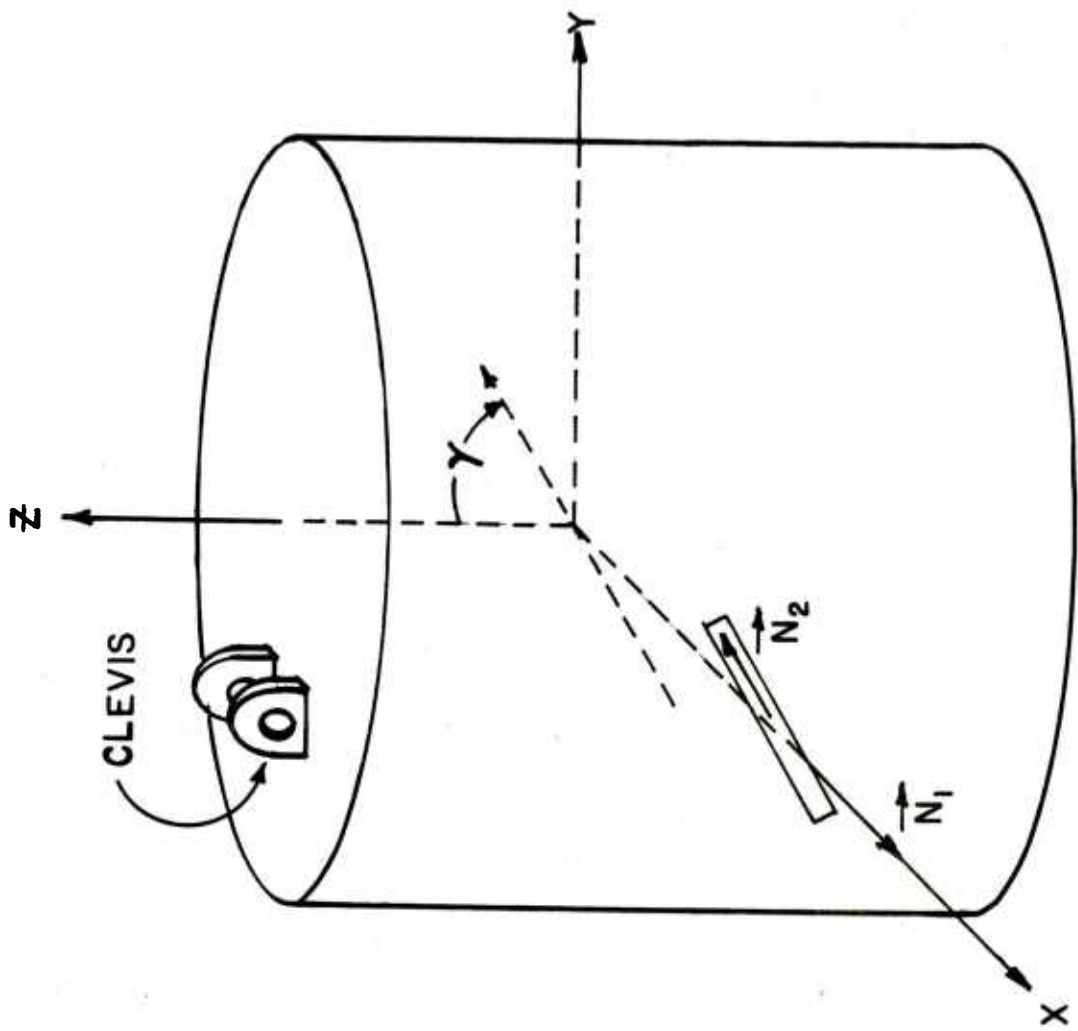


FIGURE A1 CANISTER COORDINATE SYSTEM

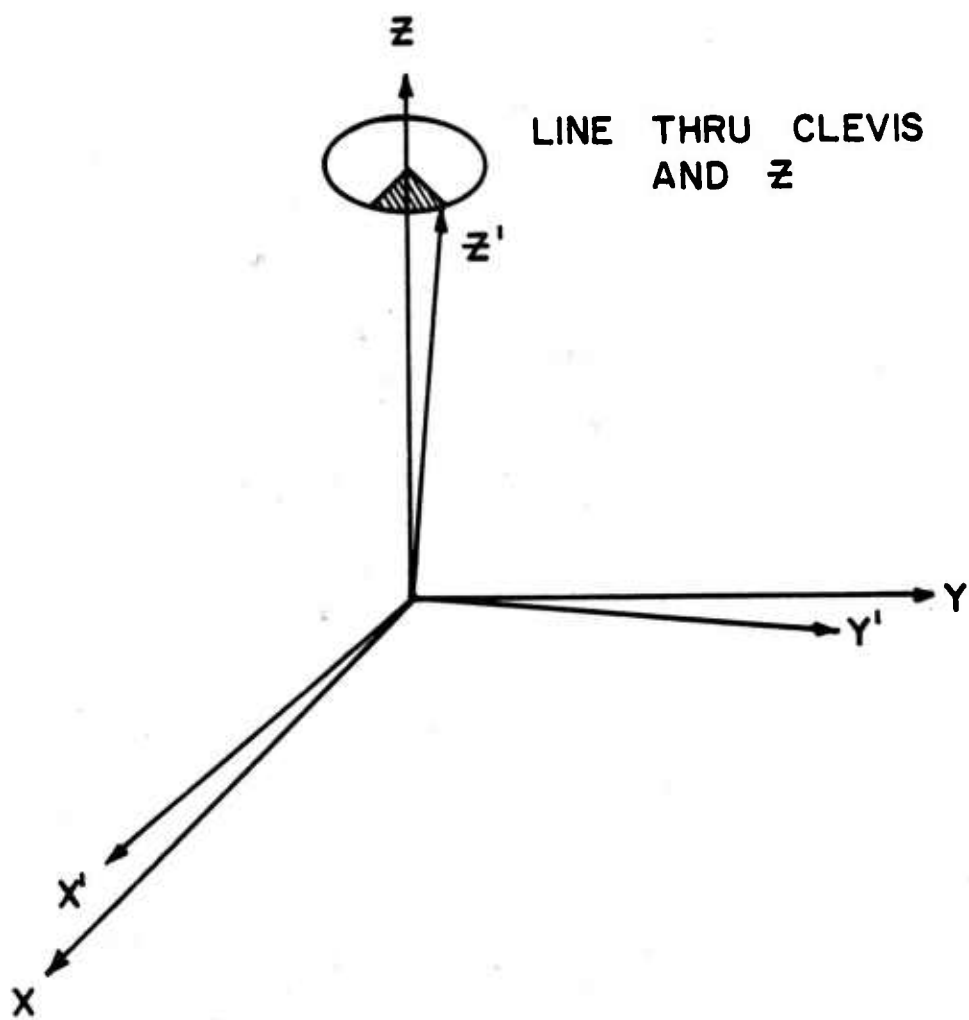


FIGURE A2 TILTED MEASUREMENT SYSTEM

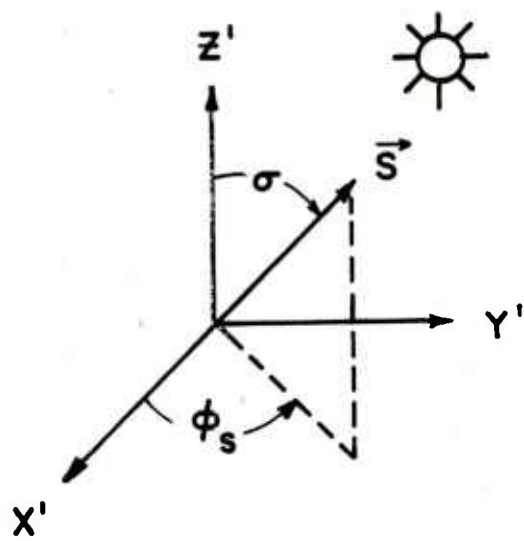


FIGURE A3 THE SOLAR VECTOR IN THE MEASUREMENT COORDINATE SYSTEM

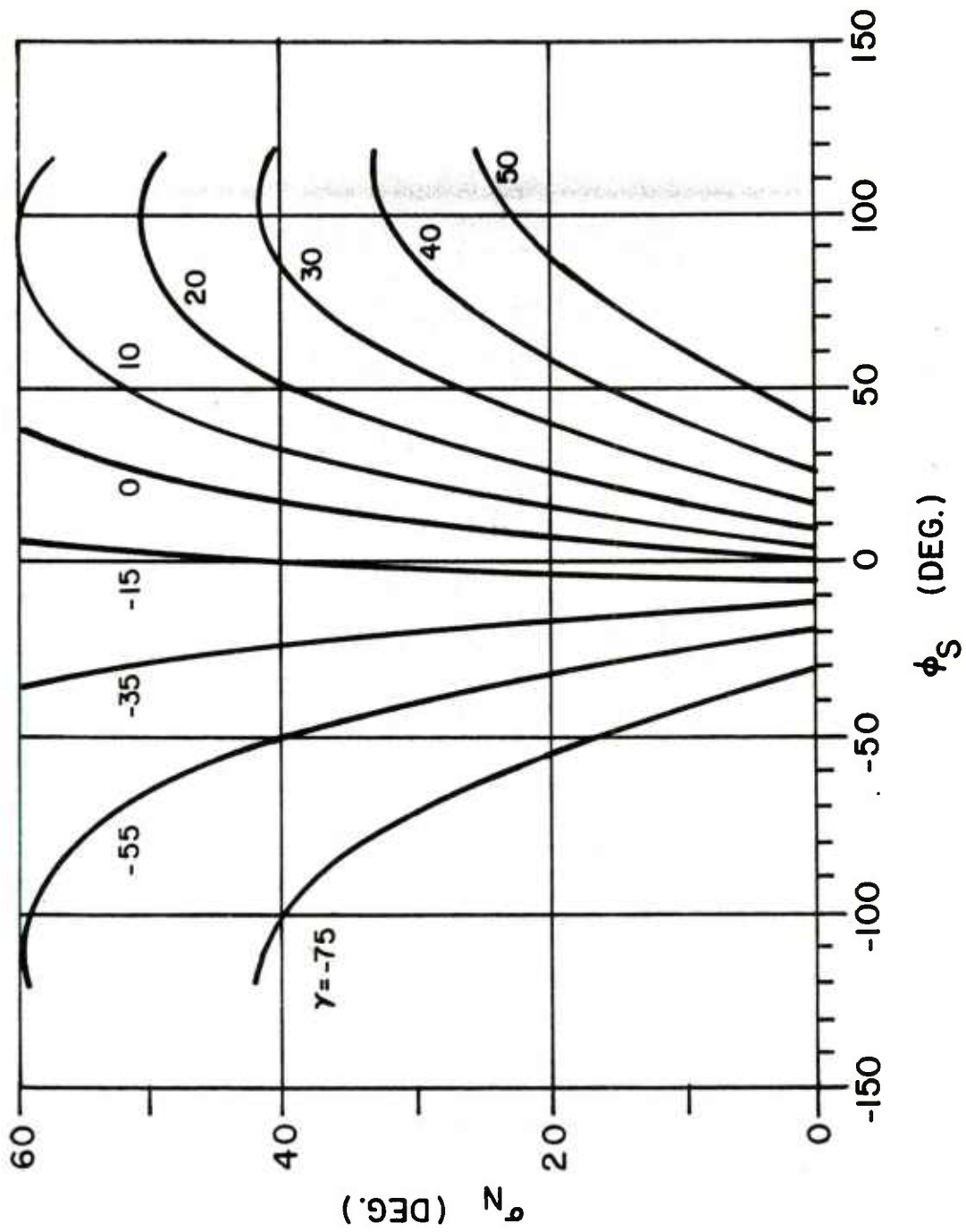


FIGURE A4 SOLAR ASPECT ANGLE AS A FUNCTION OF ROLL ANGLE
WITH γ AS PARAMETER

APPENDIX B
ADDITIONAL YAWSONDE PLOTS FOR CABLE DROPS

Spin and yaw histories of some additional cable drops are presented in this Appendix. Bulk of the data presented were obtained with the 2.13-metre Vortex-Ring parachute. There are three exceptions: (a) cable drop 25 used 1.83-metre VRP similar to the drop 18 discussed in the body of the report, (b) drops 28 and 30 used the 2.13-metre VRP but also used a modified linkage which was supposed to impart torque 90° out of the clevis plane. These three drops will be discussed separately from the others.

Figures B1 - B12 give the spin histories of cable drops with 2.13-metre VRP whereas their yawing motions are plotted on Figures B13 - B24. An inspection of Figures B1 - B12 show that all but four drops have attained steady-state spin behavior by 4.5 seconds into the drop. Three drops which are exceptions (drops 5, 19, and 27) attain steady-state conditions between 5 and 6 seconds. The fourth drop, number 17, does not have any data until 7.5 seconds into the flight. Wherever early yawsonde data exist, the model/parachute appears to require about 1.5 seconds to reach the steady state. Once more, drops 19 and 27 appear to be exceptions. They have attained steady state in 2.5 - 3.0 seconds after the start of rotation. All drops with the 2.13-metre parachute achieved, on the average, a steady-state spin of 4.6 rps. All spin data plotted in Figures B1 - B12 show high frequency modulation whose oscillation rate is approximately equal to the average spin of the corresponding drop although the amplitude of the modulation varies from round to round.

Yawing behavior of these drops, Figures B13 - B24, show even greater variability. Although all drops attest to the bi-modal nature of the yawing motion of this payload/parachute combination, the modal content of each drop is different. Cable drops 2, 8, 9, and 19 (Figures B13, B16, B17, and B23, respectively) show an almost equal amplitude of fast and slow modal arms. On the other hand, drops 6, 13, 14, 16, and 17 (Figures B15, B19, B20, B21, and B22, respectively) show a dominant high-frequency mode. Drops 10 and 27 (Figures B18 and B24, respectively) show yawing motions where the relationship between the two modes vary during the drop. Although a relatively constant amplitude fast mode persists throughout these drops, both show a sudden appearance of a slow frequency mode of sizable amplitude. Finally, cable drop 5 (Figure B14) show a complete lack of fast frequency component during the steady-state portion of the drop. In spite of this apparent variability in the yawing behavior of this system, the motion is consistent in that, when detectable, the fast mode has a frequency approximately equal to the average spin of the system and the slow frequency is approximately one (1) Hertz which is the system's pendular frequency.

The spin and yaw data for the cable drops 28 and 30 are plotted on Figures B25 - B28. Figures B25 and B26 give the spin histories of drops 28 and 30, respectively. Similar to the other drops using the 2.13-metre VRP, about 4.5 seconds are required to reach a steady-state spin rate whose average value is 4.7 rps. They also show the same fast frequency modulation. The yawing behavior of these drops shown in Figures B27 and B28. As the previously discussed data, these two Figures show bi-modal behavior of varying modal content. Although two drops do not form a sufficient statistical base, it may be concluded that the modified link did not alter the dynamic behavior of the system.

Figures B29 and B30 show the spin and yaw behaviors of cable drop 25, respectively. This drop used the 1.83-metre VRP similar to drop 18 discussed in the main body of the report. Although there were four additional drops with that parachute, data reduction problems precluded their immediate analyses. Behavior of this drop is quite similar to that of drop 18. The system reaches the average steady-state spin of 6 rps at 7.5 seconds into the drop. The system is once more bi-modal in behavior although the modal amplitudes for this drop are different than the yawing motion of cable drop 18.

At the beginning of each yawsonde plot, there appears to be a region of irregular motion. These segments must be ignored as part of the dynamic behavior of the parachute/warhead system since our method of yawsonde analysis will produce questionable results in regions of strongly transient spin. The gaps in the data are caused by the editing of noise which was present during portions of the drops. This noise was most likely due to the loose coupling between parachute and payload through a slip-cup assembly. The mechanical friction and rubbing in the cup could produce radio interference, particularly at L-band.

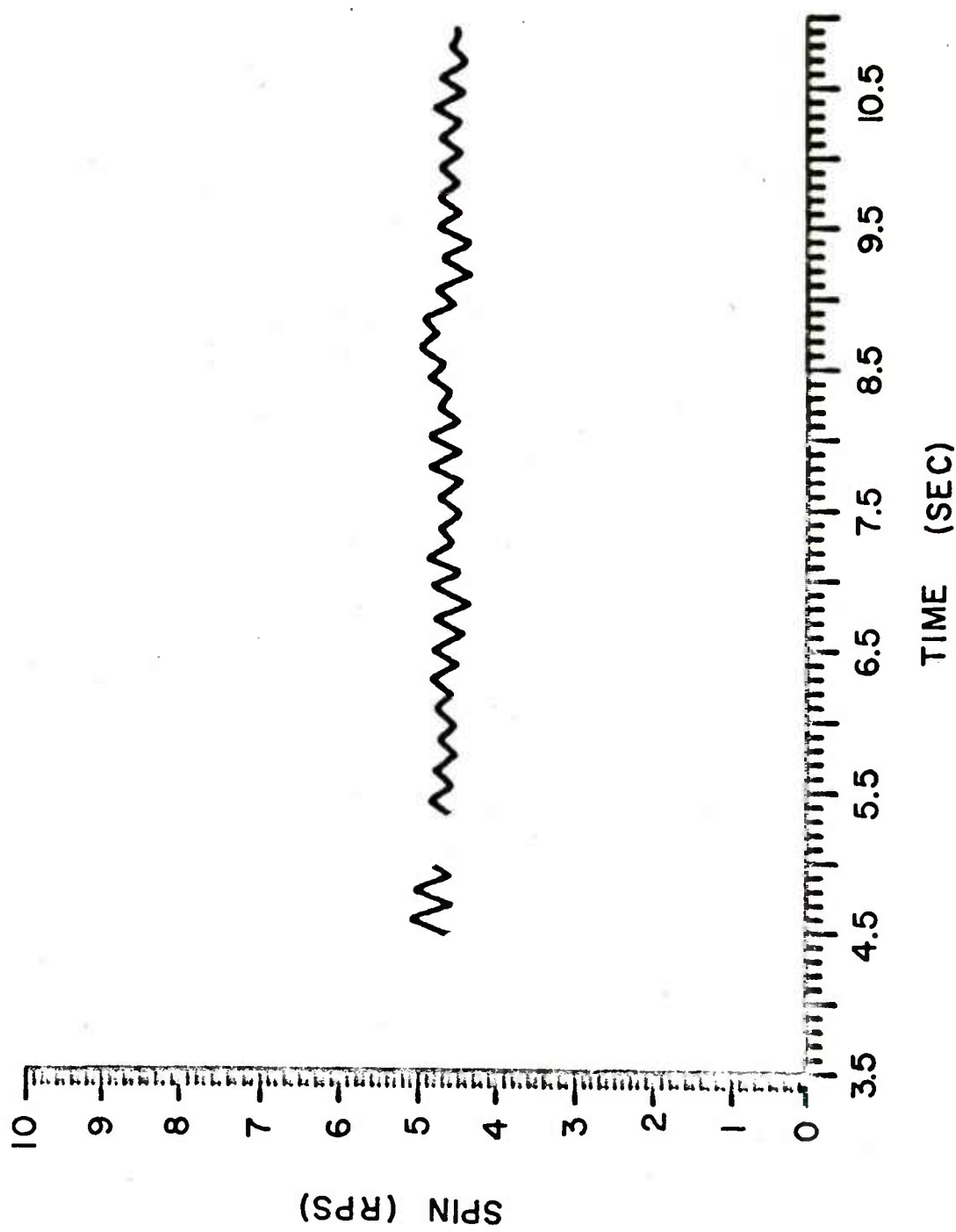


FIGURE B1. SPIN VERSUS TIME FOR CABLE DROP 2

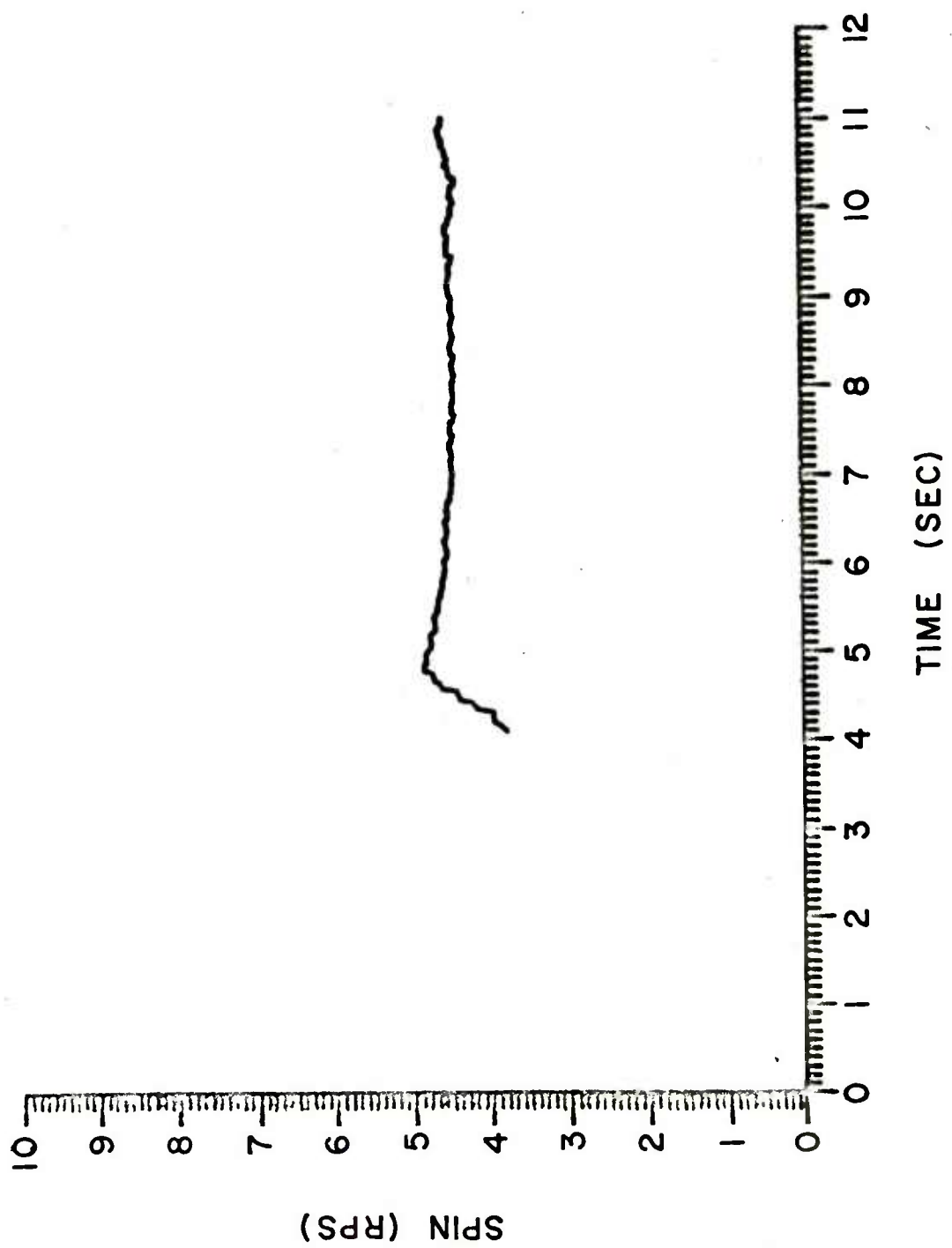


FIGURE B2. SPIN VERSUS TIME FOR CABLE DROP 5

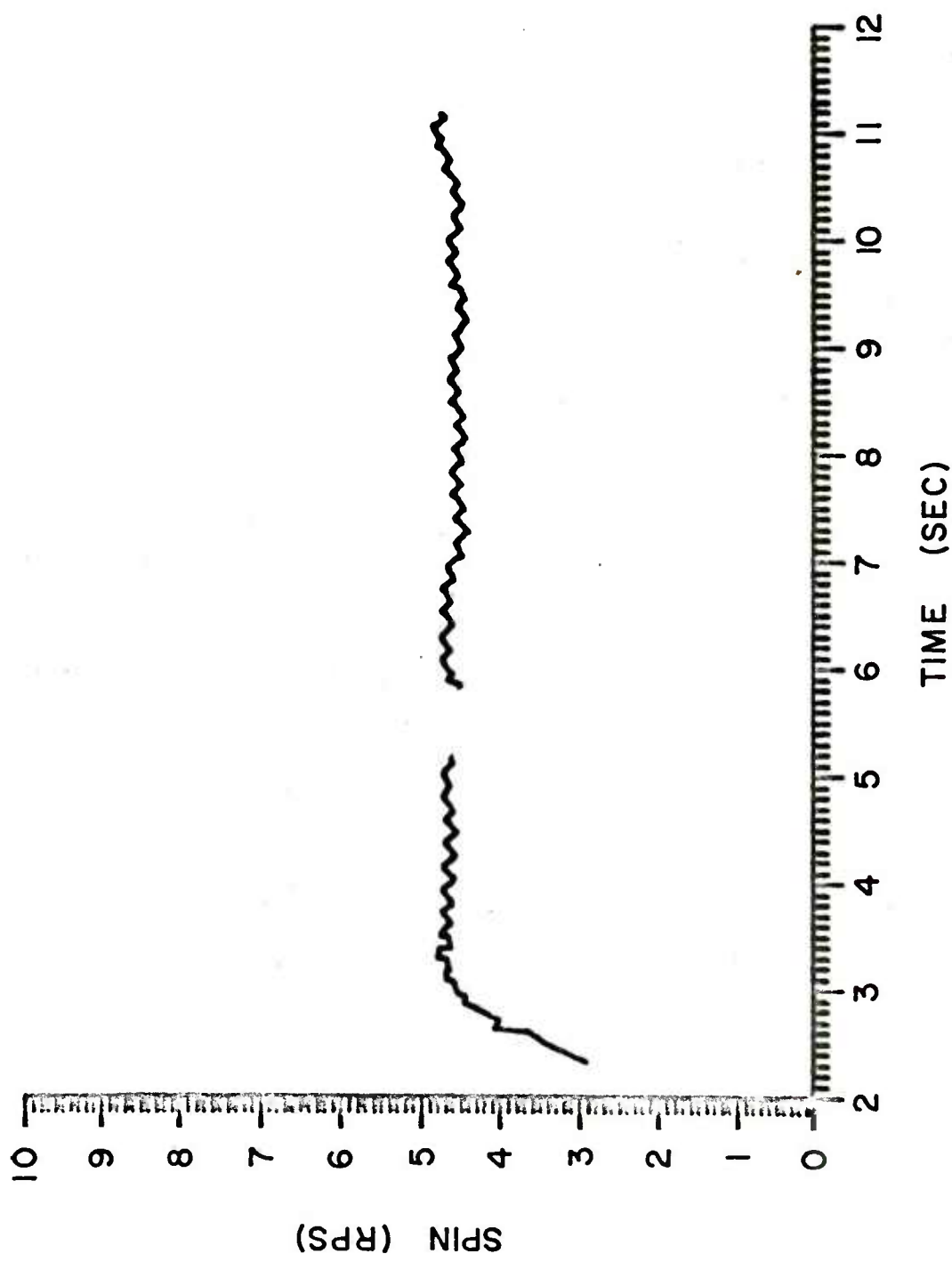


FIGURE B3. SPIN VERSUS TIME FOR CABLE DROP 6

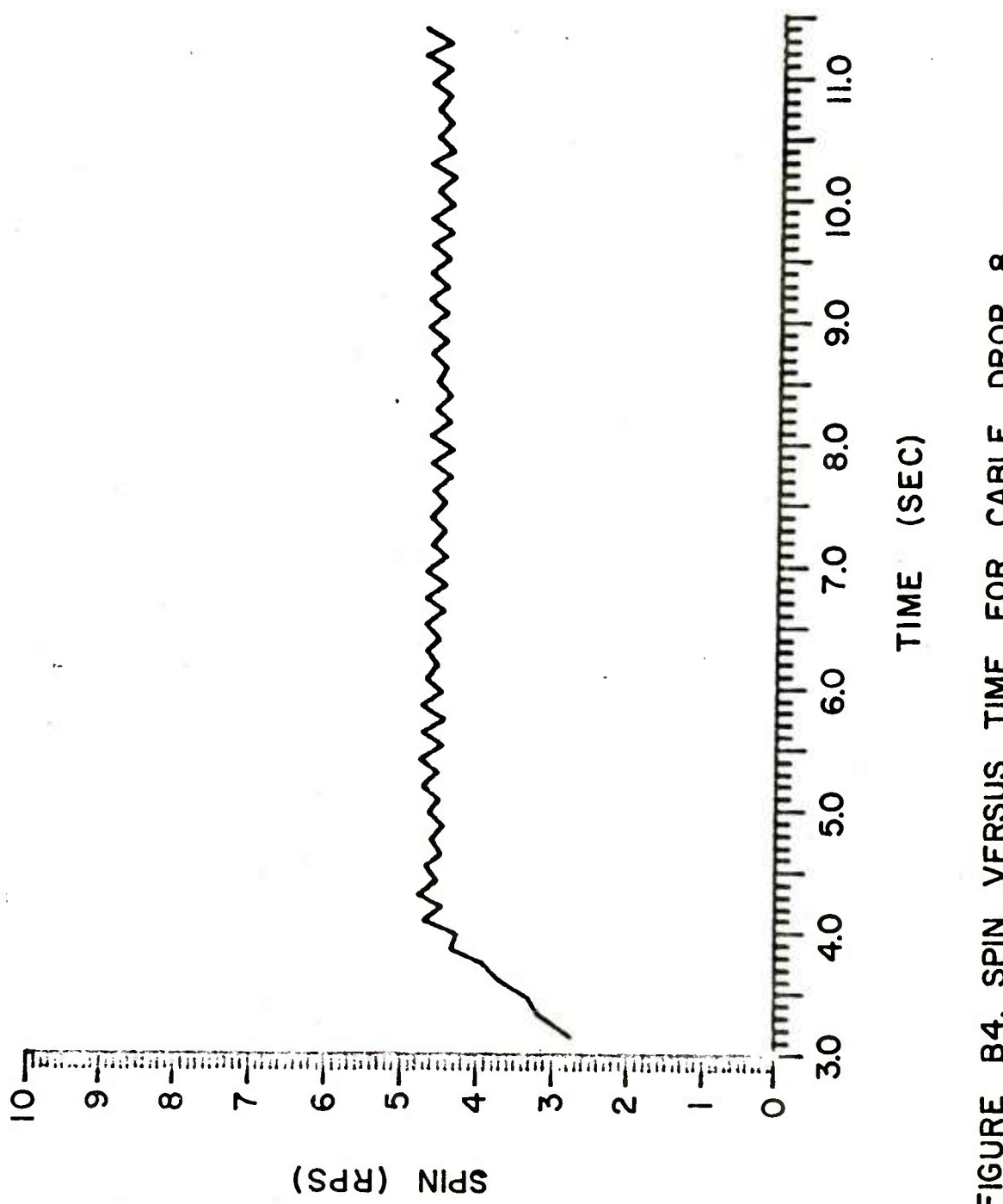


FIGURE B4. SPIN VERSUS TIME FOR CABLE DROP 8

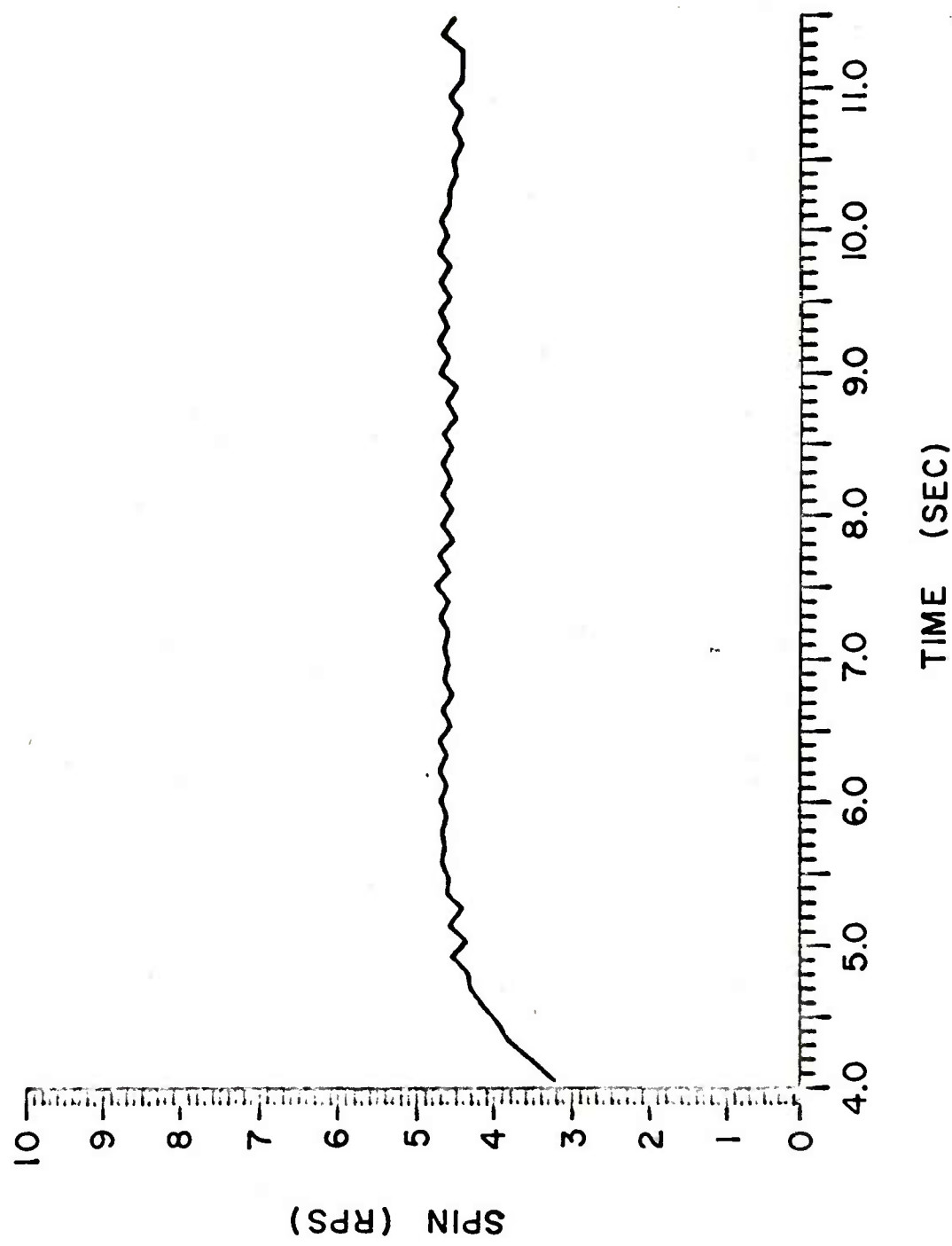


FIGURE B5. SPIN VERSUS TIME FOR CABLE DROP 9

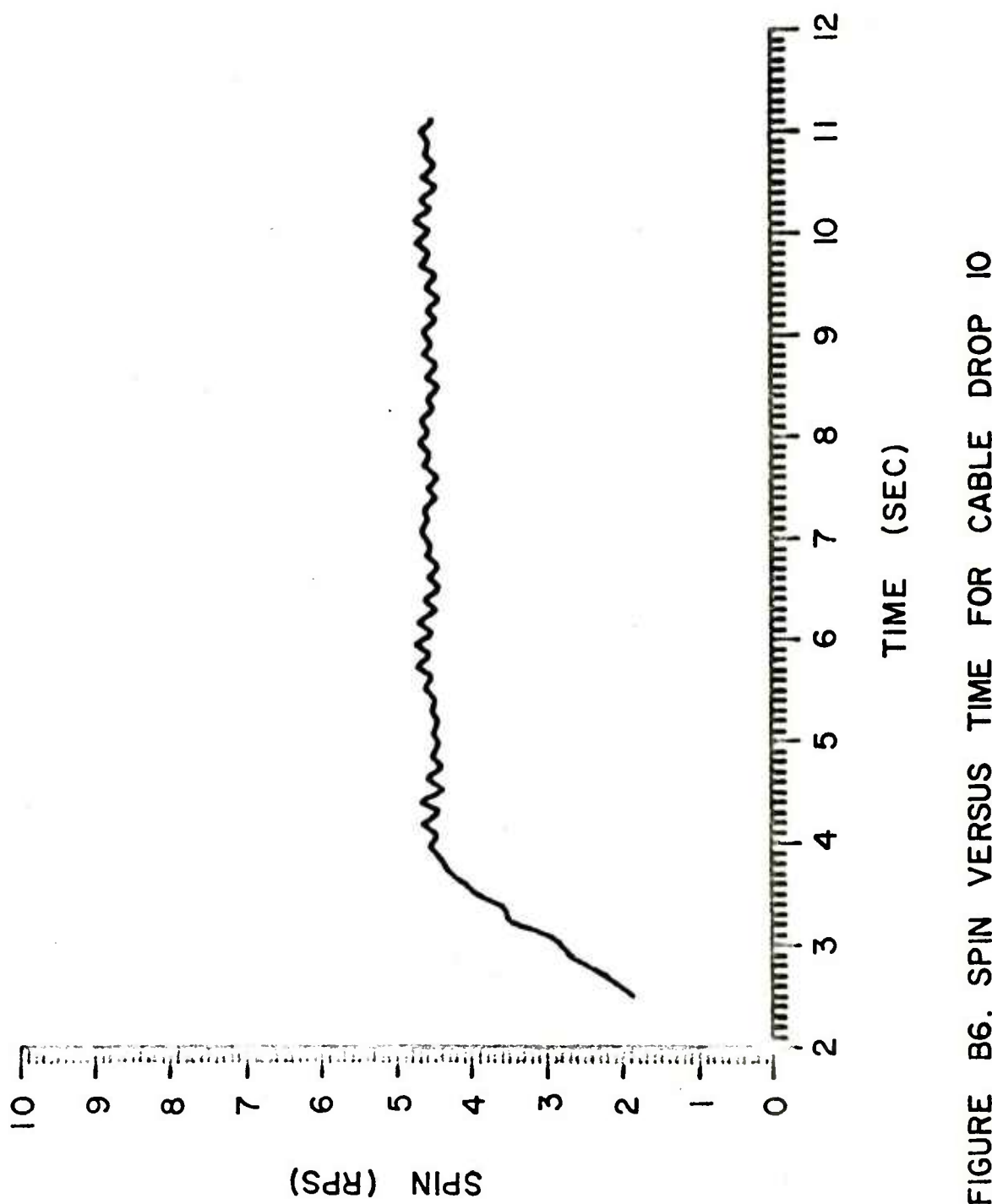


FIGURE B6. SPIN VERSUS TIME FOR CABLE DROP 10

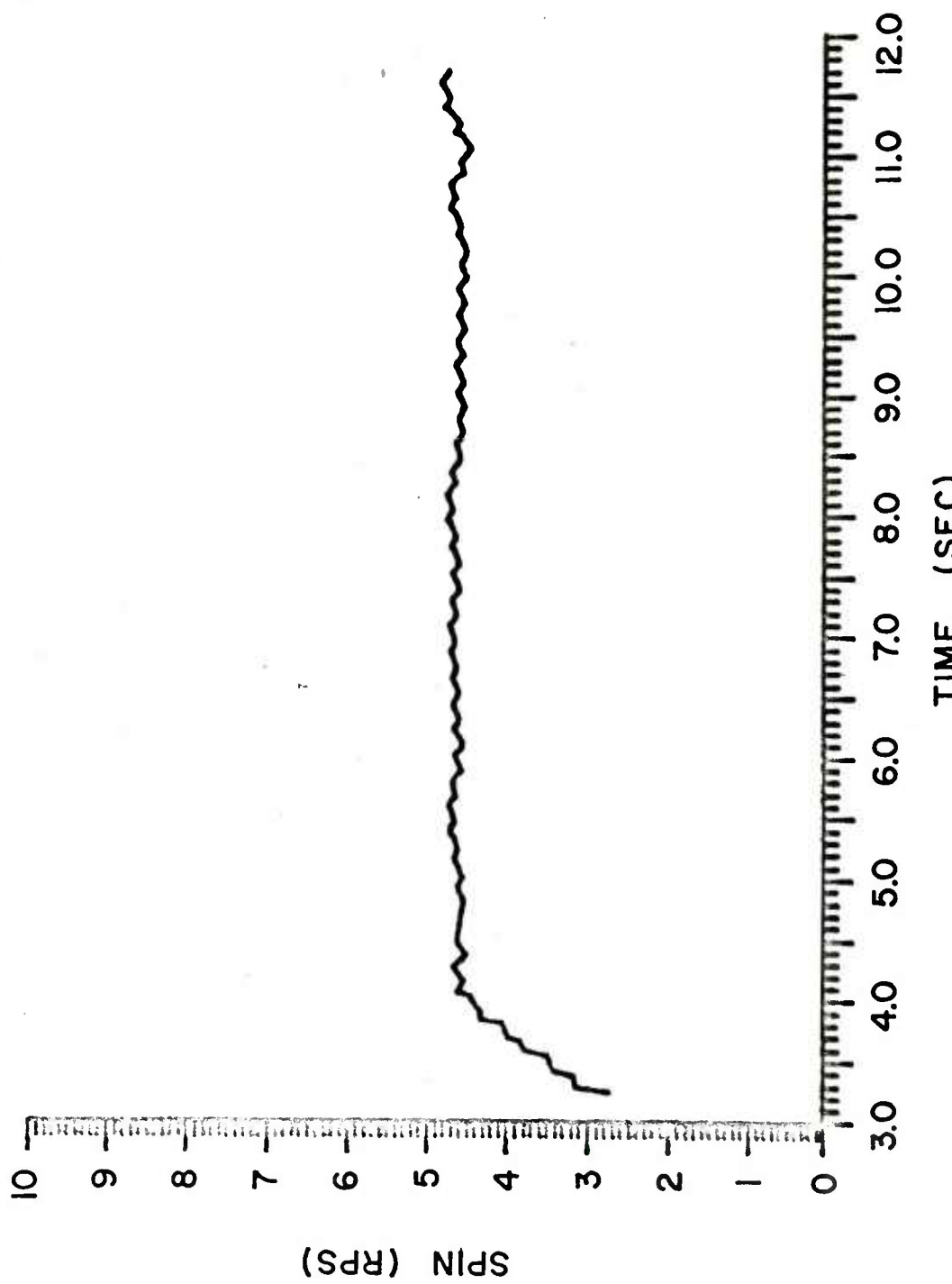


FIGURE B7. SPIN VERSUS TIME FOR CABLE DROP 13

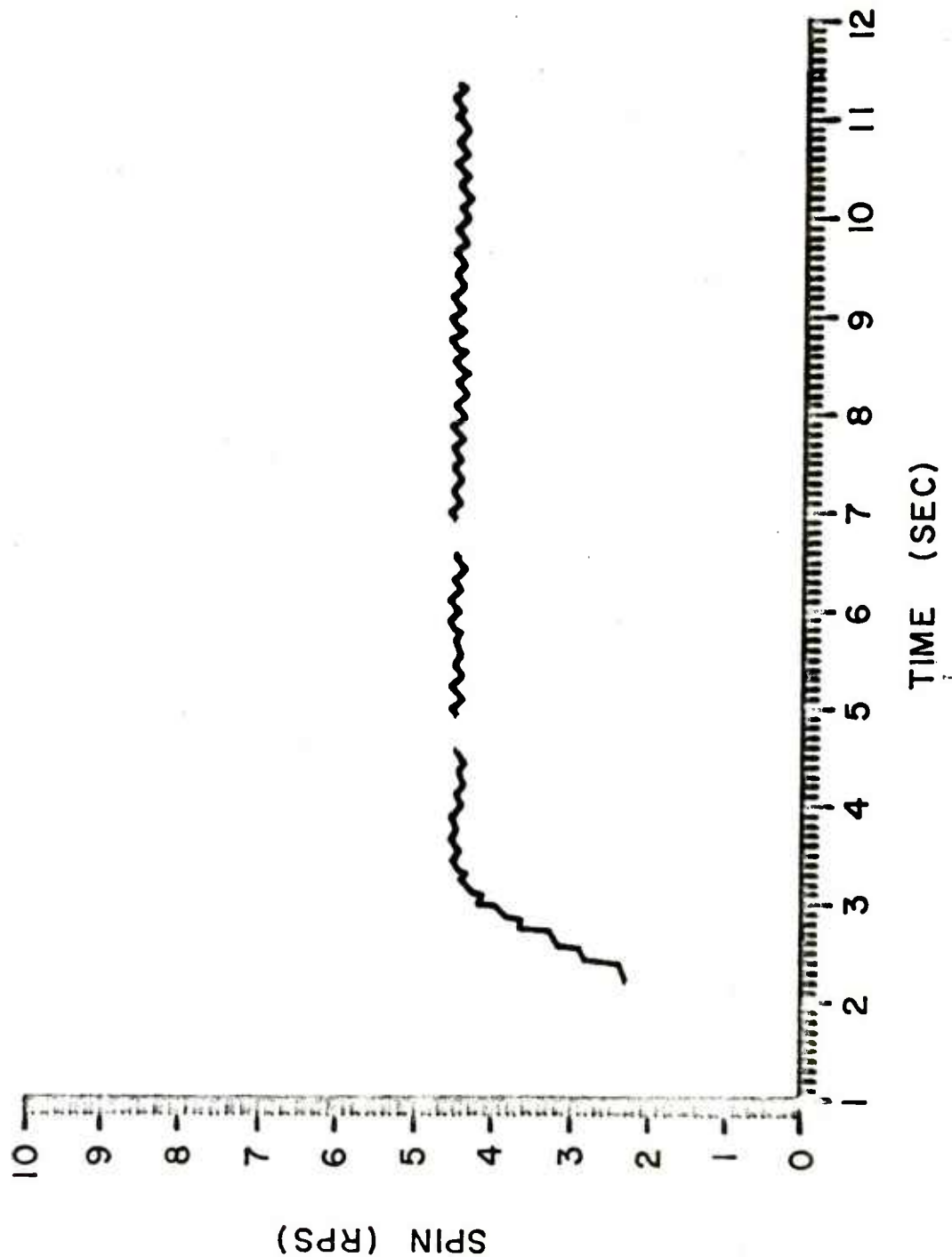


FIGURE B8. SPIN VERSUS TIME FOR CABLE DROP 14

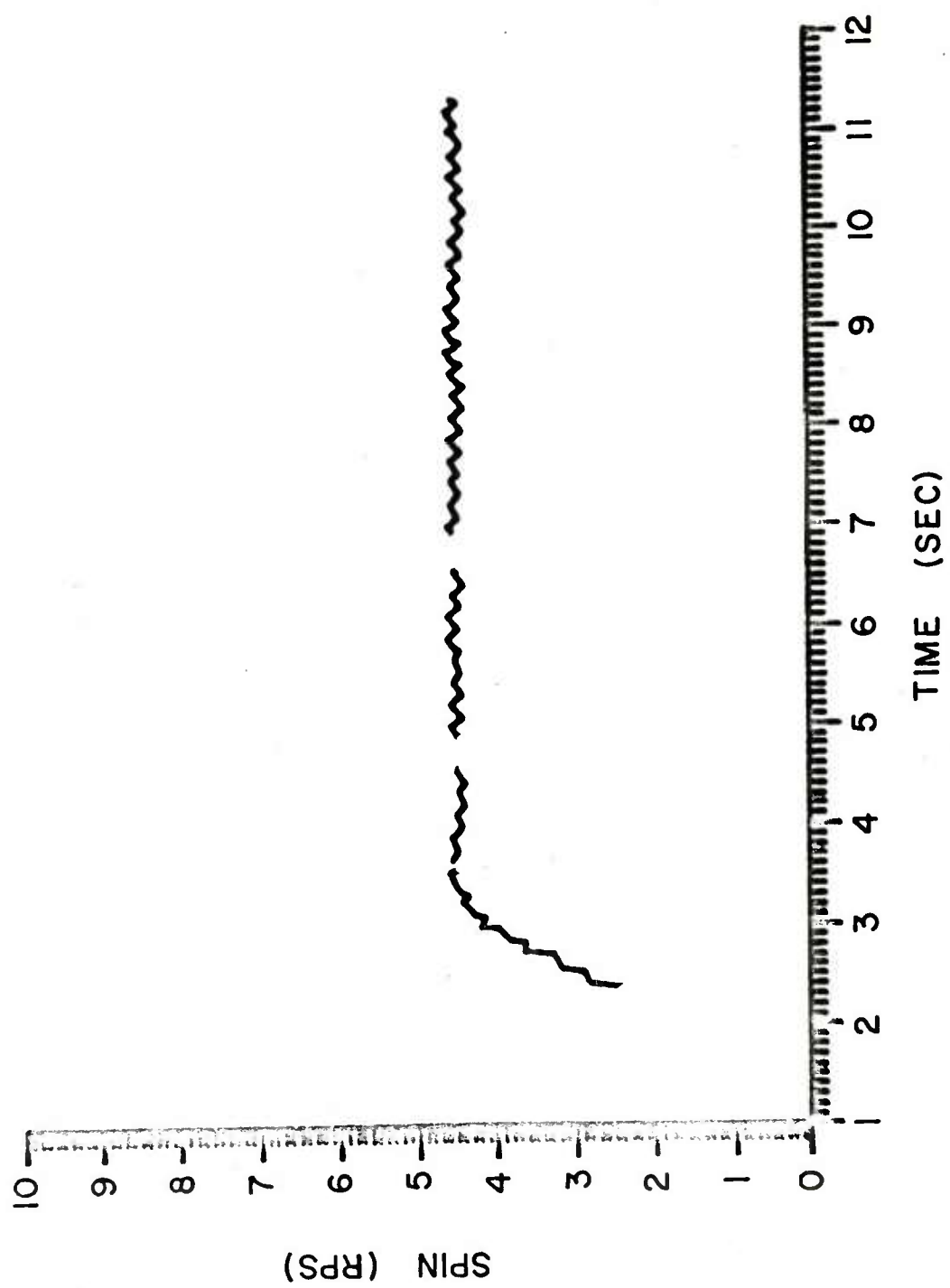


FIGURE B9. SPIN VERSUS TIME FOR CABLE DROP 16

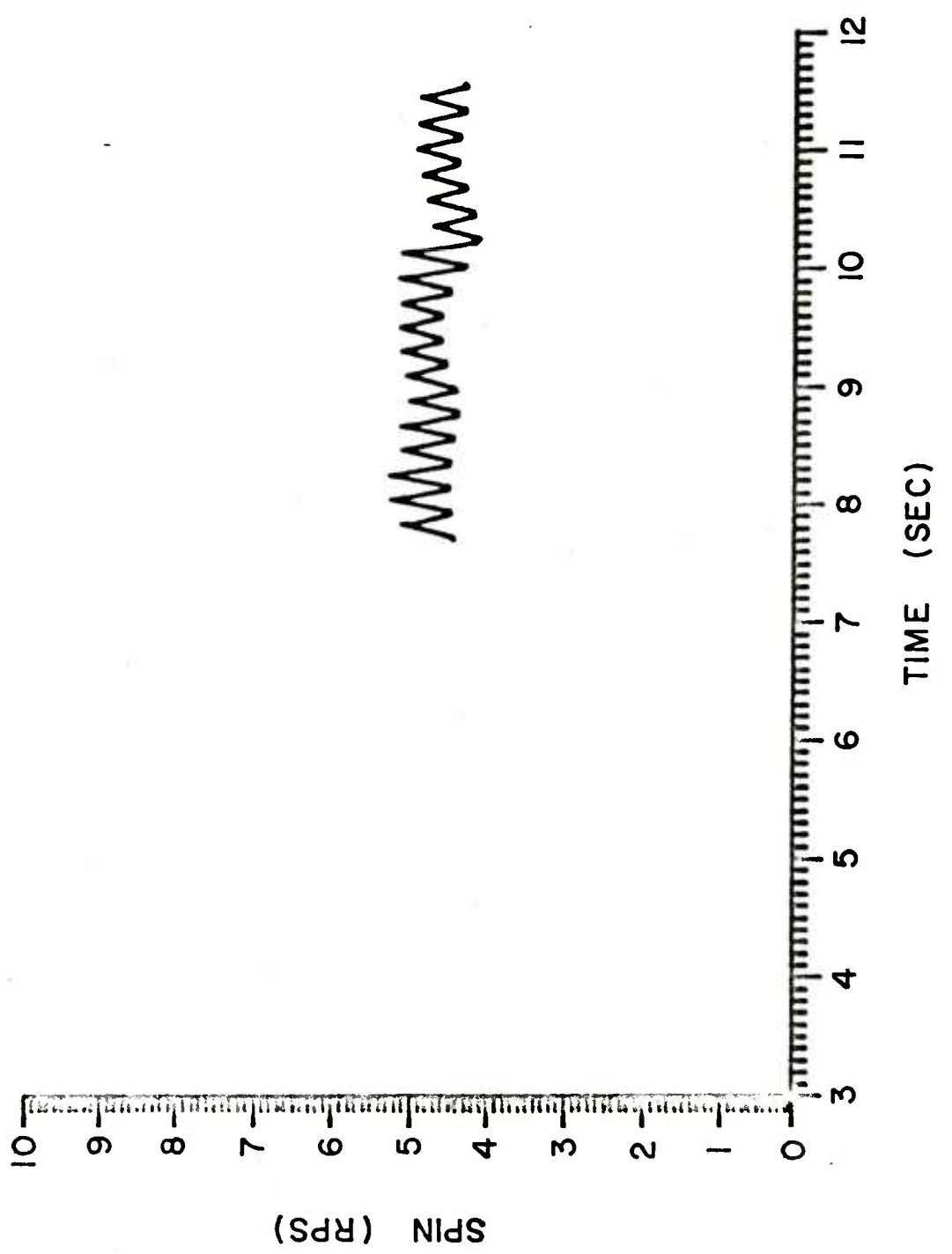


FIGURE BIO. SPIN VERSUS TIME FOR CABLE DROP 17

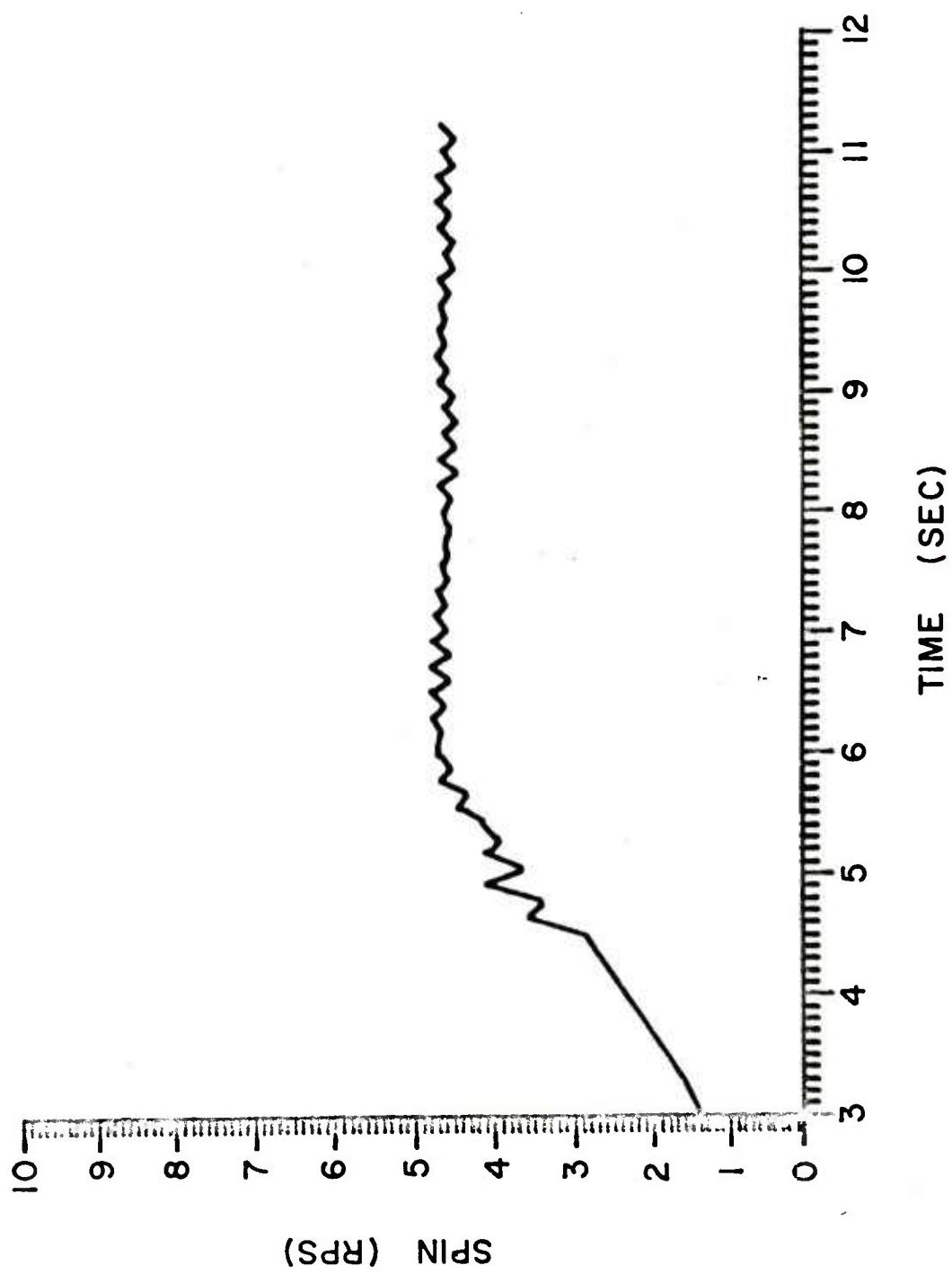


FIGURE BII. SPIN VERSUS TIME FOR CABLE DROP 19

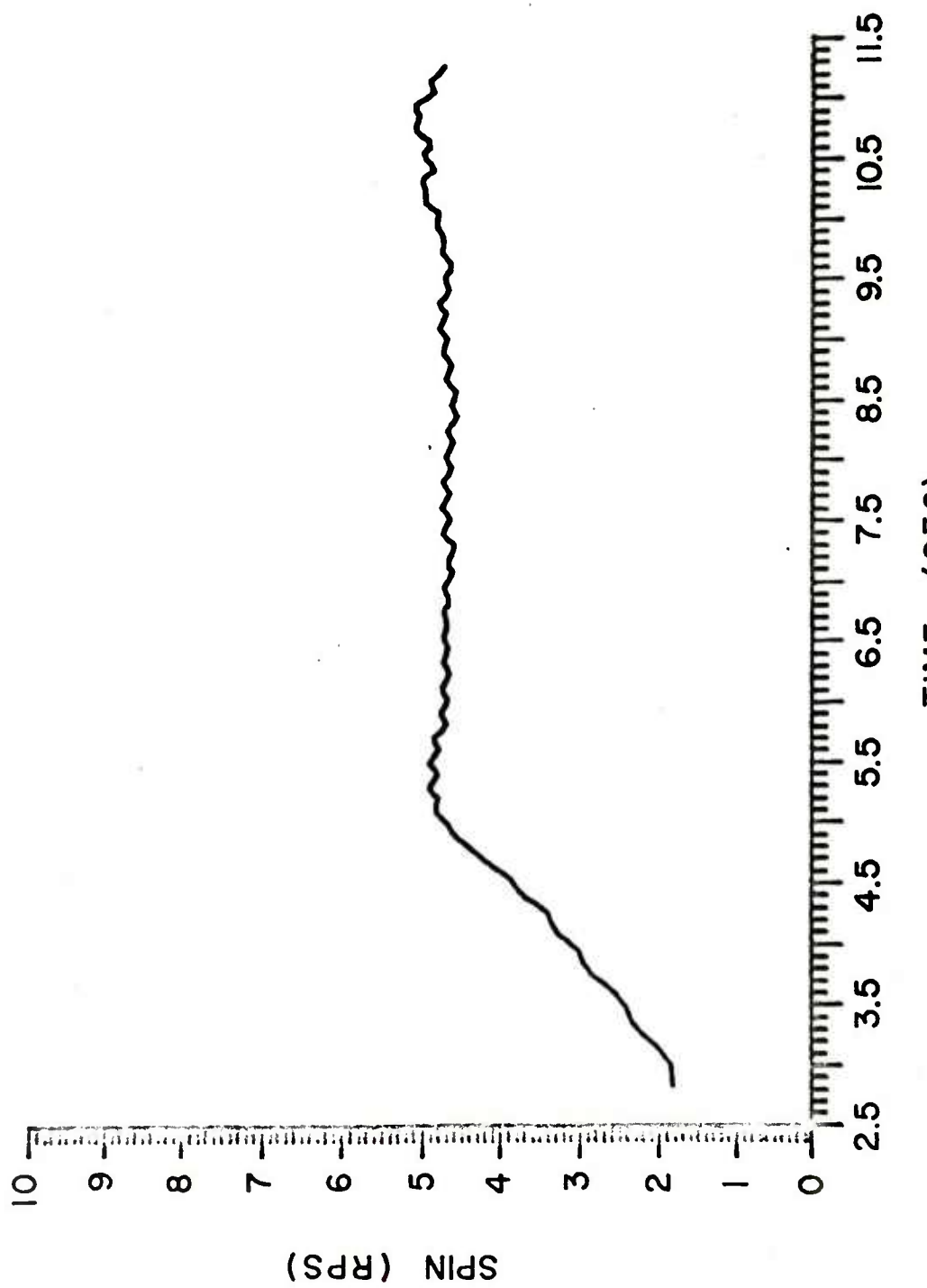


FIGURE B12. SPIN VERSUS TIME FOR CABLE DROP 27

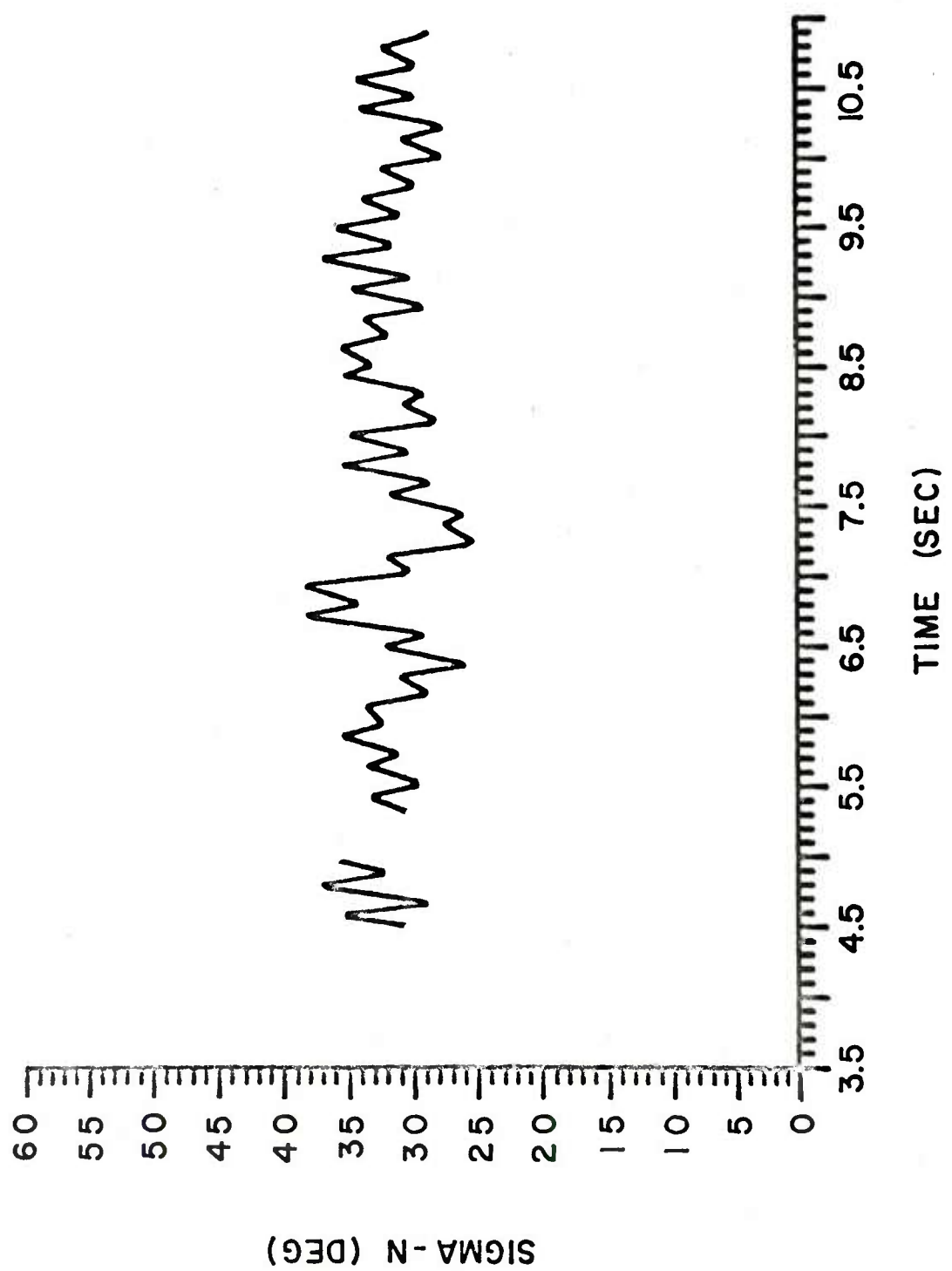


FIGURE BI3. YAW VERSUS TIME FOR CABLE DROP 2

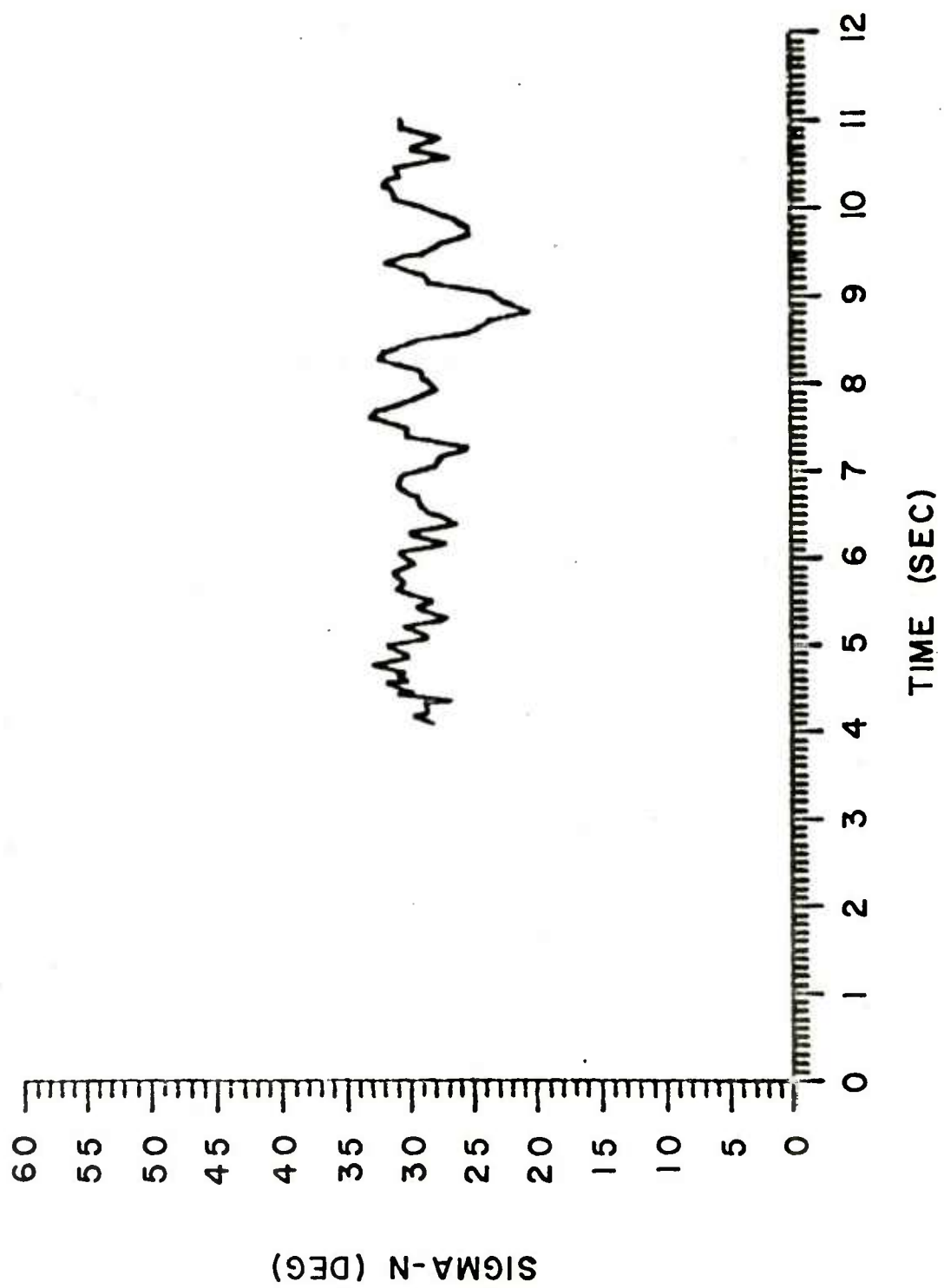


FIGURE B14. YAW VERSUS TIME FOR CABLE DROP 5

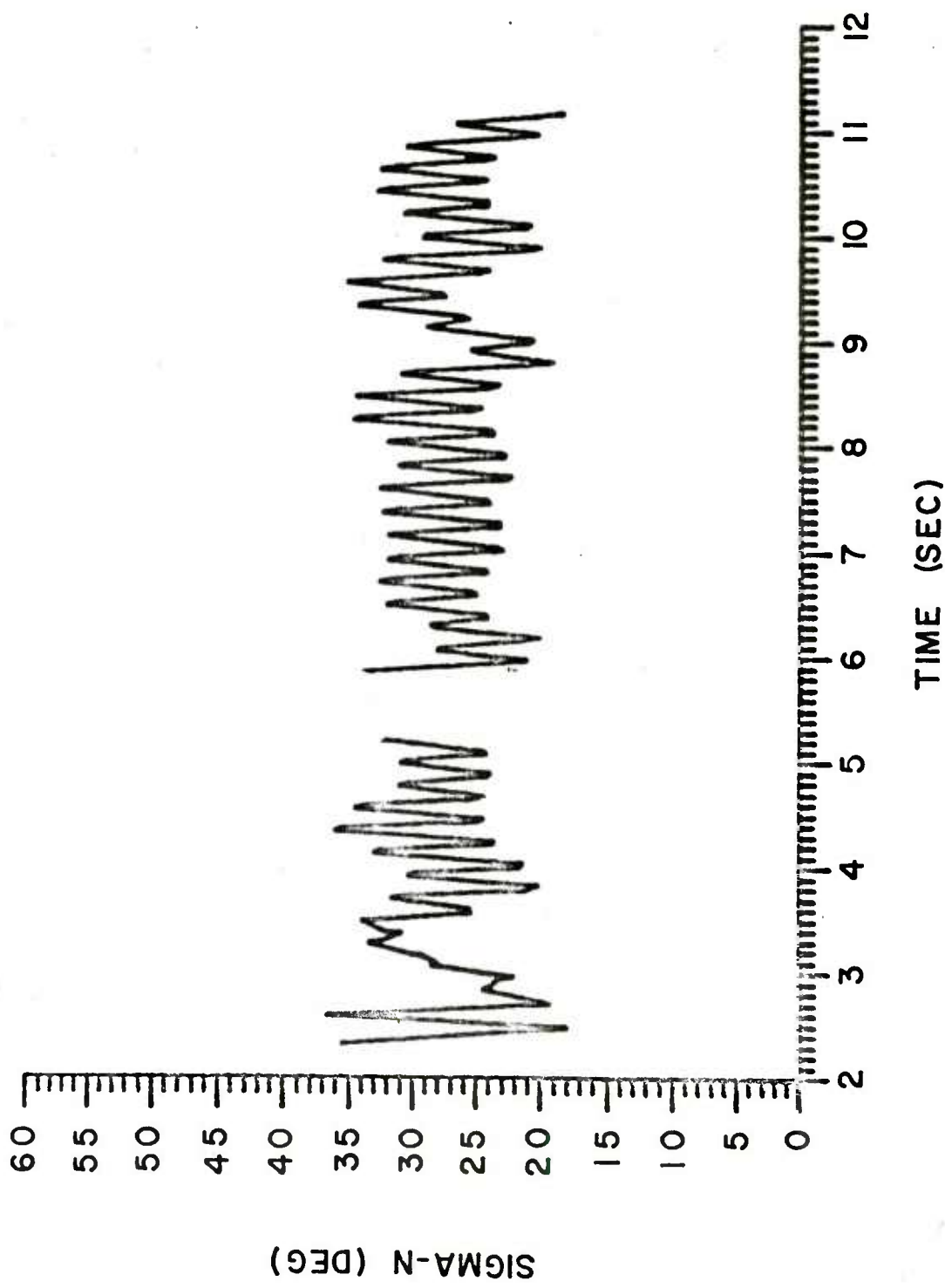


FIGURE B15. YAW VERSUS TIME FOR CABLE DROP 6

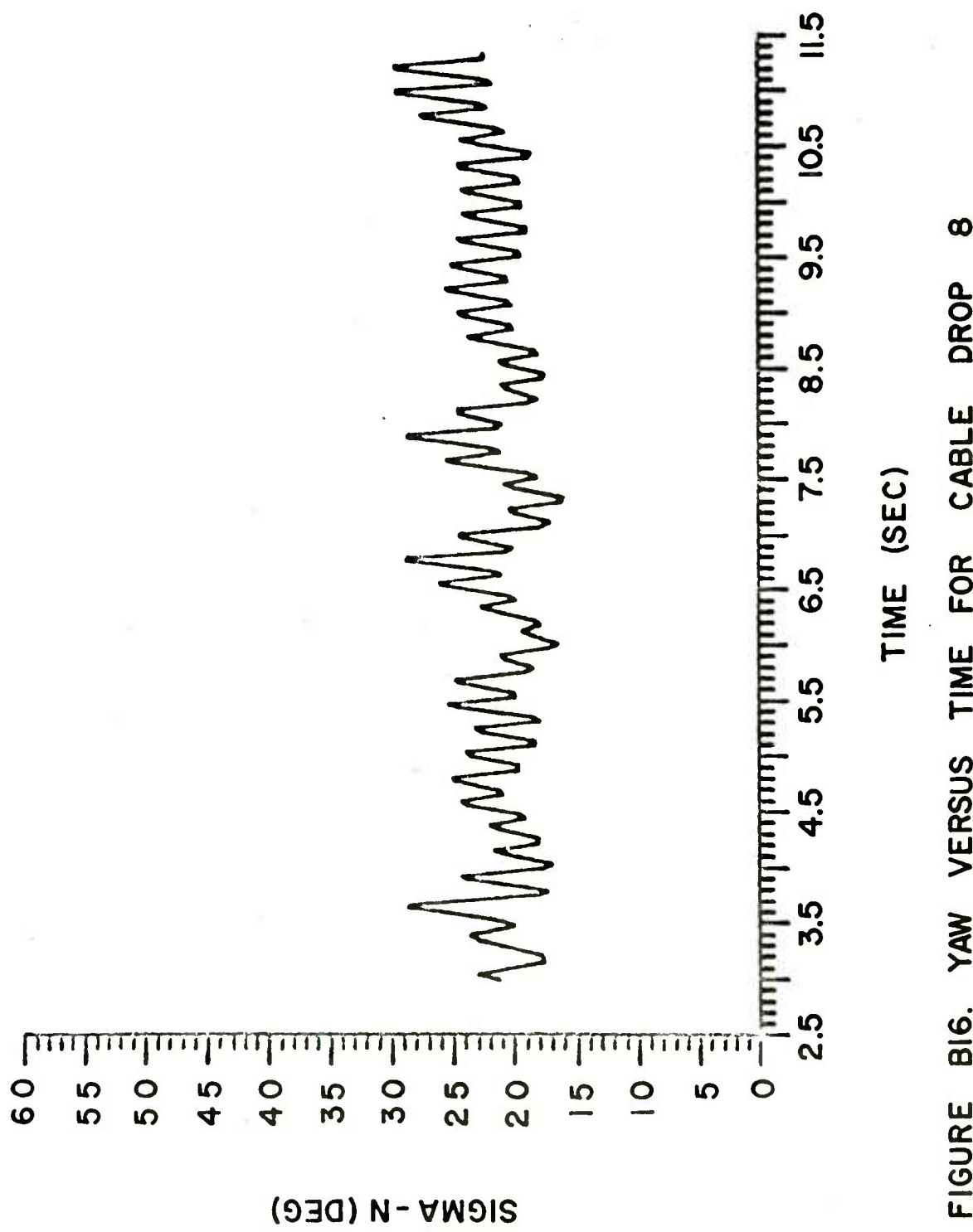
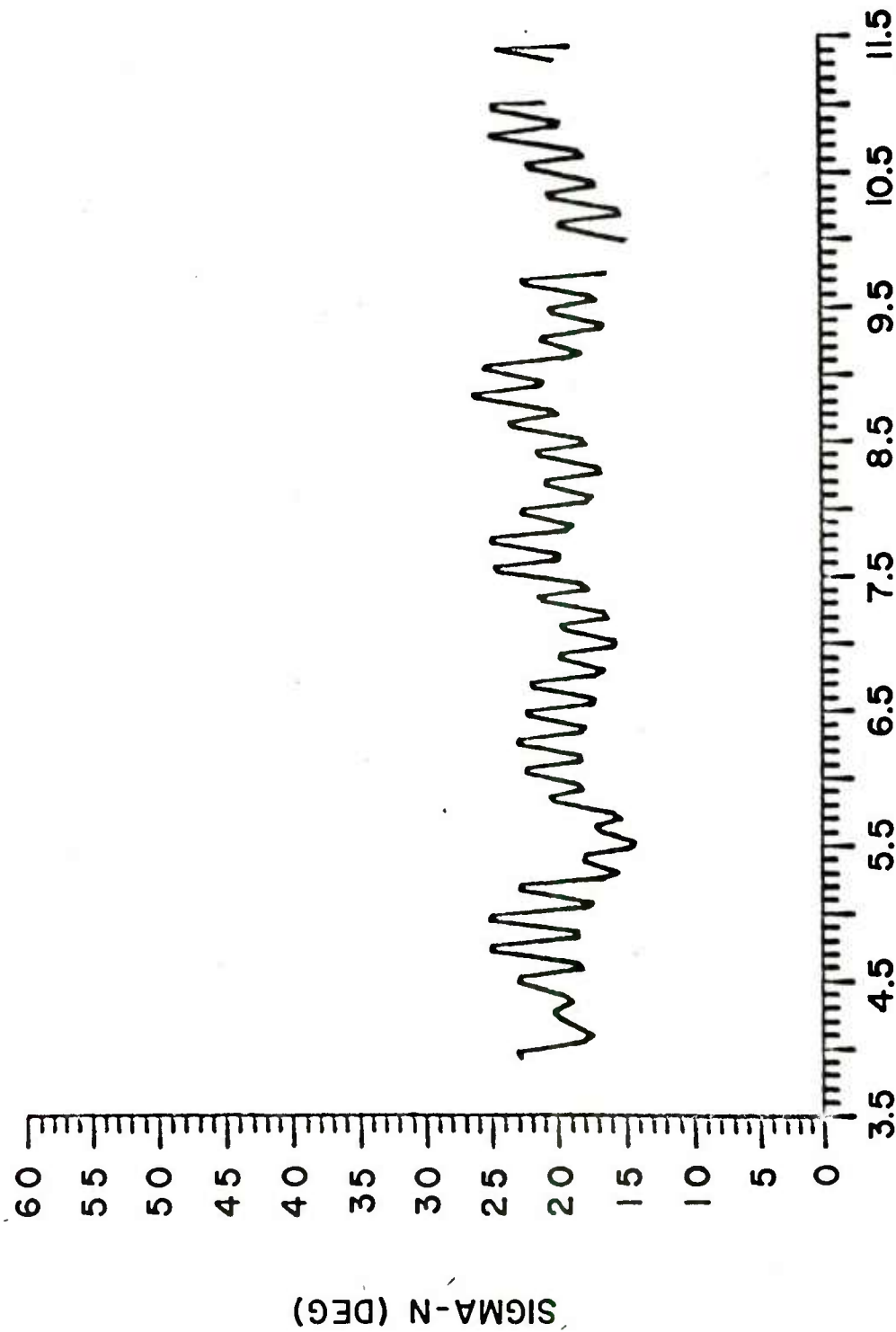


FIGURE B17. YAW VERSUS TIME FOR CABLE DROP 9



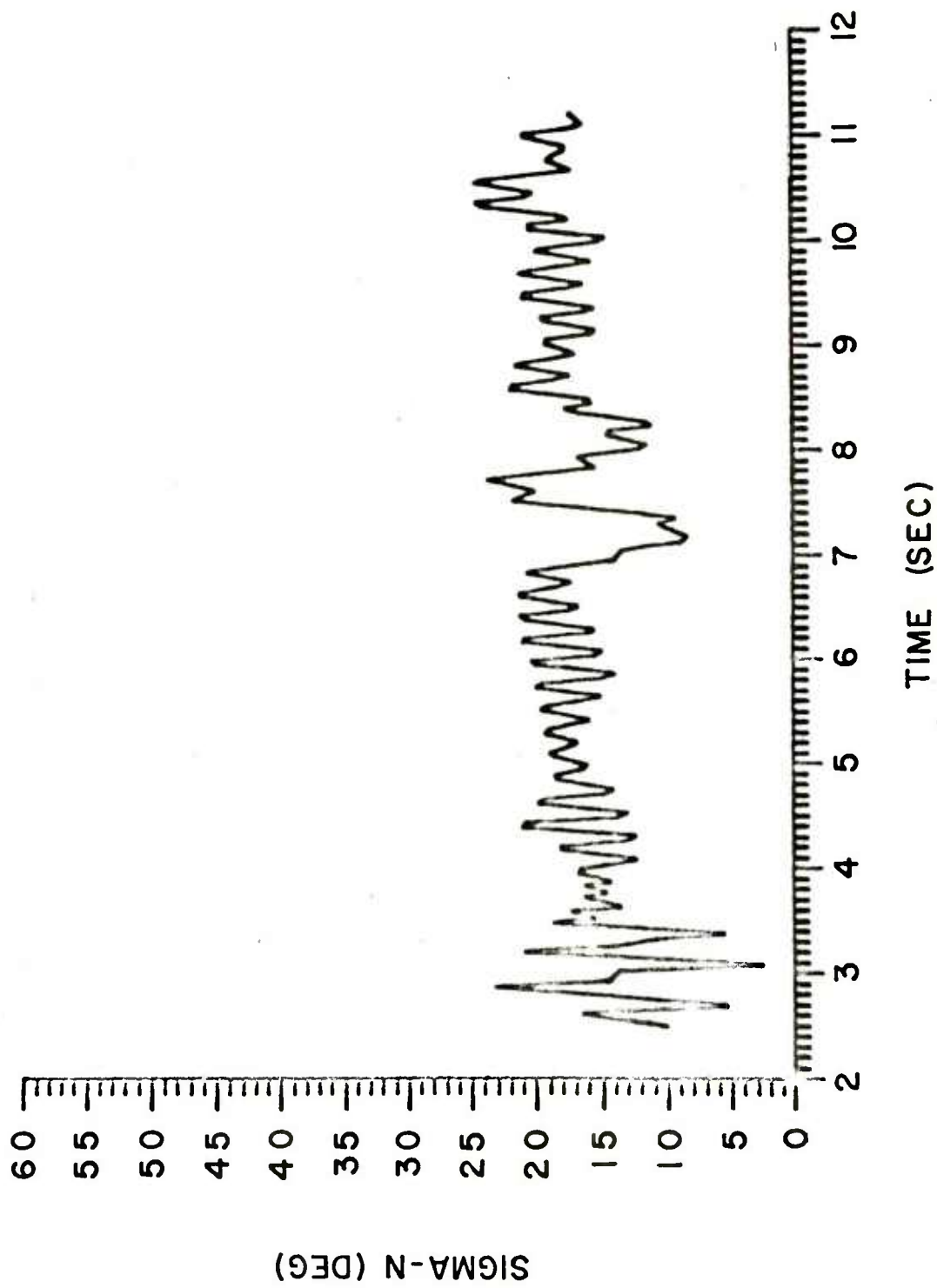


FIGURE B18. YAW VERSUS TIME FOR CABLE DROP 10

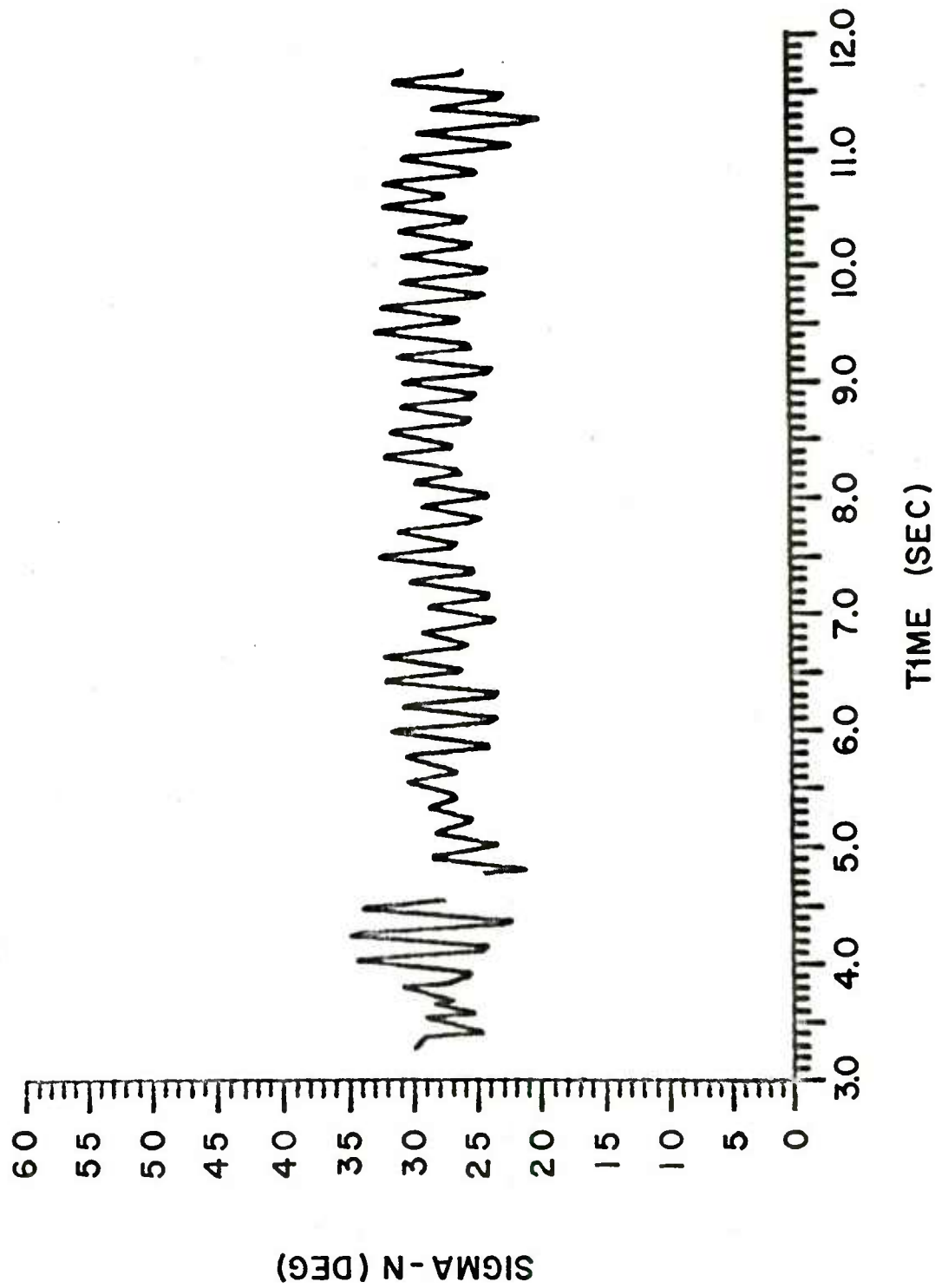


FIGURE B19. YAW VERSUS TIME FOR CABLE DROP 13

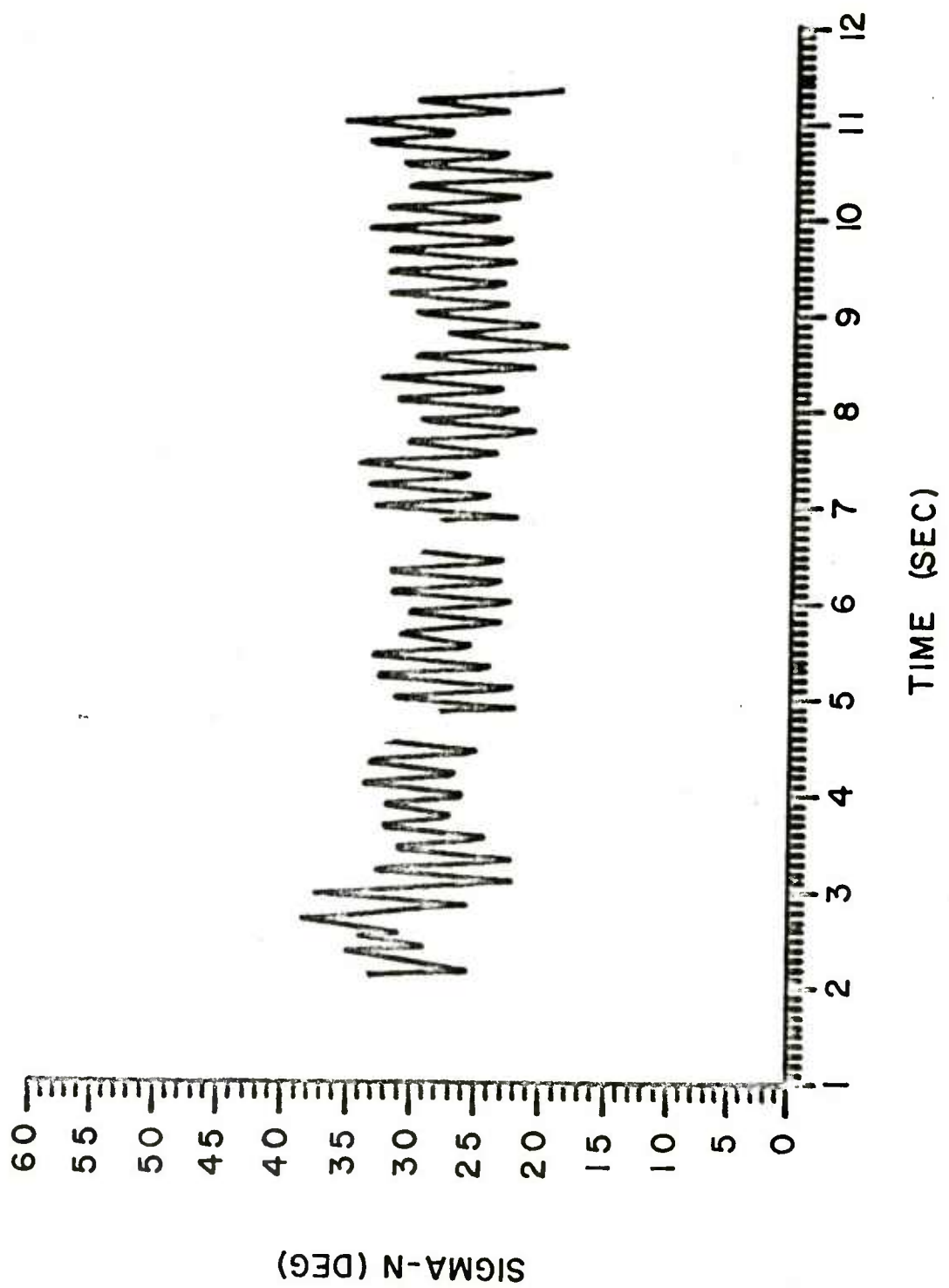
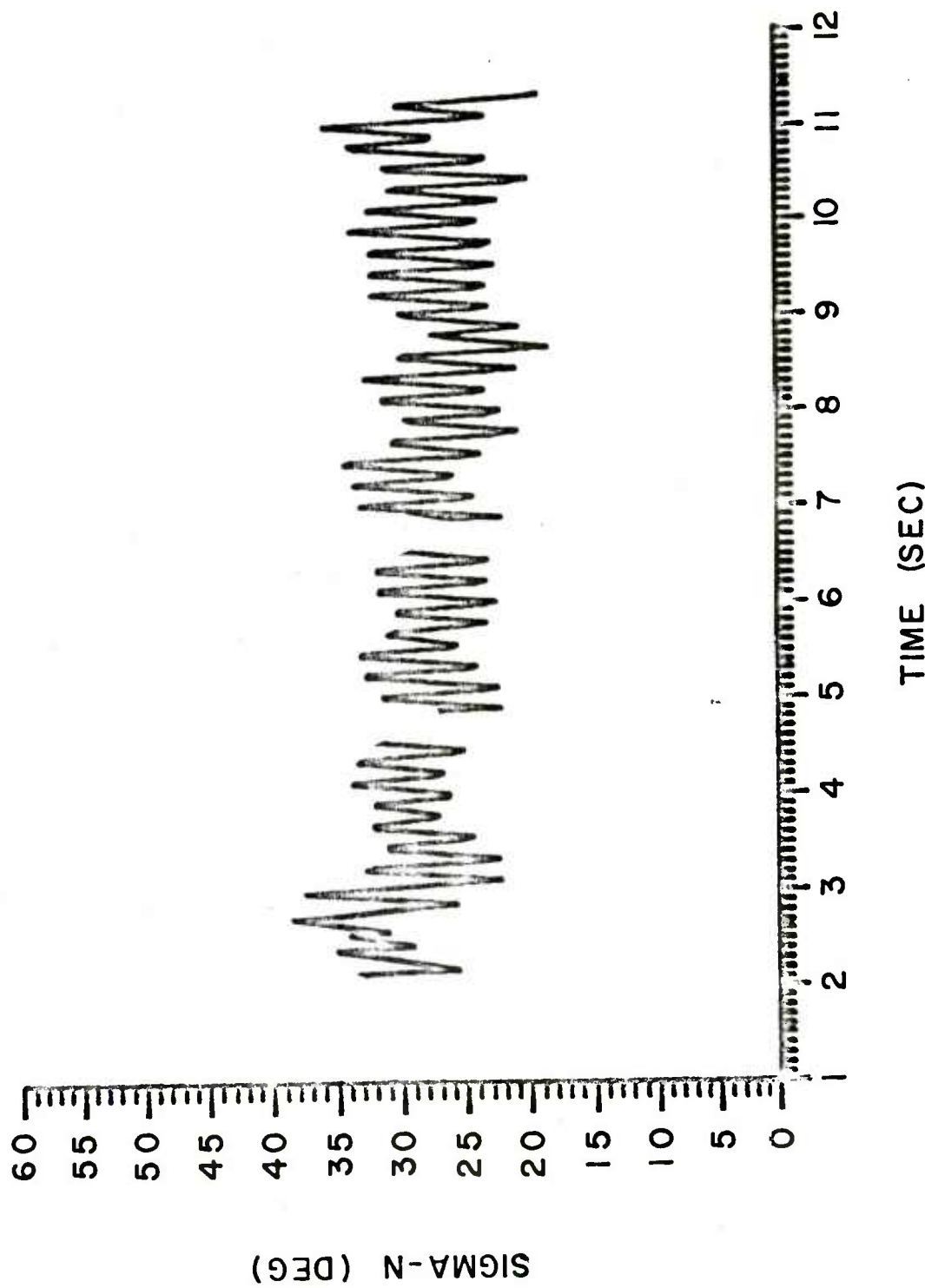


FIGURE B20. YAW VERSUS TIME FOR CABLE DROP 14



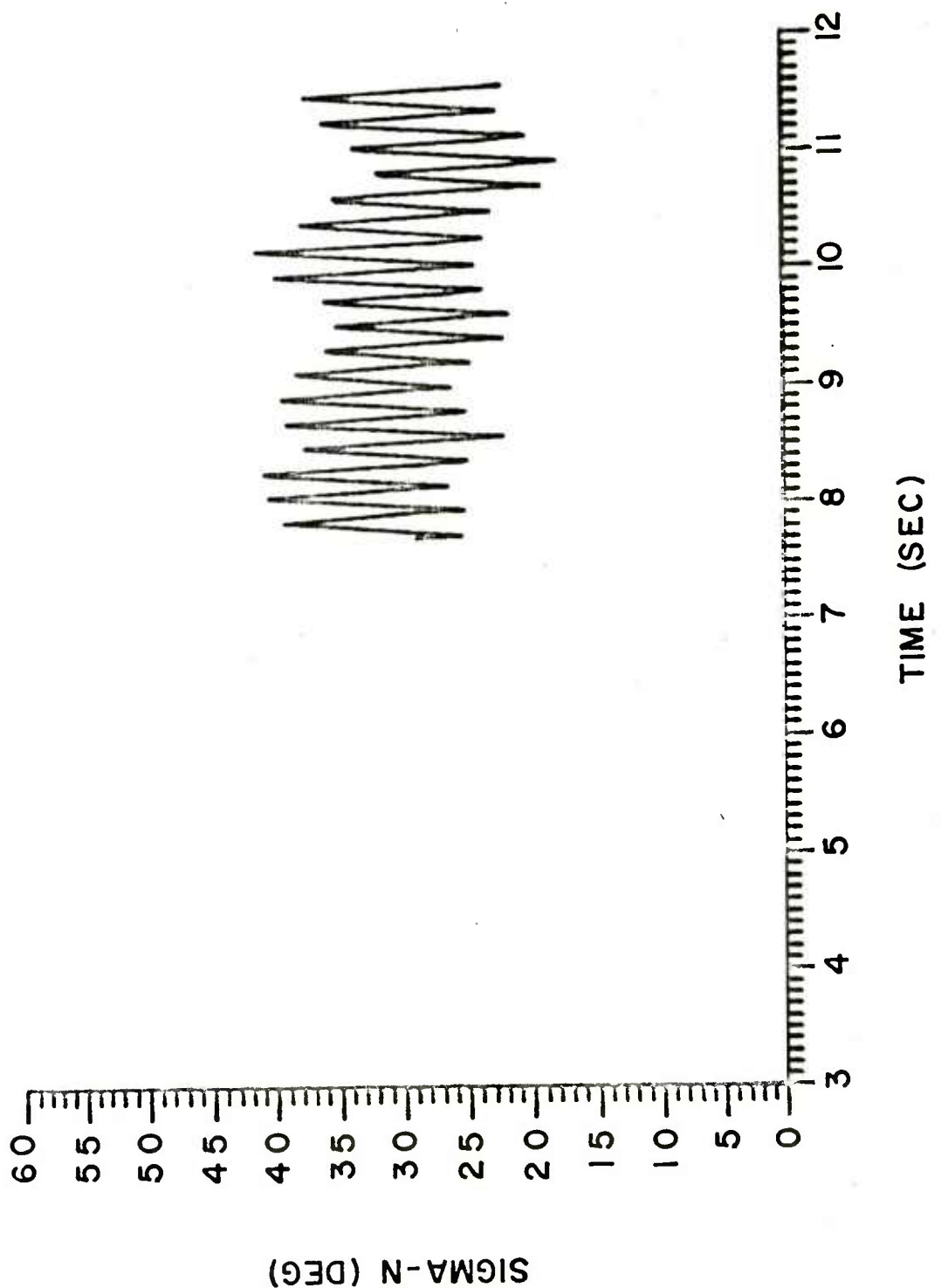


FIGURE B22 YAW VERSUS TIME FOR CABLE DROP 17

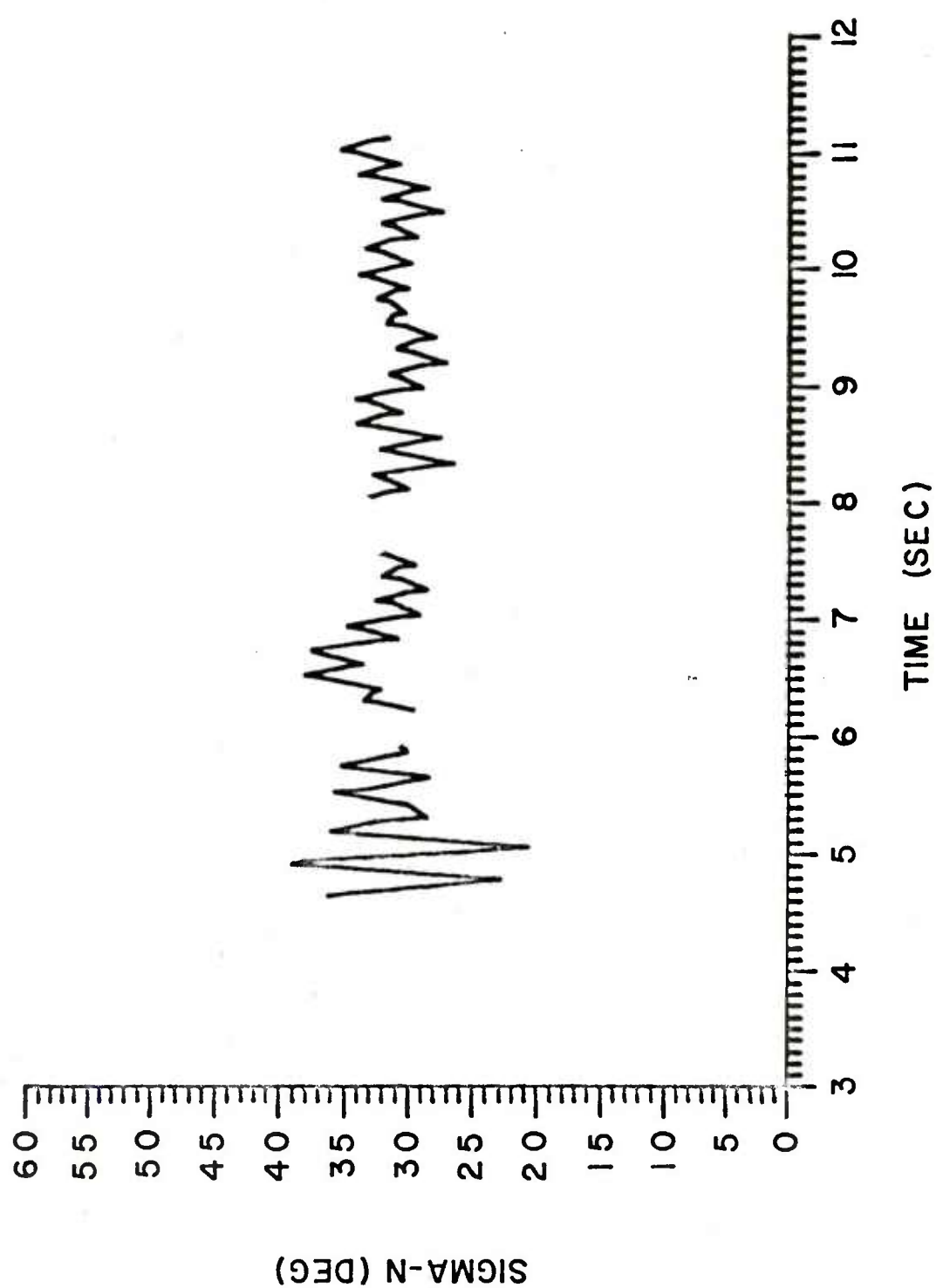


FIGURE B23. YAW VERSUS TIME FOR CABLE DROP 19

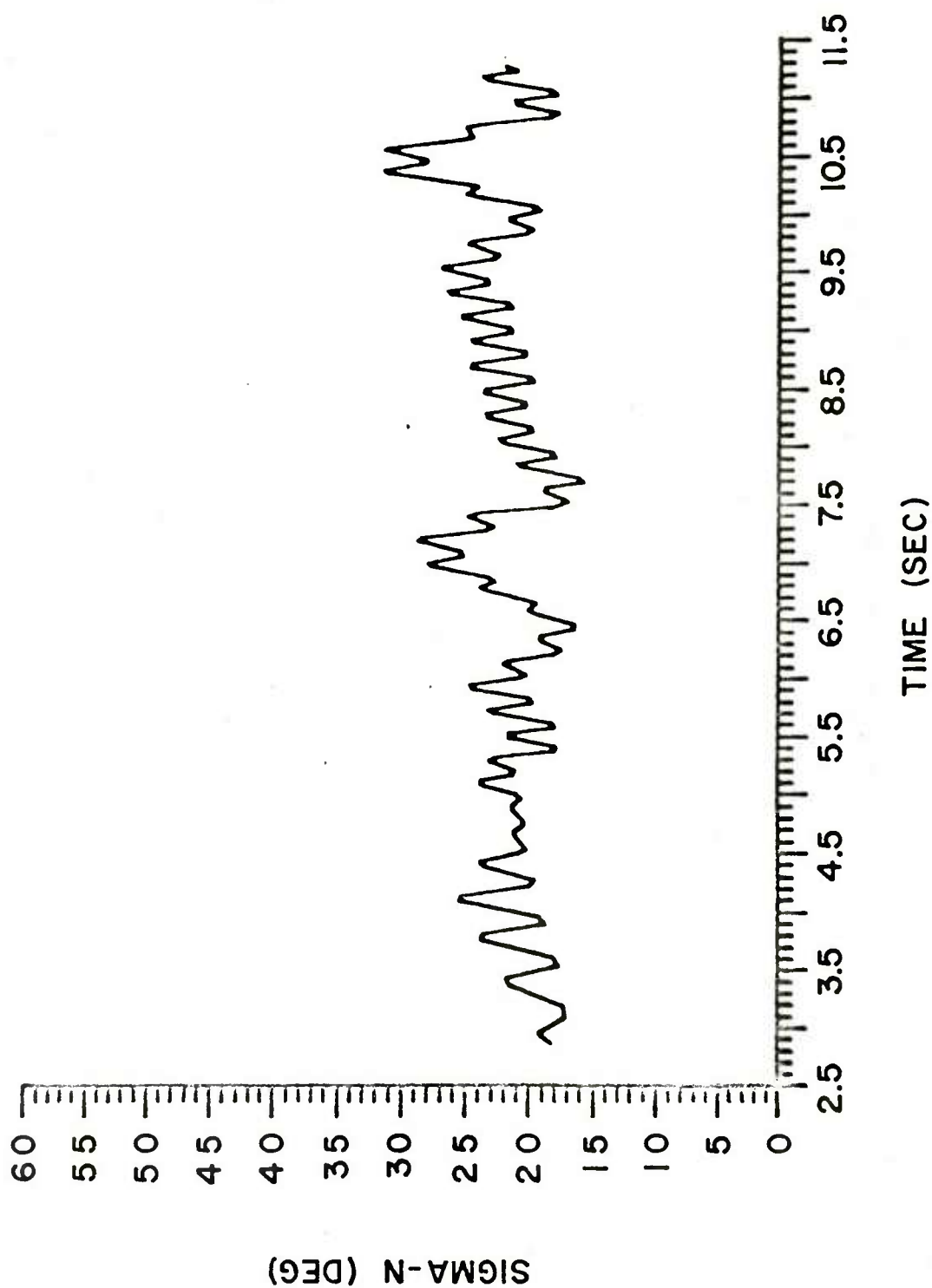


FIGURE B24. YAW VERSUS TIME FOR CABLE DROP 27

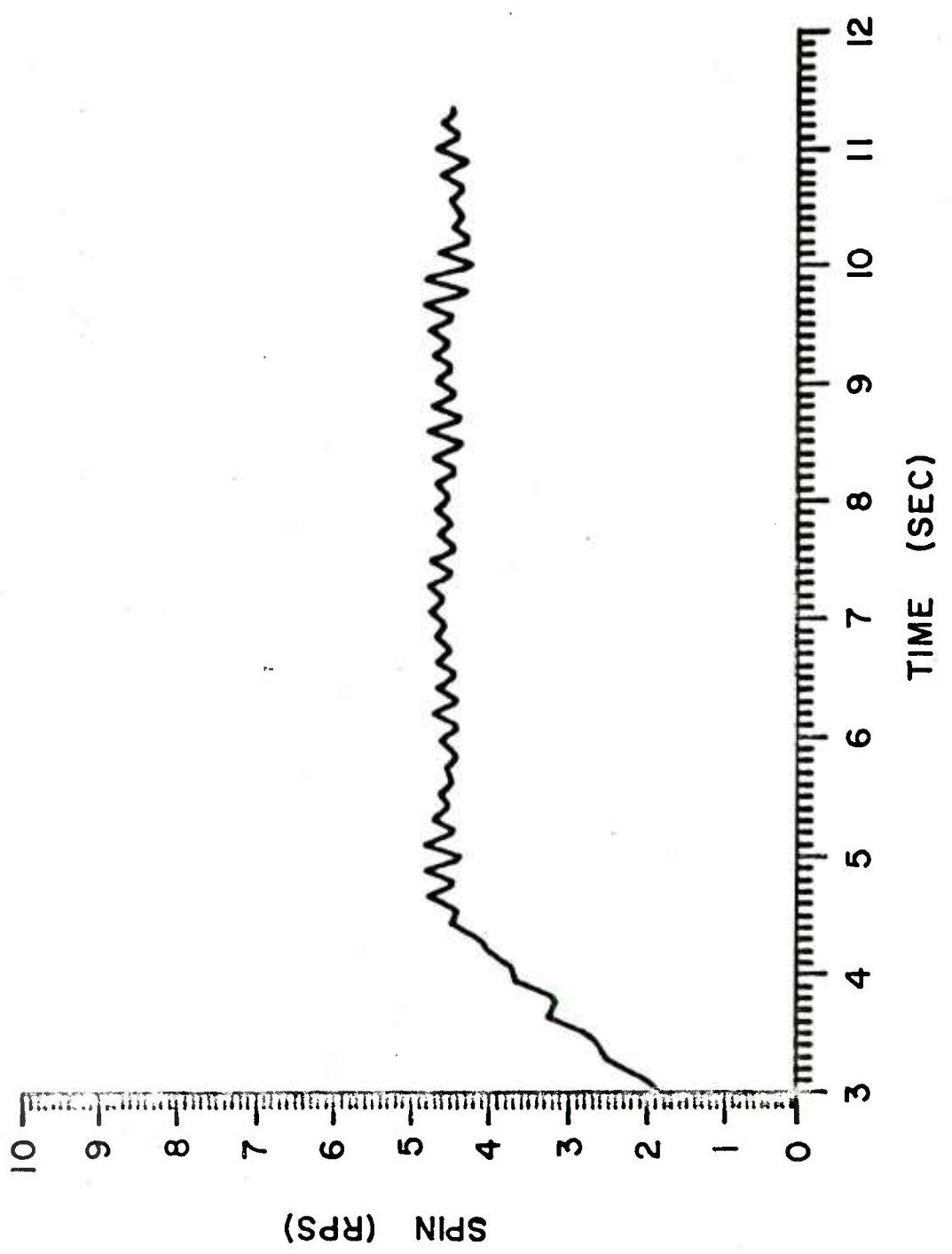


FIGURE B25. SPIN VERSUS TIME FOR CABLE DROP 28

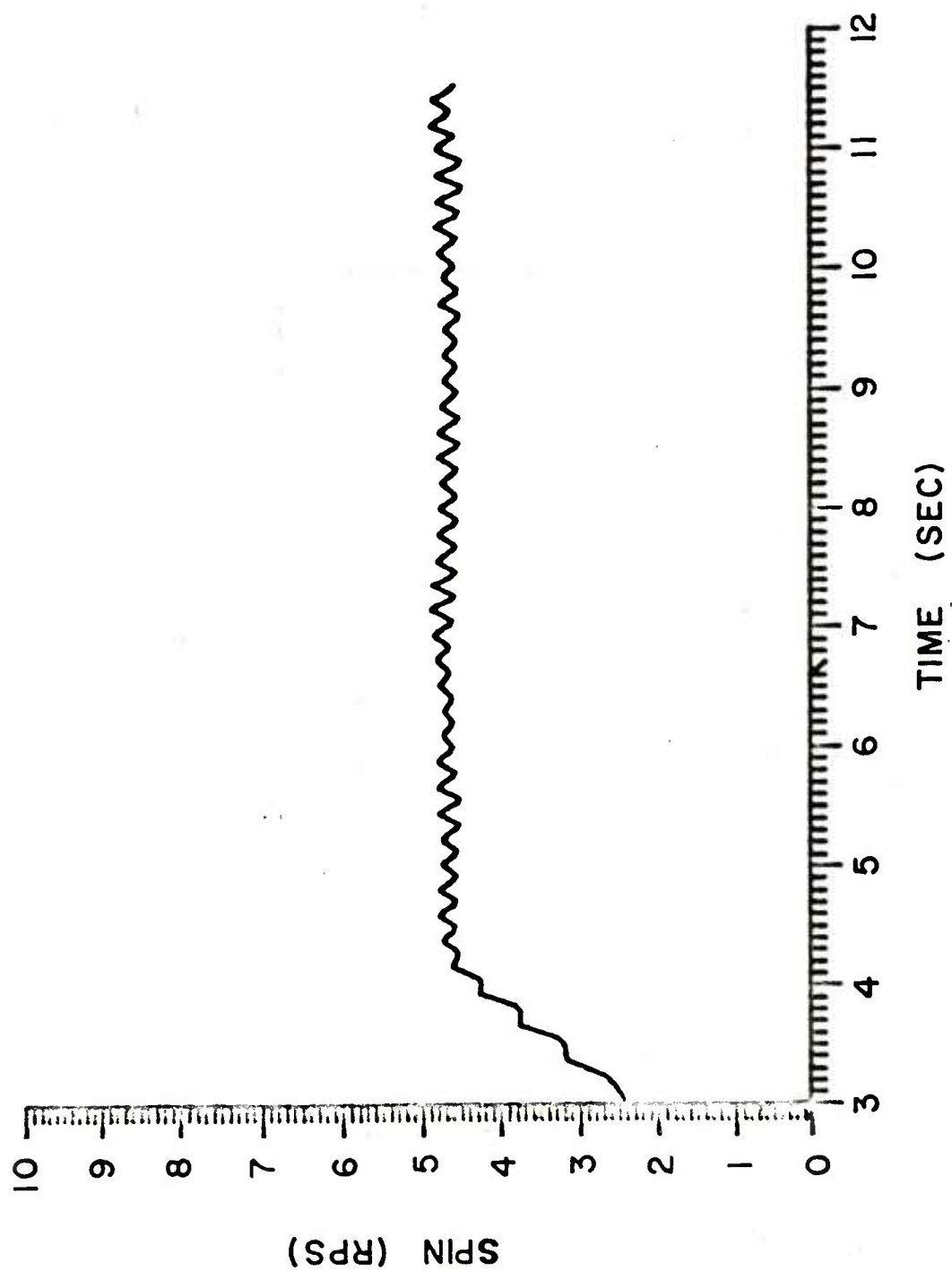
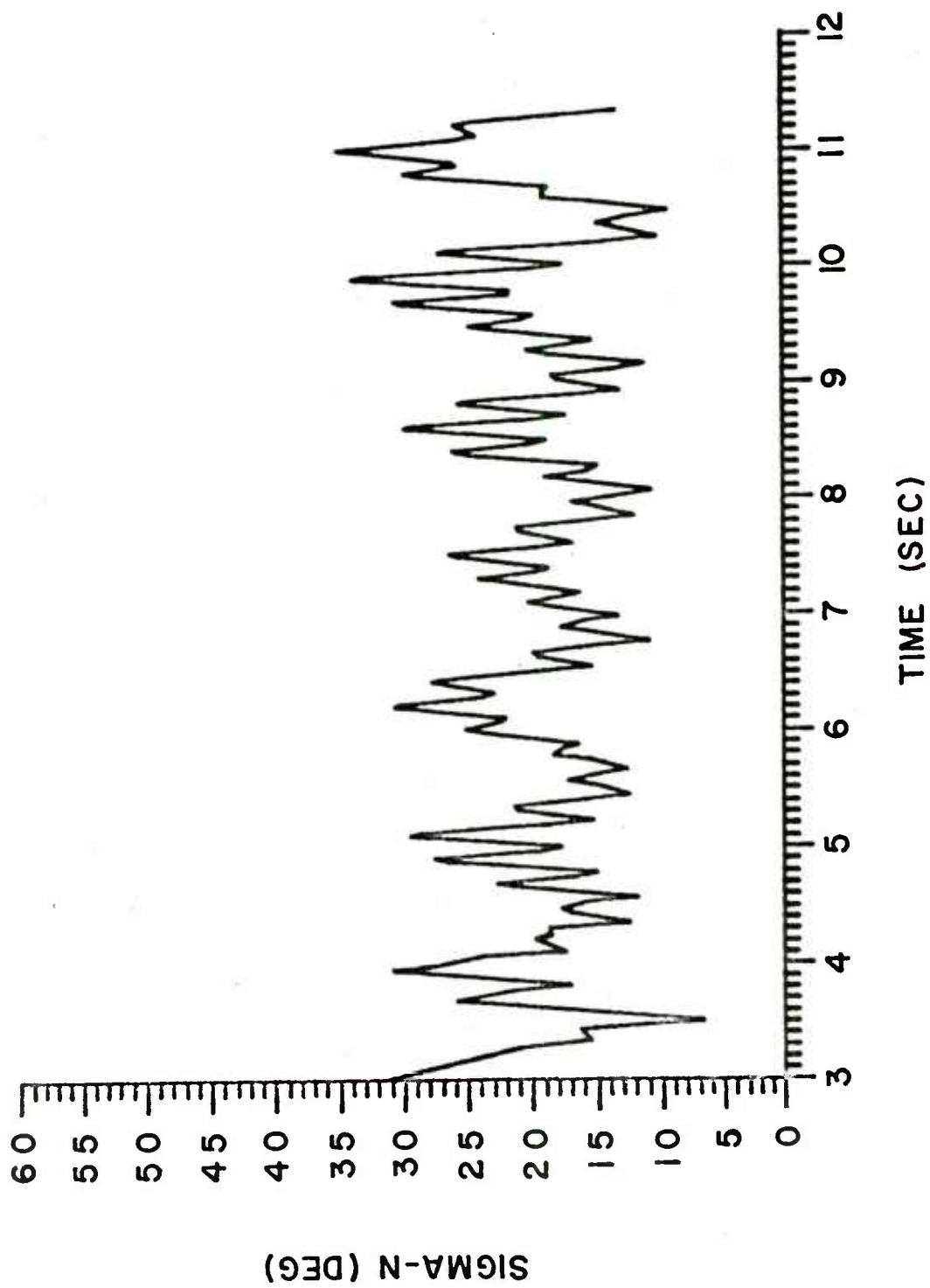
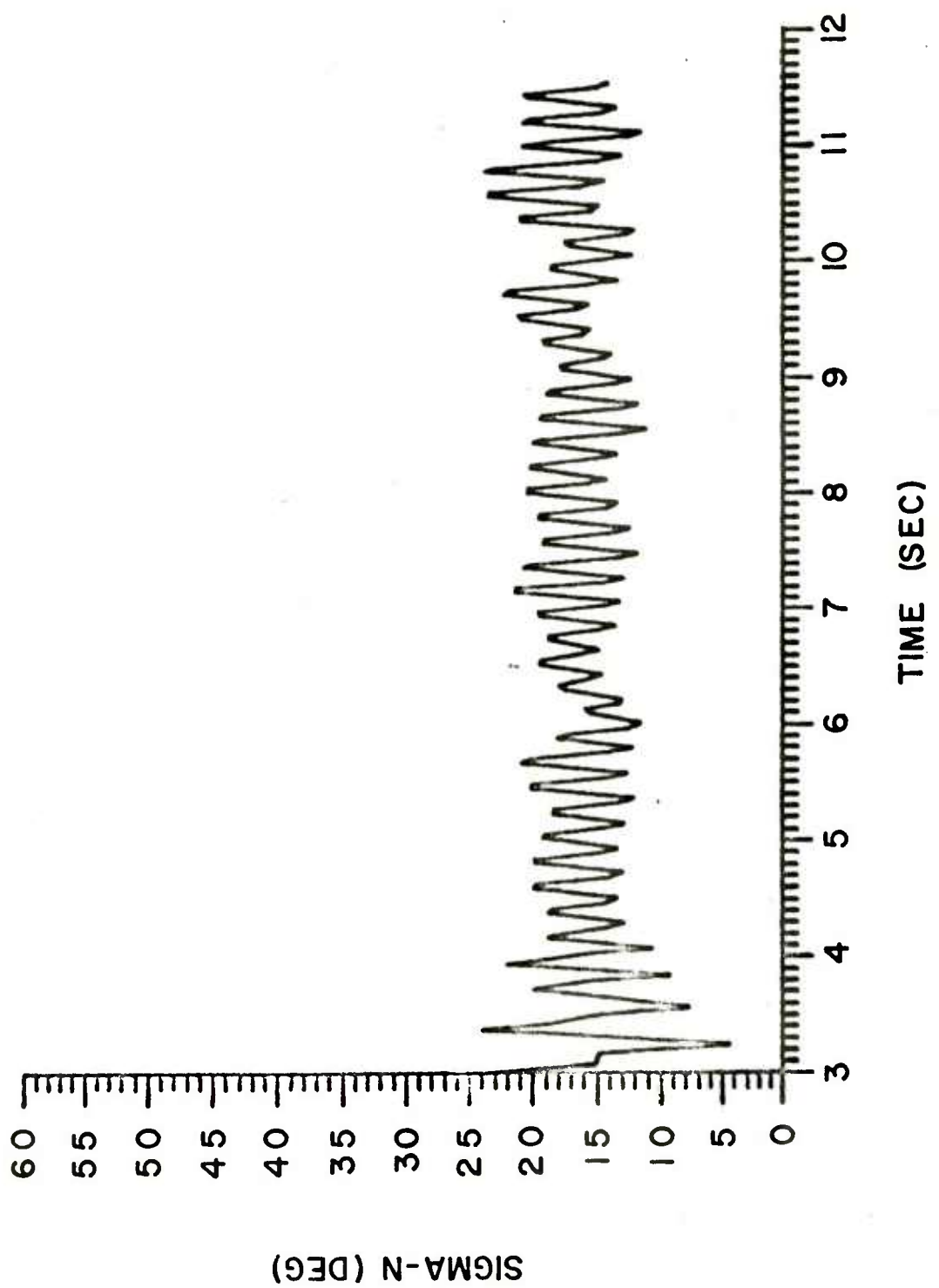


FIGURE B26. SPIN VERSUS TIME FOR CABLE DROP 30





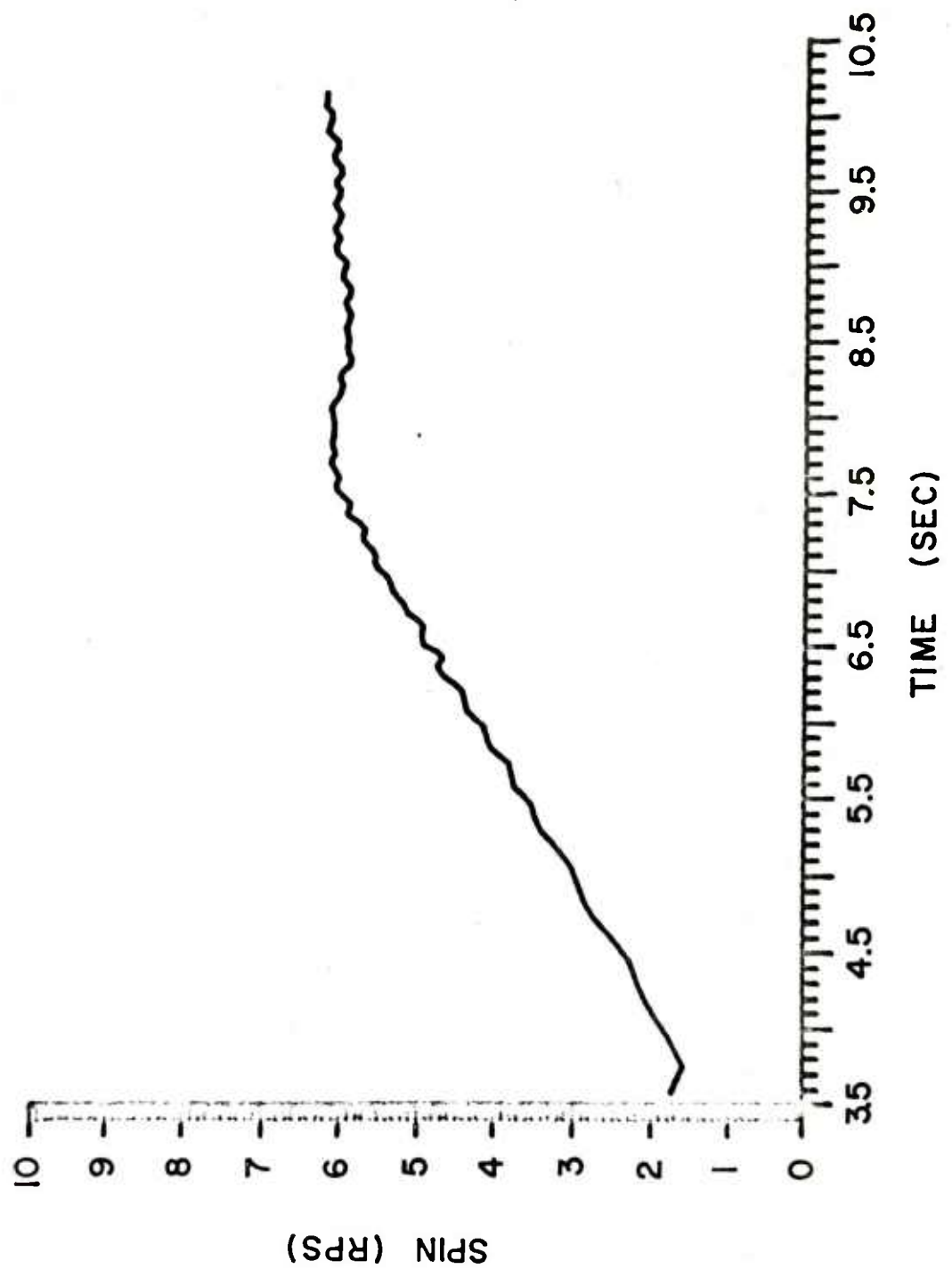


FIGURE B29. SPIN VERSUS TIME FOR CABLE DROP 25

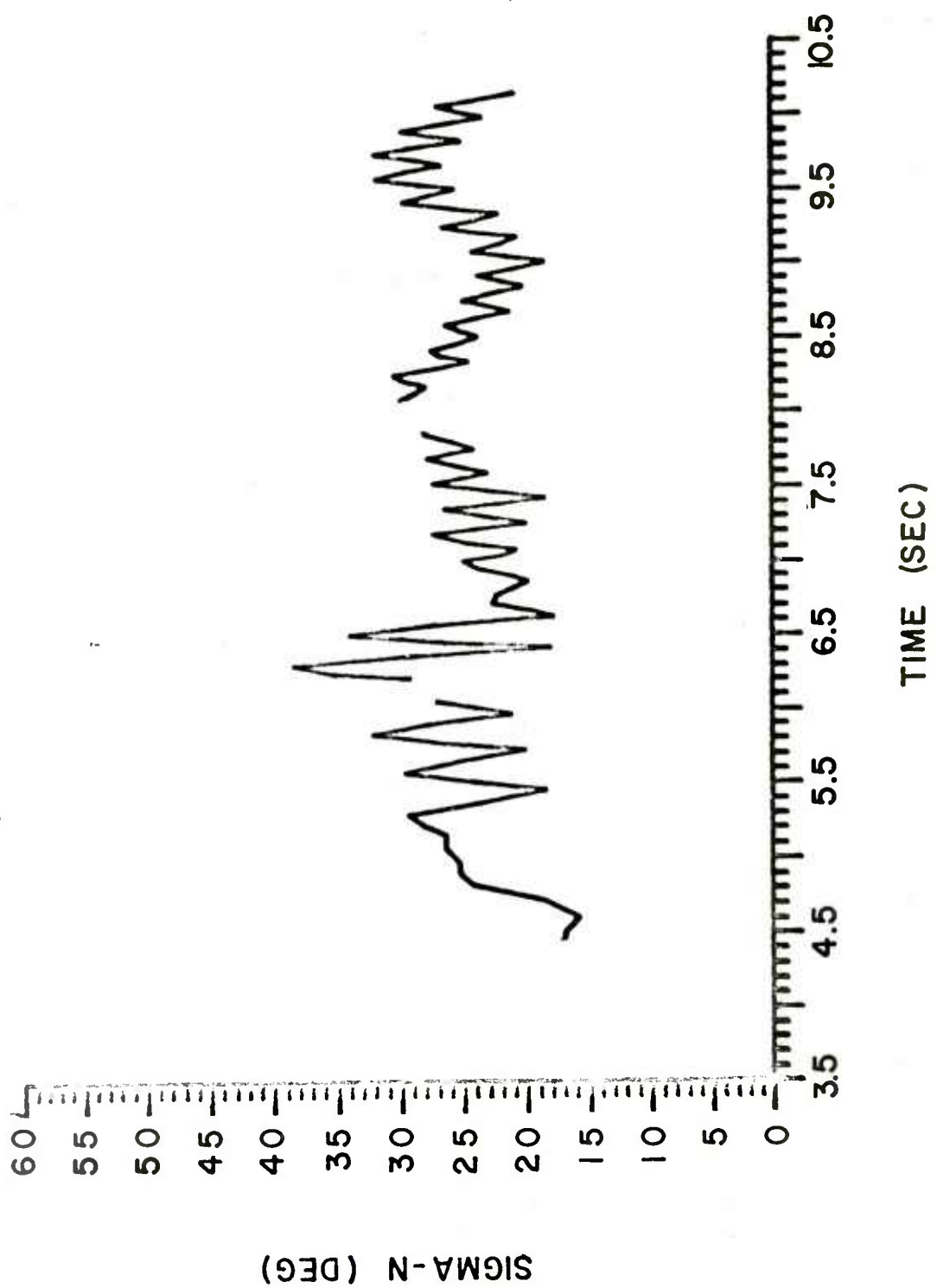


FIGURE B30. YAW VERSUS TIME FOR CABLE DROP 25

APPENDIX C

TESTCASES FOR RESONANT MOTION

A number of test cases had been developed to test Murphy's algorithm for use with the data from the first SADARM drop test program². These test cases did not address the problem of pitch rate equal to spin rate. Such motion was observed on the second test series and the validity of the results were determined by a new set of test cases designed to exercise the algorithm under pitch rate equals spin conditions. The data from the second test differed from the data of the first test series in still another way. The motion observed in the first tests showed a single mode of yawing motion. The second series of tests gave results which indicated bi-modal motion with a fast and a slow frequency present. The test case generator was modified to include bi-modal behavior. Finally, the second test series used canisters instrumented with spin sensors. These sensors produced spin data which also show a modulation of the spin at the average spin rate. The sensitivity and accuracy of these spin sensors will also be reviewed in this appendix.

A spectral analysis of the yaw data from selected drop tests with 2.13 m VRP showed the fast frequency to be about 4.8 Hz and the slow frequency to be about 1.25 Hz. The spin rate was about 4.7 rps on the average. The peak-to-peak amplitudes of slow and fast modes were about 5 degrees each. There were minor fluctuations in the amplitude during the drops. The values used in the test cases were selected to come close to the flight test conditions. The complementary solar aspect angle, SIGMA-N was made to vary as an exponentially damped periodic function:

$$\sigma_N = \pi/2 - e^{-at} \sigma_f \cos \omega_f t - \sigma_s \sin \omega_s t - \sigma_c \quad (C1)$$

where a is a constant damping coefficient, σ_f and σ_s are the fast and slow aspect angle values, ω_f and ω_s are the fast and slow circular rates, and σ_c is a constant aspect angle simulating the solar altitude.

Similarly, the roll rate (or PHI-DOT) was allowed to vary in a periodic manner:

$$\dot{\phi} = 1/(\tau_o \sin \omega_\tau t + \tau_c) \quad (C2)$$

where τ_o is a constant roll period amplitude, τ_c is a constant period simulating the steady-state roll period, and ω_τ is the circular rate of change of roll period.

Equations C1 and C2 were used to compute the times at which each sensor observes the sun for the computed amplitudes of aspect angle and roll period. The following procedure was used. The denominator of C2

is the roll period. At each quarter roll period, $T/4$, the value of σ_N is computed and an inverse calibration (ϕ_j as a function of σ_N) is used to determine the corresponding value of ϕ_j . The time at which the j th sensor observes the sun is then

$$t_j = \left[(\phi_j - \phi_{j-1})/2\pi \right] \cdot T + \text{elapsed time} \quad (C3)$$

The times generated in this manner are then used as inputs for the test cases for Murphy's algorithm, along with an idealized calibration curve.

The following types of test cases were used to evaluate the performance of Murphy's algorithm at resonant conditions: (1) constant $\dot{\phi}$, single-arm yawing motion; (2) constant $\dot{\phi}$, two-arm yawing motion; (3) variable $\dot{\phi}$, two-arm yawing motion; (4) a case with parameters equal to those of helicopter drop 10. In all the test cases, the yaw amplitude was kept small, in the order of 5 to 10 degrees, to match the flight conditions.

Test Case 1

Test case 1 was considered the simplest resonant condition. The roll rate was held constant and a single mode yawing motion was assumed. The roll rate was set at 5 rps and the circular rate of motion was 5 Hz (10π radians per second). The yaw amplitude was a constant 5-degree amplitude cosine function. Murphy's algorithm was used with the assumptions that (1) σ was linear and ϕ quadratic, (2) σ was quadratic and ϕ linear, and (3) both ϕ and σ were quadratic functions of time.

Figure C1 shows the result of the linear σ , quadratic ϕ assumption under simple resonant conditions. The dashed curve is the reference yawing motion while the solid curve represents the output of the algorithm. The points at which the algorithm evaluated the yawing motion are shown by circles. As is seen in the figure, the algorithm performs poorly under the assumption that ϕ is quadratic when it is actually constant. The probable error of this fit was 1.7 degrees showing that some evaluated points matched the reference motion while other points were far off. A much better result is obtained with the assumption that σ is quadratic and ϕ linear. This result is seen in Figure C2. The algorithm is more successful in this case because the linear assumption on ϕ more closely represents the actual constant ϕ behavior. The probable error of fit was 0.9 degree. It should be pointed out that, despite the good fit, an erroneous evaluation of the motion can be made by simply connecting the fitted points as was done in the figure. Since the yaw amplitude is sampled and averaged at about the spin rate, a dense set of measurements is not available. Thus, the algorithm simply provides values of yaw at discrete times, not all values of yaw. Simply connecting the points, as was done in Figure C2, gives the impression that the motion was a sawtooth curve which is clearly not the case. Figure C3 shows the

result of assuming that both σ and ϕ varied quadratically over the measurement interval. This result, as might be expected, lies between the first two assumptions and the degradation in fit (probable error is 1.0 degree) is due to the quadratic assumption on ϕ .

Test Case 2

Test case 2 was designed to provide the algorithm with a two-arm motion consisting of a fast and a slow frequency. The fast frequency was resonant with a spin rate which was held constant at 5 rps. Thus, the fast yaw rate was set at 10π radians/second while the slow rate was 1 Hz (2π radians/second). The slow-mode amplitude was a constant 3-degree sine wave with a constant amplitude 5-degree cosine function superposed for the fast mode. Again, the three different assumptions on the behavior of ϕ and σ were used with Murphy's algorithm.

Figure C4 shows the result of using the σ linear, ϕ quadratic assumption. As was true with test case 1, the motion is not well represented by this assumption. The solid curve (algorithm) is much smaller in amplitude than the dashed curve (reference). Again, there is a danger in constructing a curve from the fitted points, the open circles, because the algorithm does not provide a dense set of points. The probable error of fit for this assumption is 1.7 degrees. Figure C5 shows the result of using the assumption that σ varied quadratically and ϕ linearly over the measurement interval. The fit is much better because the assumption for linear ϕ more closely resembles the actual situation. The probable error of fit is 0.9 degree. The result of assuming that both ϕ and σ vary quadratically is shown in Figure C6. The result, again, lies halfway between the first two assumptions because of the non-linear stipulation on the form of ϕ . The probable error of fit is 1.0 degree.

Test Case 3

Test case 3 assumed the same two-arm motion as test case 2 with the added complication that the roll rate was allowed to vary. The average roll rate was set at 5 rps and was modulated by ± 0.1 rps at a circular rate of 10π radians/second. This rate is the same as the circular rate of the fast yaw mode.

Figure C7 shows the result of the linear σ , quadratic ϕ assumption. Despite the fact that the roll rate is varying in this case, the quadratic assumption on ϕ does not provide a good fit. A slight improvement is noted by the probable error of 1.45 degrees. Figure C8 shows the result of the quadratic σ , linear ϕ assumption and indicates that a linear variation in ϕ is adequate to account for the varying roll rate assumed for this test case. The probable error of fit showed an improved value of 0.6 degree. The result of the assumption that both σ and ϕ are quadratic is shown in Figure C9. The result

this time is not halfway between the first two assumptions but closer to the second assumption that ϕ had a linear variation. The probable error is 0.9 degree.

Test Case 4

Test case 4 used a two-arm motion with variable roll rate and the parameters were selected to be close to the values of helicopter drop 10. Thus, the circular rate of the fast mode was 9.4π radians/second and the amplitude was 2.5 degrees. The circular rate of the slow mode was 2.4π radians/second with an amplitude of 5 degrees. The spin was 5 rps and modulated ± 0.1 rps at a rate of 10π radians/second.

Figures C10 - C12 show the results of using Murphy's algorithm with the three different assumptions on the form of σ and ϕ . The poorest fit, again, was obtained with the σ linear, ϕ quadratic assumption with a probable error of 0.7 degree. The probable errors for test case 4 are less than for the other test cases because of the reduced amplitude of the reference motion. It would be difficult to determine by eye the difference between the σ quadratic, ϕ linear and the σ quadratic, ϕ quadratic assumptions (Figures C11 and C12). The probable errors of fit for these assumptions were 0.5 and 0.4 degree, respectively. Thus, to within 0.1 degree, either assumption could be used to handle the flight data from helicopter drop 10.

The results of fitting the spin with those three assumptions are shown in Figures C13 - C15. In each of the three cases, the spin seems to be fit well over certain times while at other times the spin seems to decay from the reference spin waveform. This is not merely an artifact of the plotting process (see Figures C14 and C15 which show erroneous points far from the peaks), but is probably due to the manner in which the algorithm selects values to start successive interval iterations. The probable errors in spin, however, are quite small being 0.02, 0.04, and 0.03 rps for the assumptions σ linear and ϕ quadratic, σ quadratic and ϕ linear, and both σ and ϕ quadratic, respectively. The significant fact is that the algorithm will converge to reasonable values of spin in a case where the spin modulation rate is equal to the yaw rate.

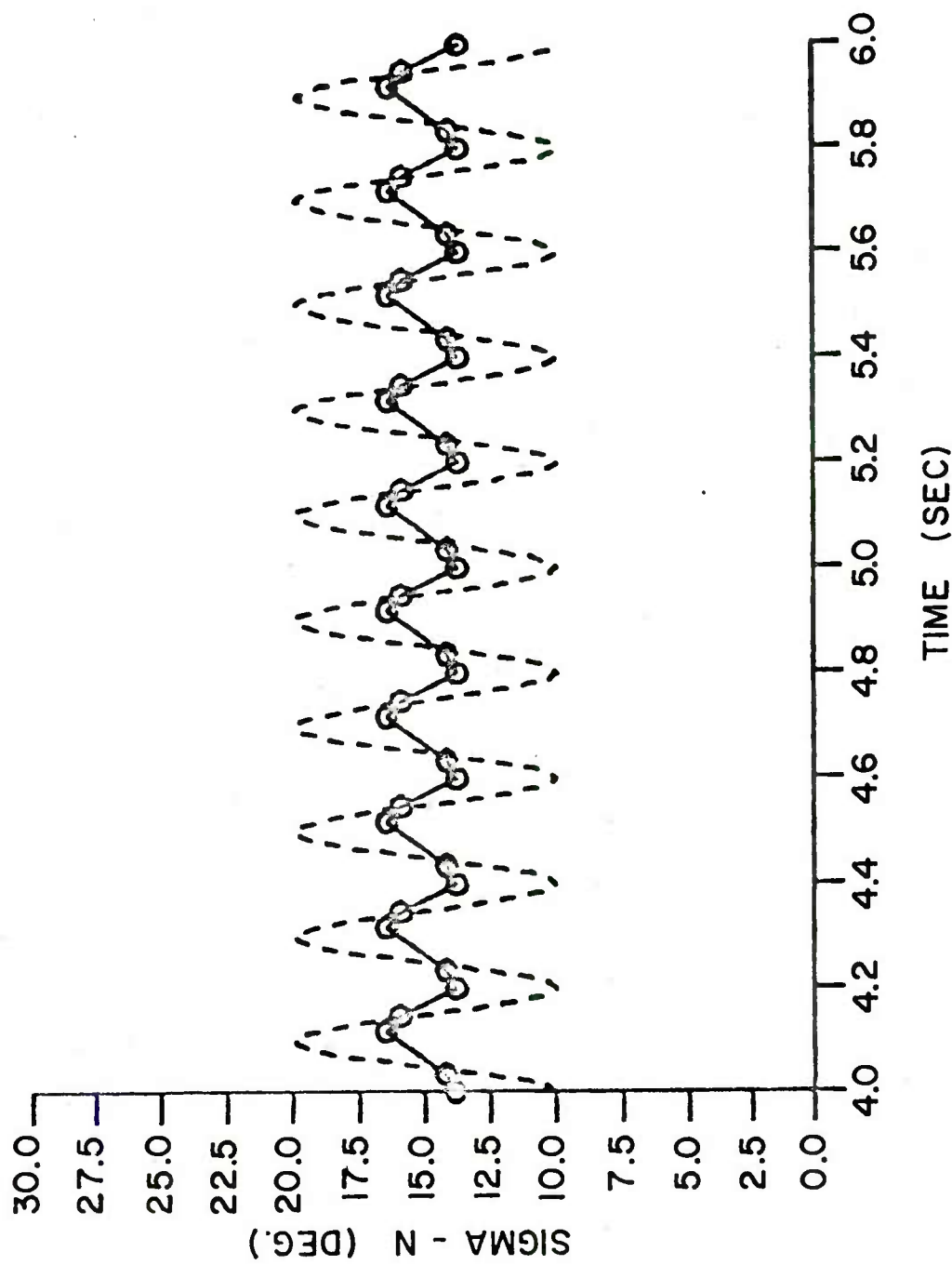


FIGURE C1. YAW VERSUS TIME - TEST CASE I (LINEAR SIGMA, QUADRATIC PHI)

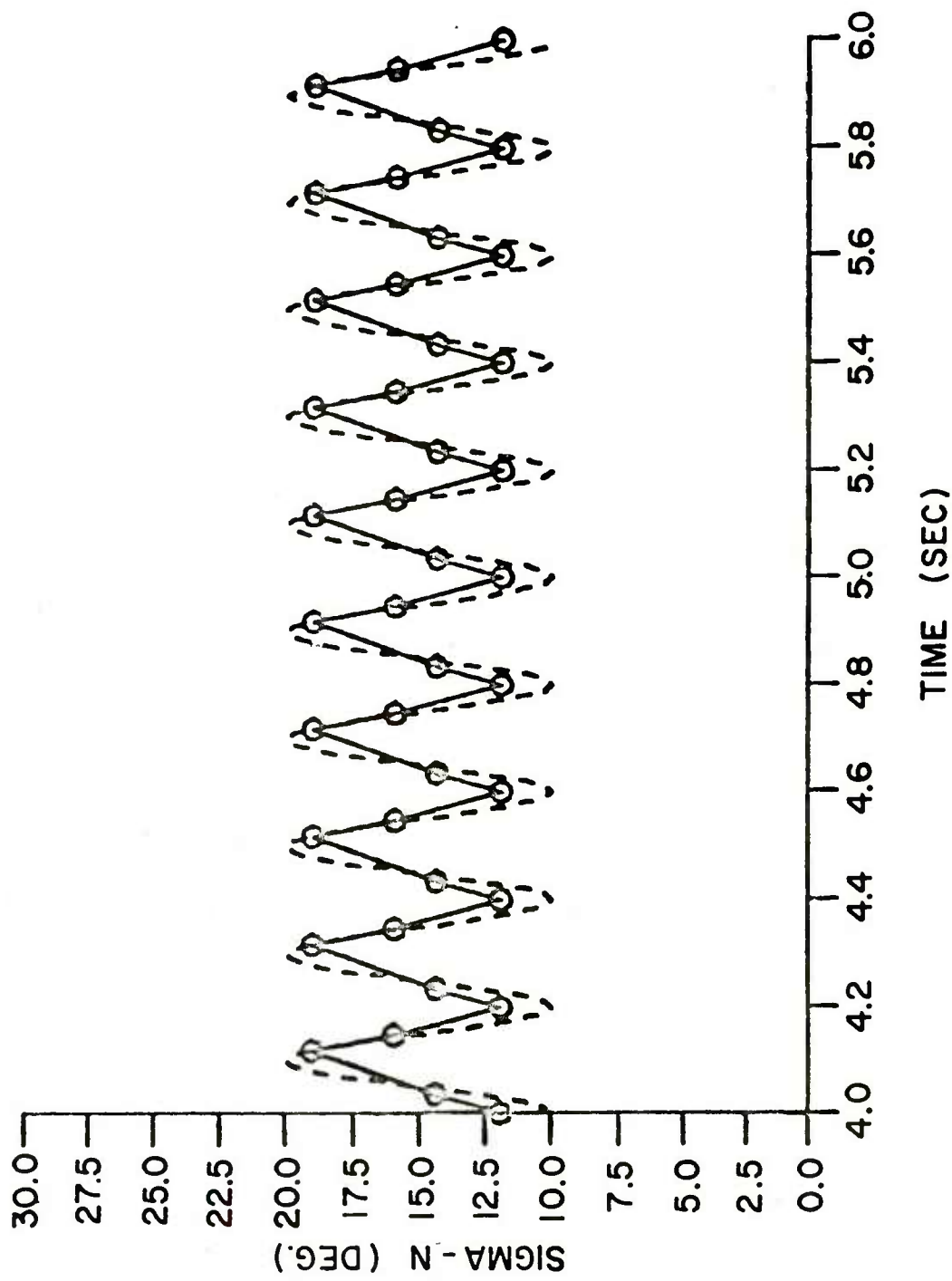


FIGURE C2. YAW VERSUS TIME - TEST CASE I (QUADRATIC SIGMA, LINEAR PHI)

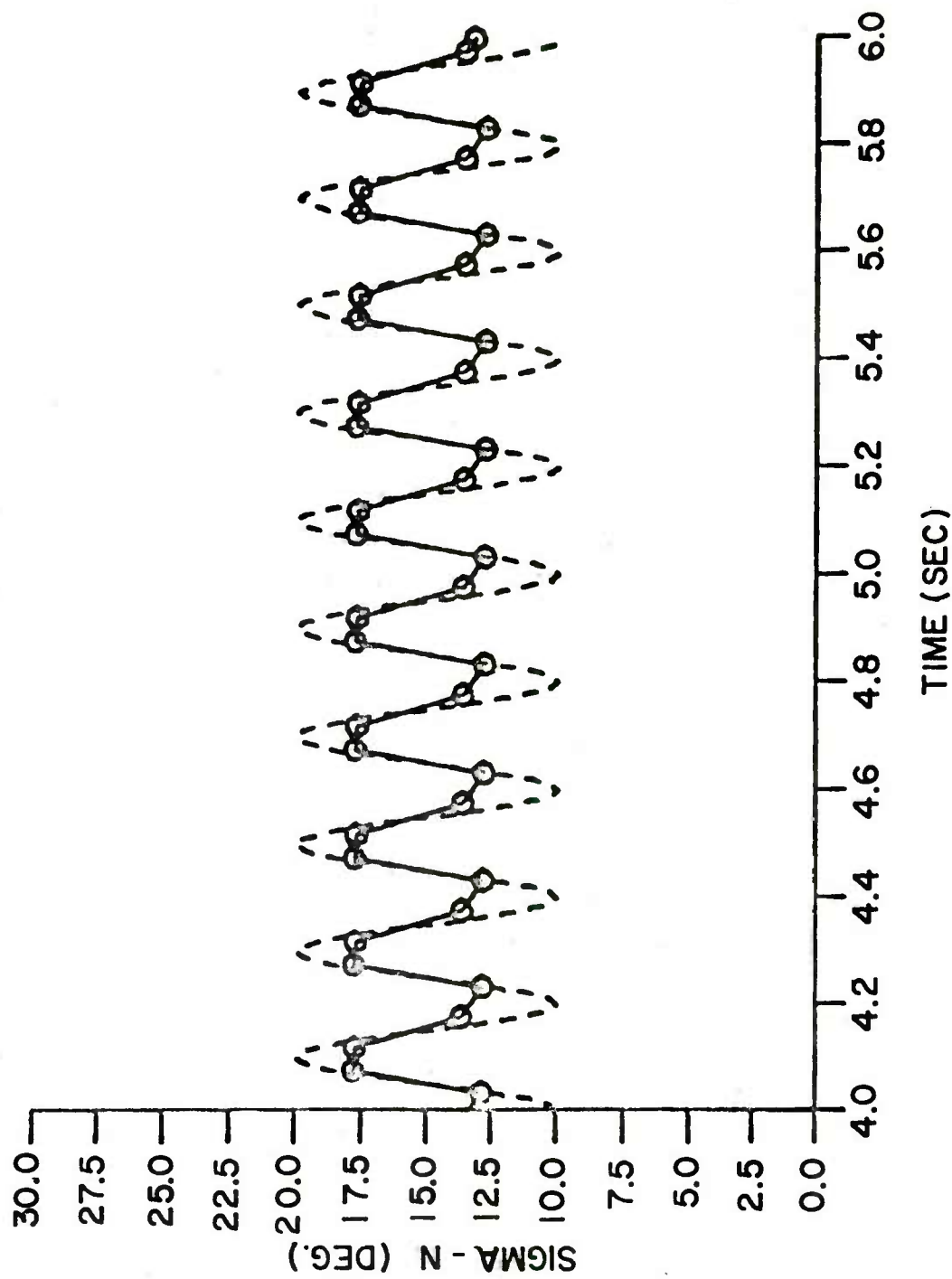


FIGURE C3. YAW VERSUS TIME - TEST CASE 1 (QUADRATIC SIGMA, QUADRATIC PHI)

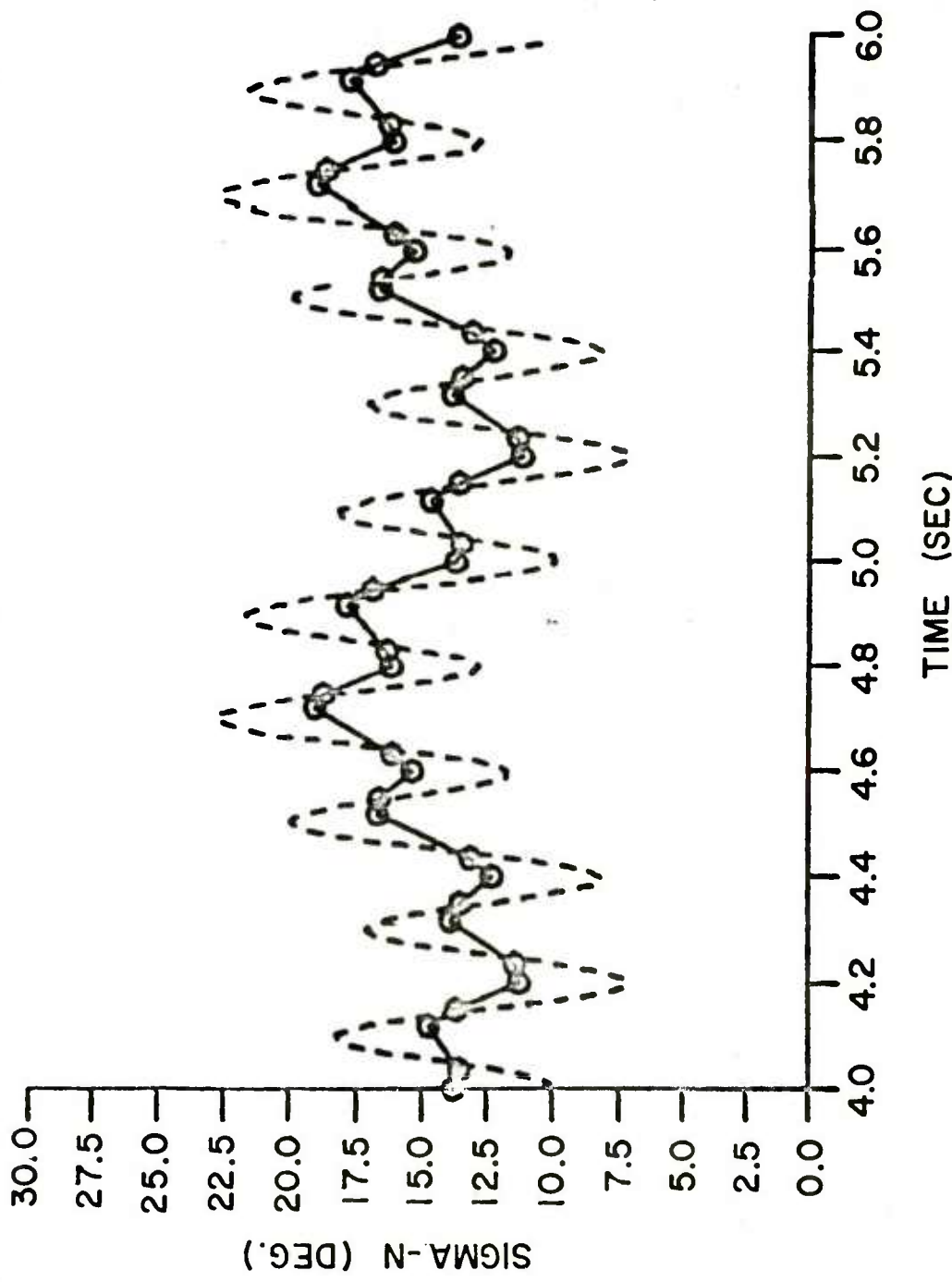


FIGURE C4. YAW VERSUS TIME - TEST CASE 2 (LINEAR SIGMA, QUADRATIC PHI)

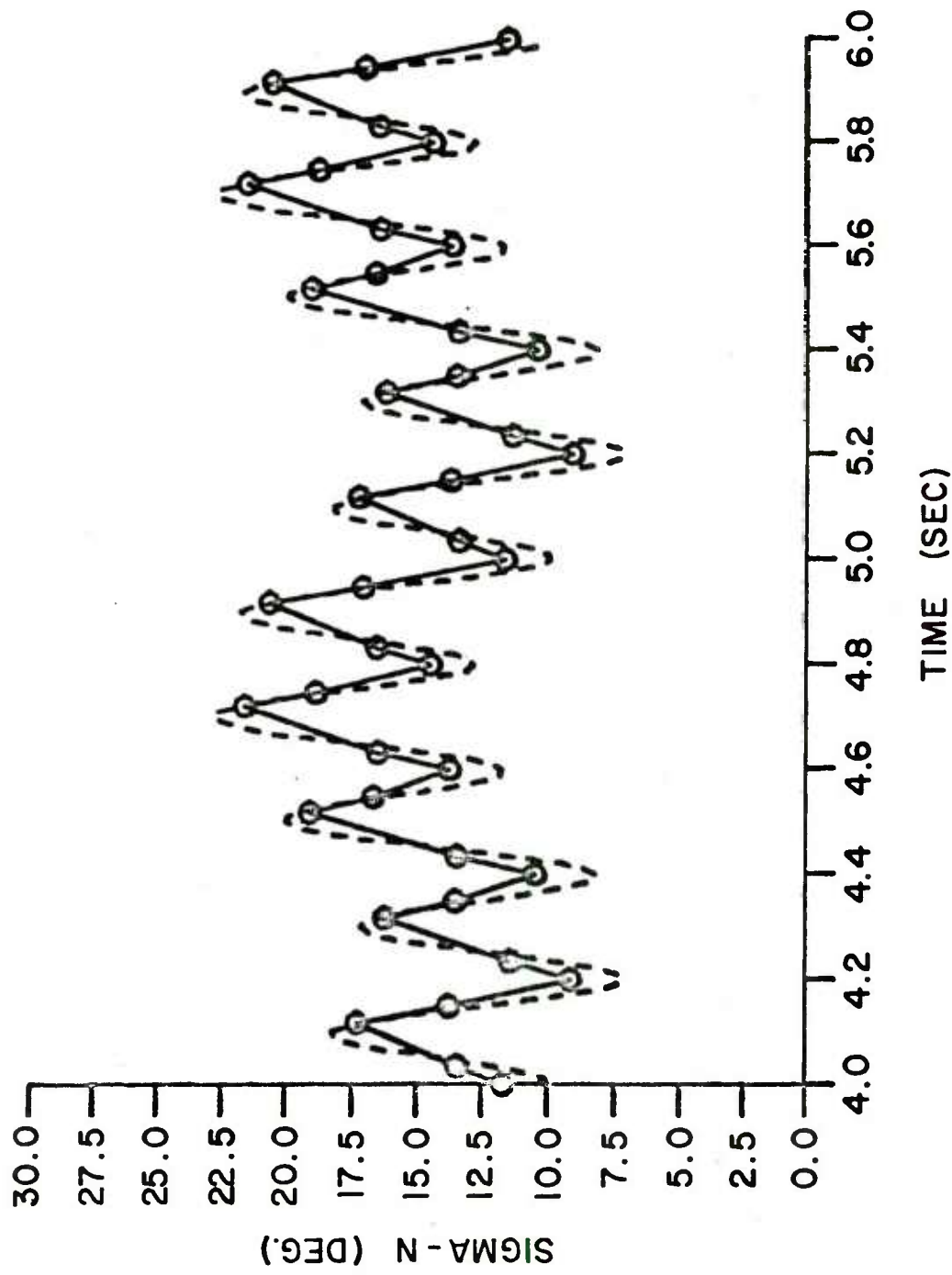


FIGURE C5. YAW VERSUS TIME - TEST CASE 2 (QUADRATIC SIGMA, LINEAR PHI)

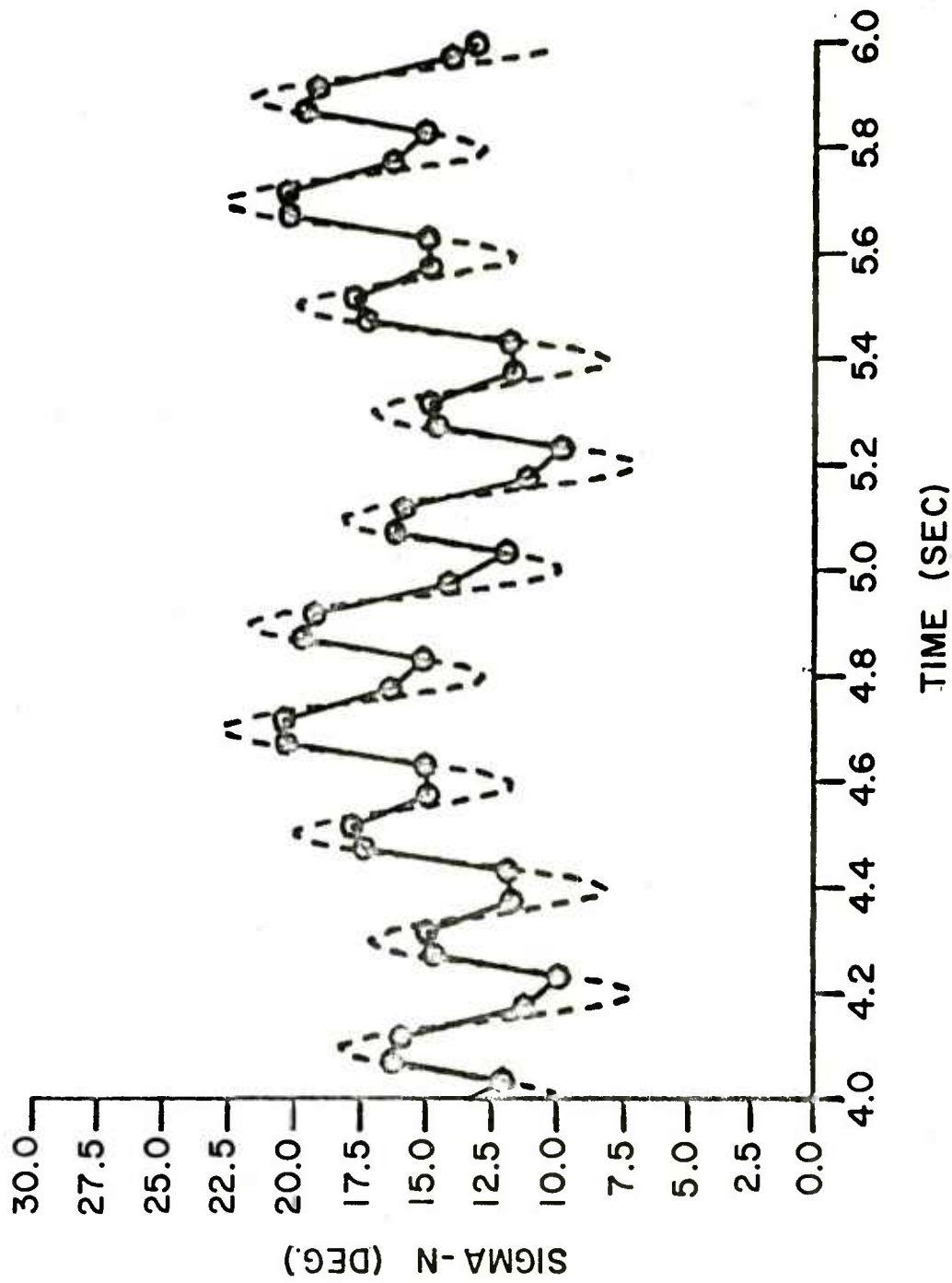


FIGURE C6. YAW VERSUS TIME - TEST CASE 2 (QUADRATIC SIGMA, QUADRATIC PHI)

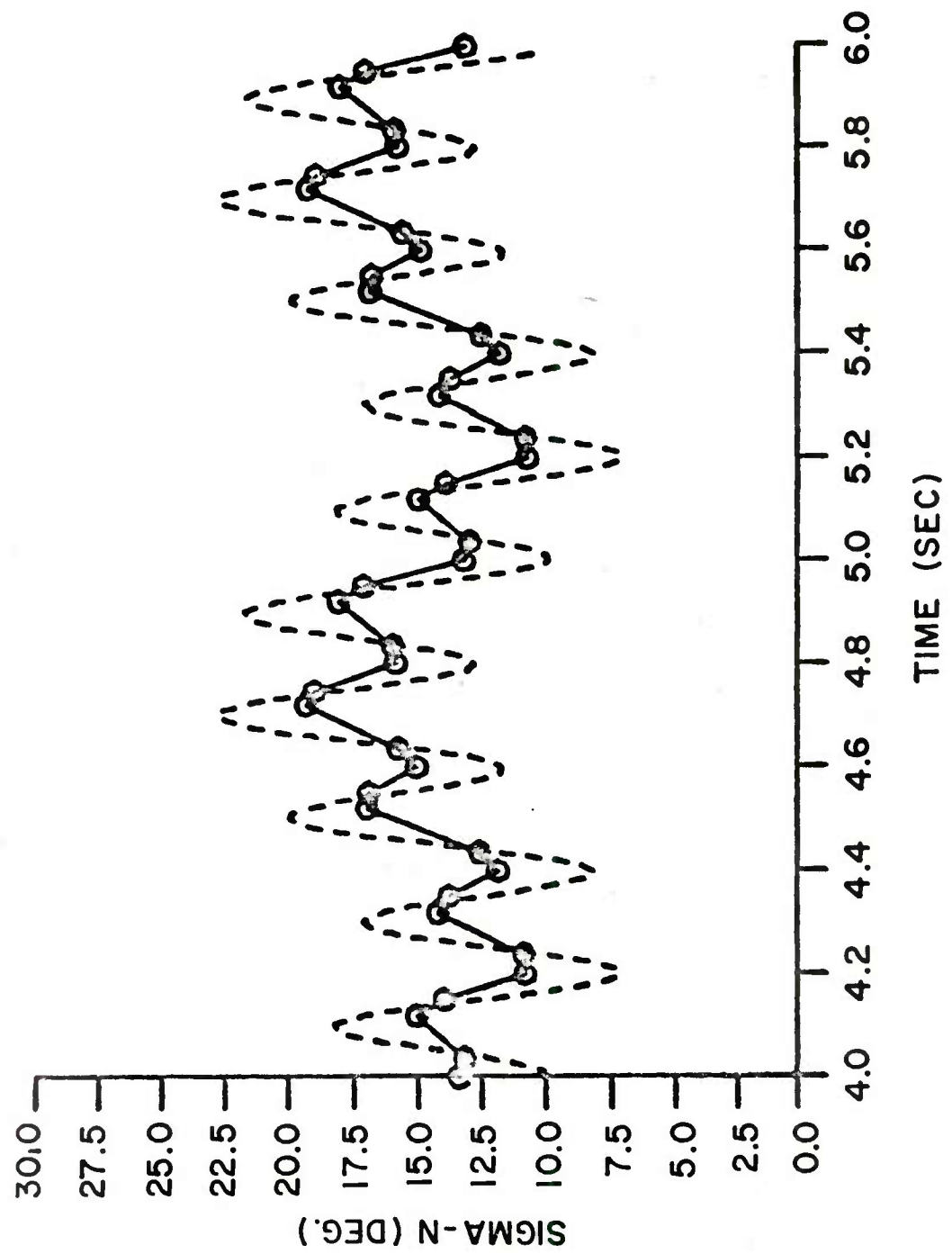


FIGURE C7. YAW VERSUS TIME - TEST CASE 3 (LINEAR SIGMA, QUADRATIC PHI)

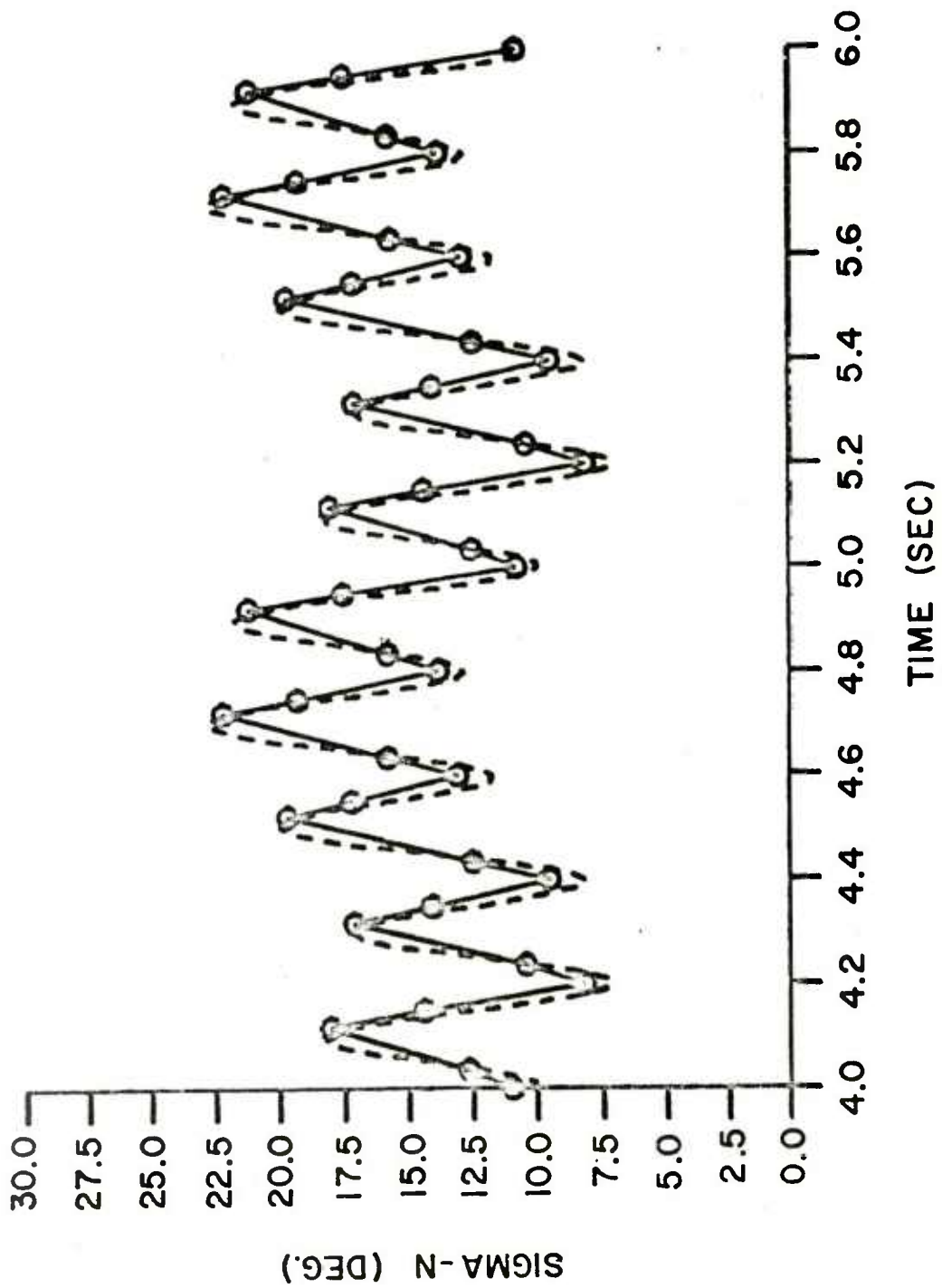


FIGURE C8. YAW VERSUS TIME- TEST CASE 3 (QUADRATIC SIGMA, LINEAR PHI)

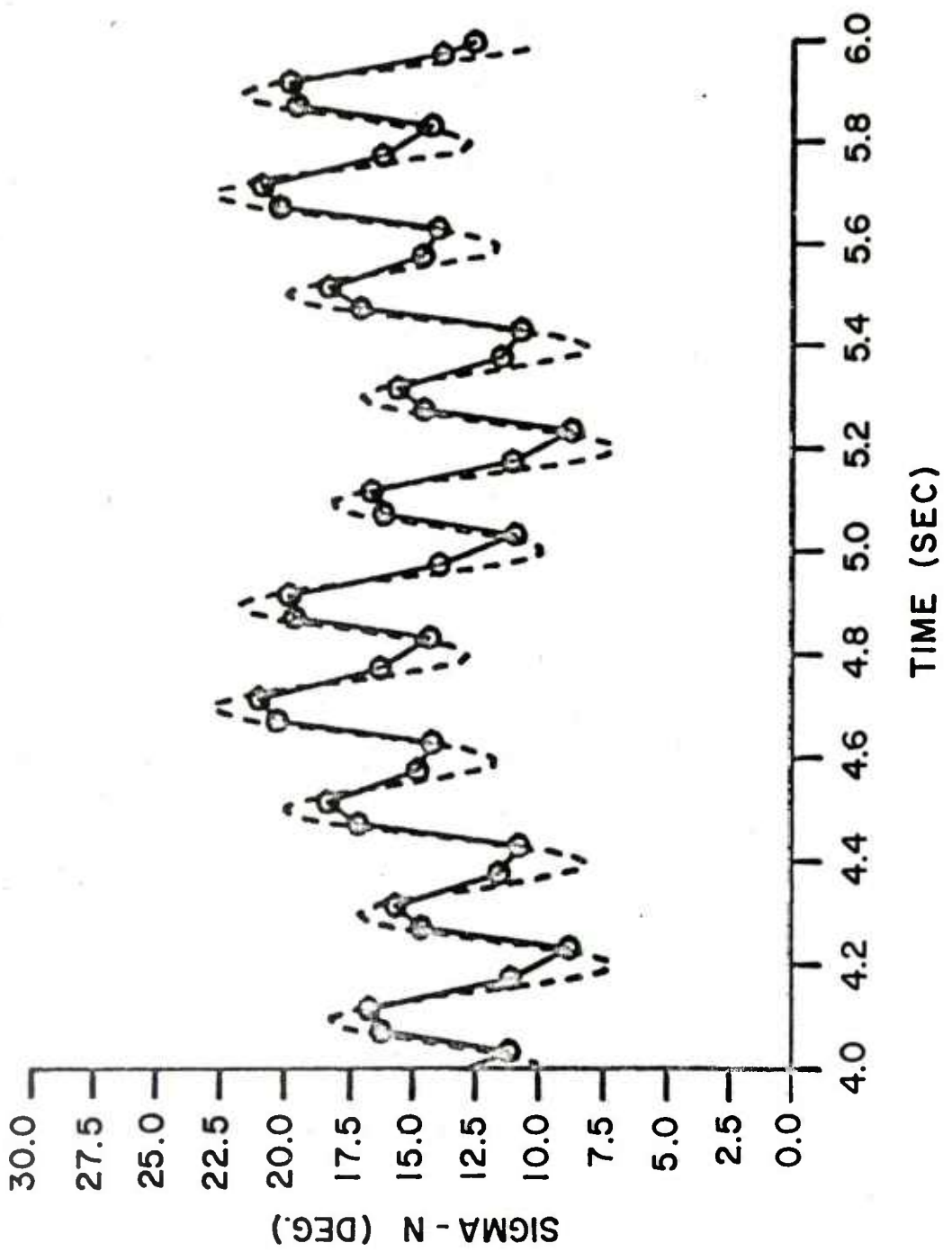


FIGURE C9. YAW VERSUS TIME - TEST CASE 3 (QUADRATIC SIGMA, QUADRATIC PHI)

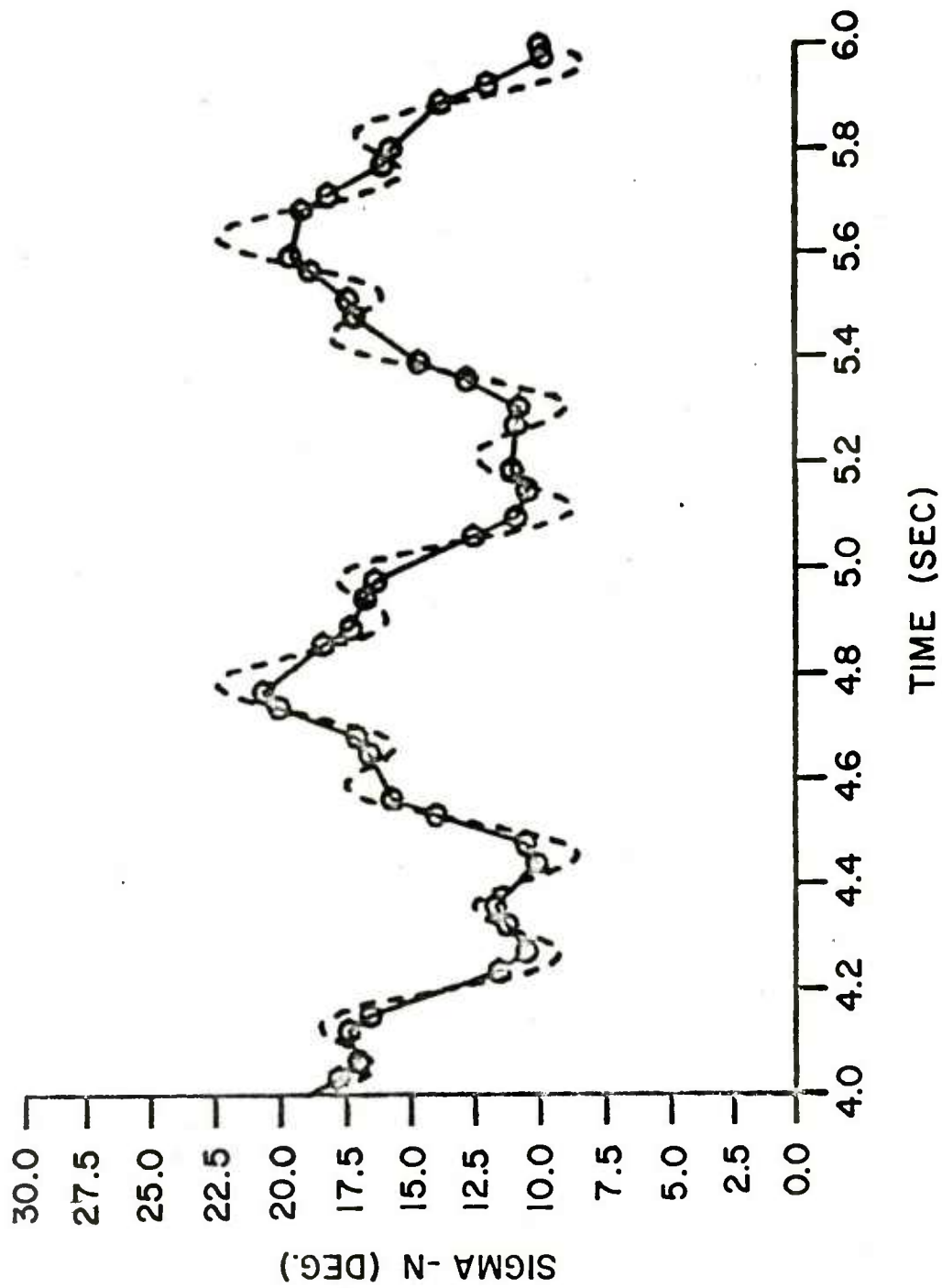


FIGURE C10. YAW VERSUS TIME - TEST CASE 4 (LINEAR SIGMA, QUADRATIC PHI)

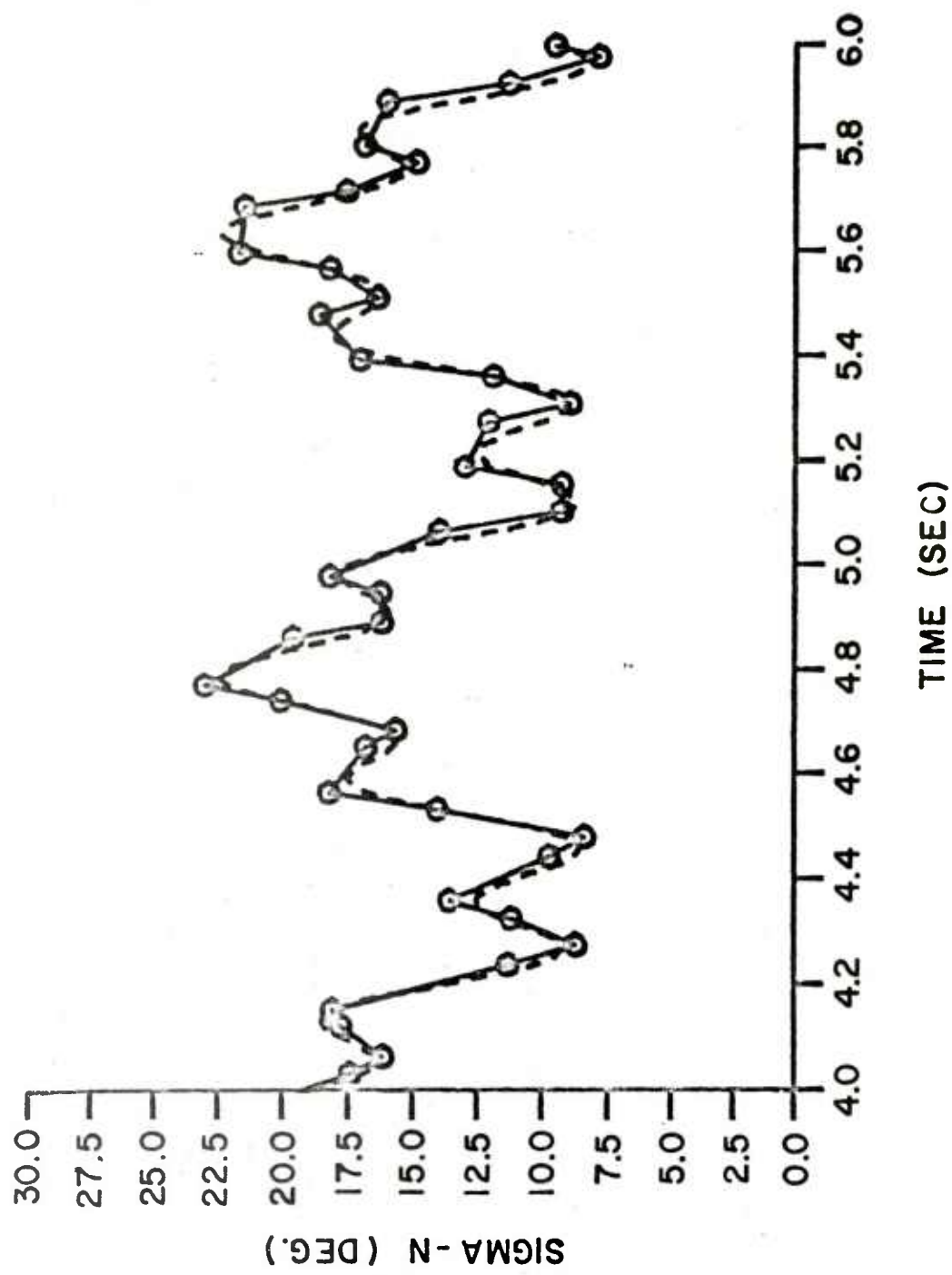


FIGURE CII. YAW VERSUS TIME - TEST CASE 4 (QUADRATIC SIGMA, LINEAR PHI)

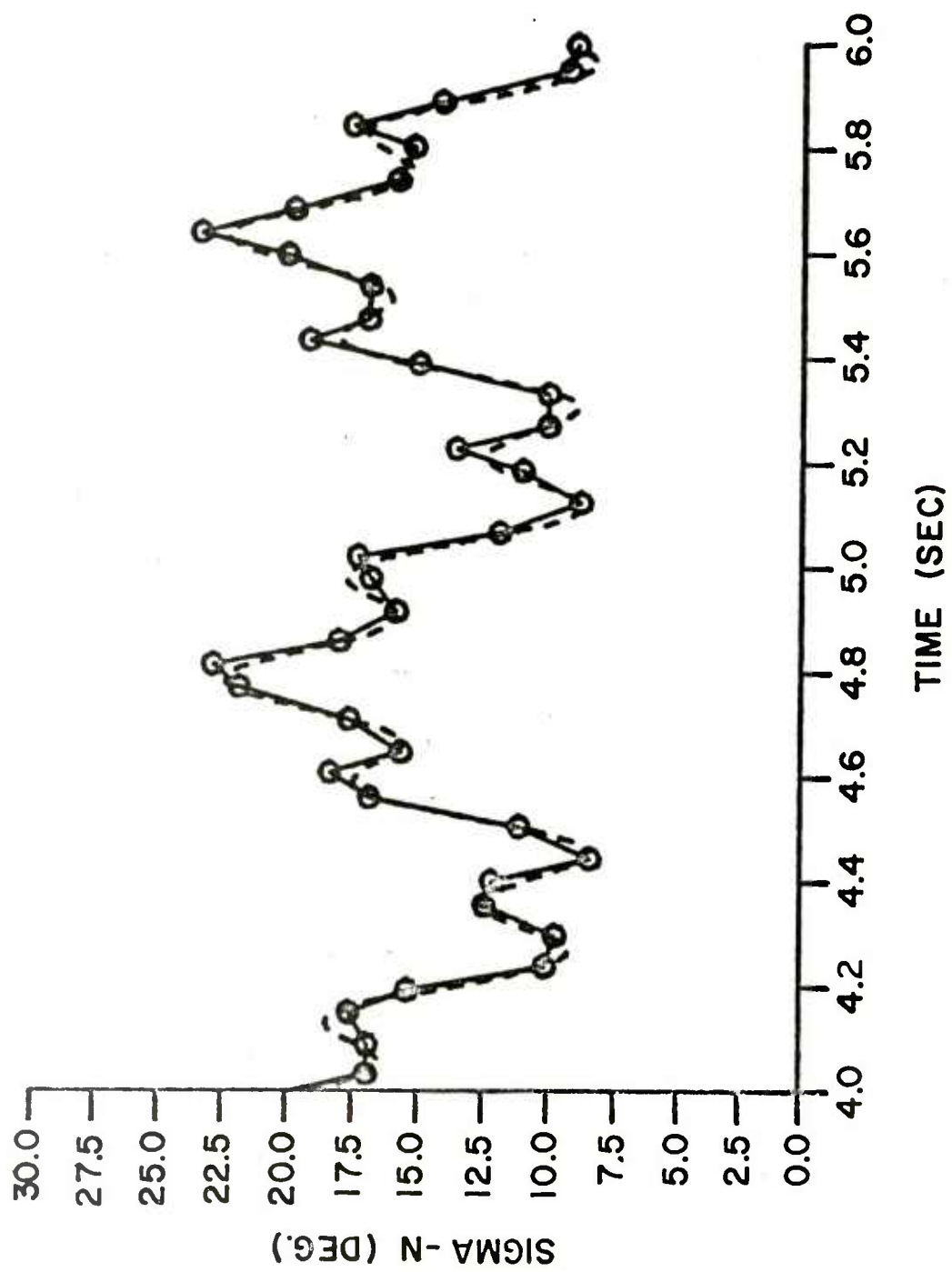


FIGURE C12. YAW VERSUS TIME - TEST CASE 4 (QUADRATIC SIGMA, QUADRATIC PHI)

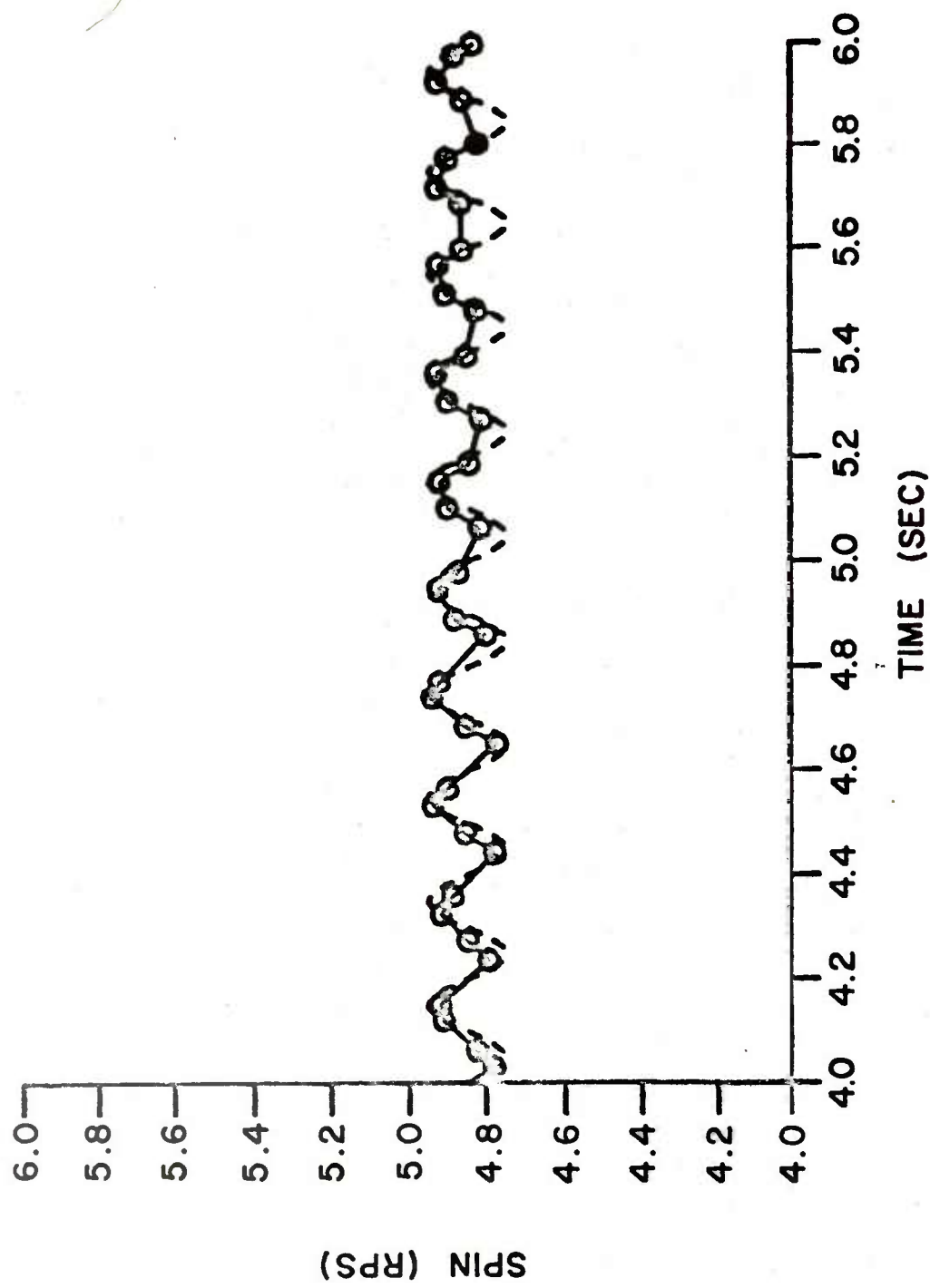


FIGURE C13. SPIN VERSUS TIME- TEST CASE 4 (LINEAR SIGMA, QUADRATIC PHI)

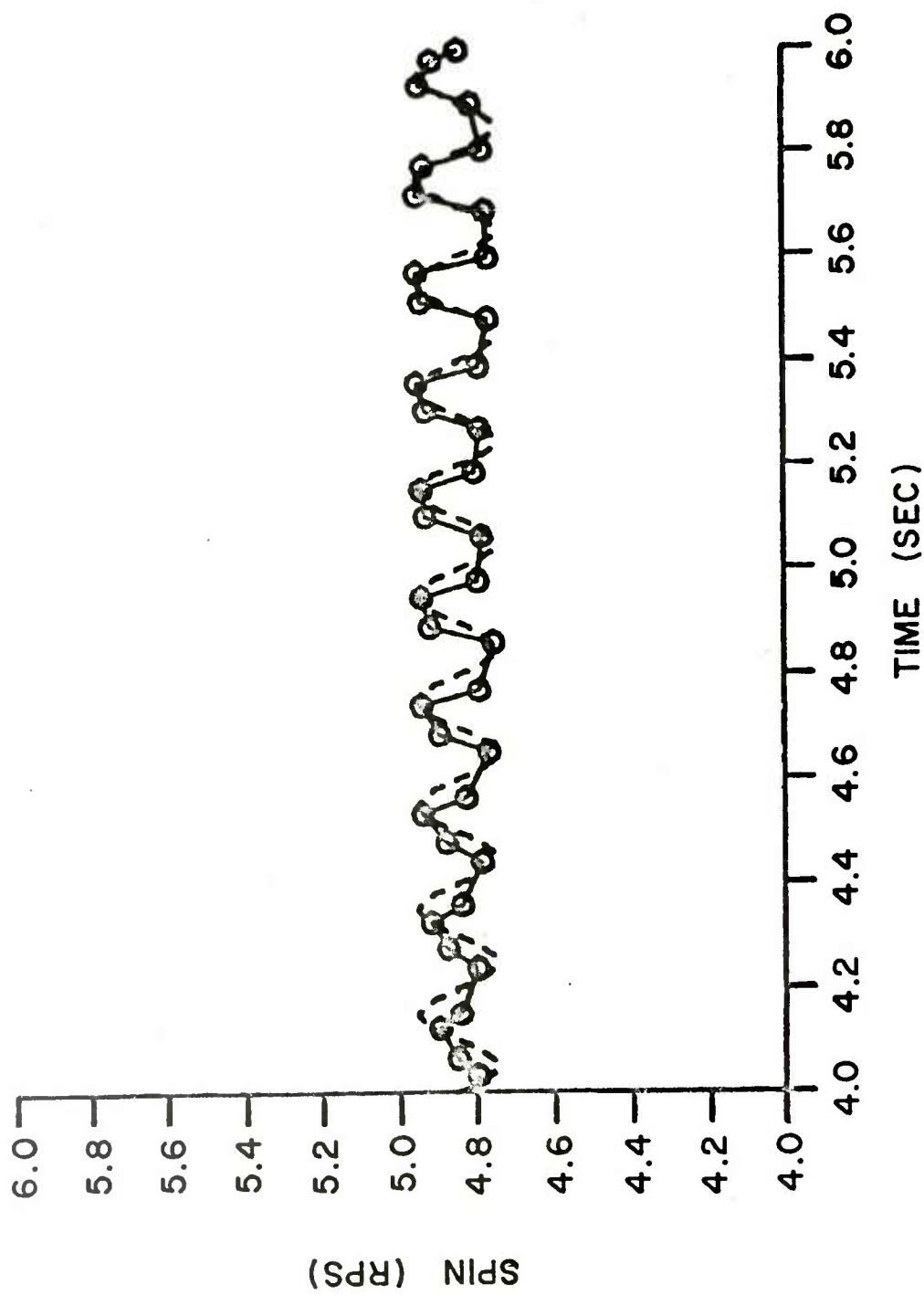


FIGURE C14. SPIN VERSUS TIME- TEST CASE 4 (QUADRATIC SIGMA, LINEAR PHI)

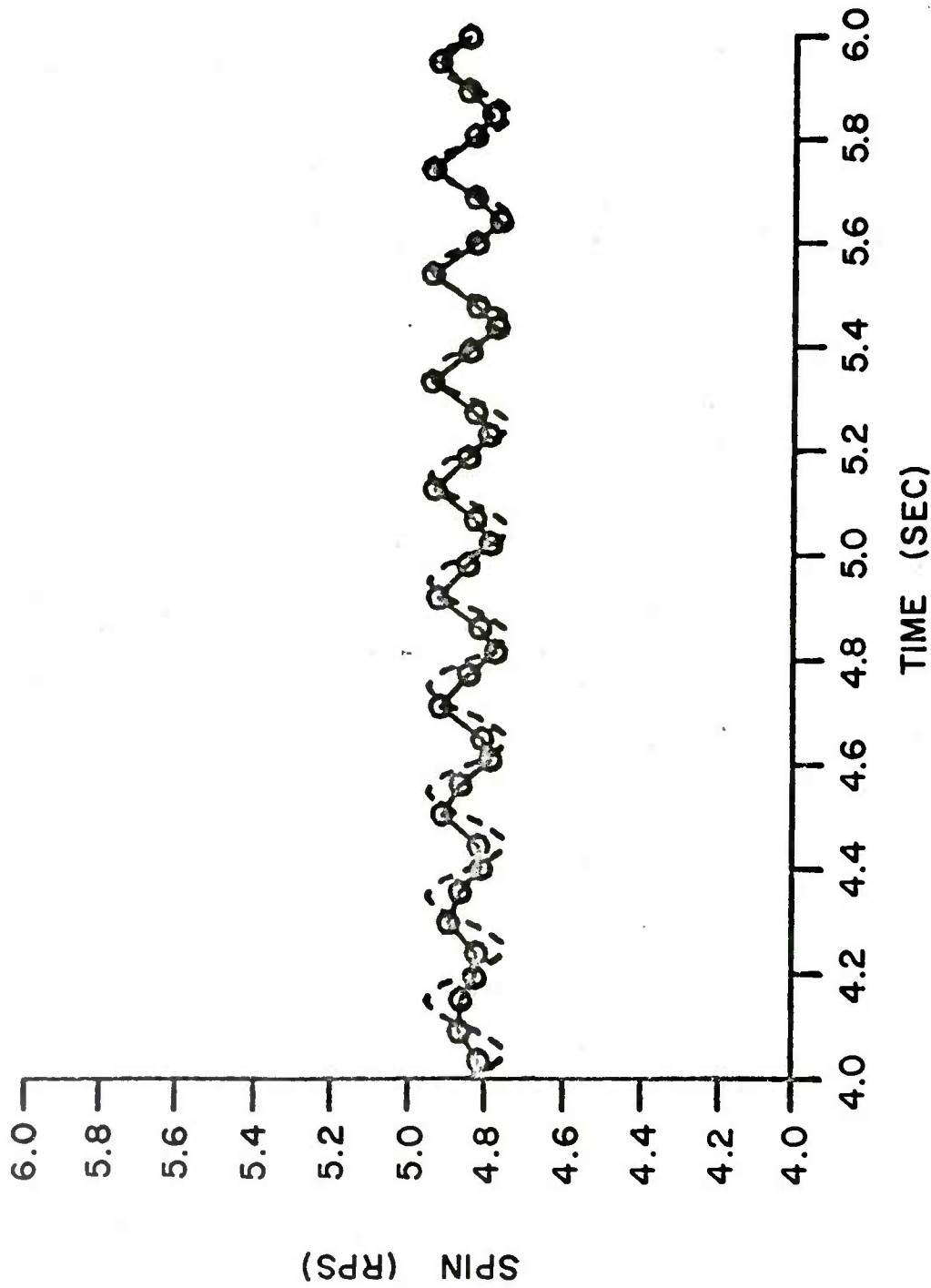


FIGURE C15. SPIN VERSUS TIME - TEST CASE 4(QUADRATIC SIGMA,QUADRATIC PHI)

DISTRIBUTION LIST

<u>No. of Copies</u>	<u>Organization</u>	<u>No. of Copies</u>	<u>Organization</u>
12	Commander Defense Technical Info Center ATTN: DDC-DDA Cameron Station Alexandria, VA 22314	2	Commander US Army Armament Research and Development Command ATTN: DRDAR-LCU-SE Mr. P. Granger Dover, NJ 07801
1	Commander US Army Materiel Development and Readiness Command ATTN: DRCDMD-ST 5001 Eisenhower Avenue Alexandria, VA 22333	1	Commander US Army Armament Materiel Readiness Command ATTN: DRSAR-LEP-L, Tech Lib Rock Island, IL 61299
2	Commander US Army Armament Research and Development Command ATTN: DRDAR-TSS (2 cys) Dover, NJ 07801	1	Director US Army Armament Research and Development Command Benet Weapons Laboratory ATTN: DRDAR-LCB-TL Watervliet, NY 12189
1	Commander US Army Armament Research and Development Command ATTN: DRDAR-LC Dr. J.T. Frasier Dover, NJ 07801	1	Commander US Army Aviation Research and Development Command ATTN: DRSAV-E P. O. Box 209 St. Louis, MO 61366
5	Commander US Army Armament Research and Development Command ATTN: DRDAR-LCA-F Mr. A. Loeb Mr. S. Wasserman Mr. D. Mertz Mr. T. Hoffman Mr. R. Kline Dover, NJ 07801	1	Director US Army Air Mobility Research and Development Laboratory Ames Research Center Moffett Field, CA 94035
1	Commander US Army Armament Research and Development Command ATTN: DRDAR-LCN Mr. J. Hathaway Dover, NJ 07801	1	Commander US Army Communications Research and Development Command ATTN: DRDCO-PPA-SA Fort Monmouth, NJ 07703
1		1	Commander US Army Electronics Research and Development Command Technical Support Activity ATTN: DELSD-L Fort Monmouth, NJ 07703

DISTRIBUTION LIST

<u>No. of Copies</u>	<u>Organization</u>	<u>No. of Copies</u>	<u>Organization</u>
1	Commander US Army Missile Command ATTN: DRSMI-R Redstone Arsenal, AL 35809	1	Director US Army TRADOC Systems Analysis Activity ATTN: ATAA-SL, Tech Lib White Sands Missile Range NM 88002
1	Commander US Army Missile Command ATTN: DRSMI-YDL Redstone Arsenal, AL 35809	1	Commander US Army Yuma Proving Ground ATTN: STEYP-TMW Mr. W.T. Vomocil Yuma, AZ 85364
1	Commander US Army Missile Command ATTN: DRSMI-RDK, Mr. R. Deep Redstone Arsenal, AL 35809	1	Commander US Army Harry Diamond Laboratories ATTN: DELHD-TA-L 2800 Powder Mill Road Adelphi, MD 20783
1	Commander US Army Jefferson Proving Ground ATTN: STEJP-TD-D Madison, IN 47250	1	Commander US Army Natick Research and Development Command ATTN: DRXRE, Dr. D. Sieling Natick, MA 01762
2	Commander US Army Mobility Equipment Research and Development Command ATTN: DRSME-RZT DRDME-WC Fort Belvoir, VA 22060	1	Commander US Army Research Office ATTN: CRD-AA-EH P. O. Box 12211 Research Triangle Park NC 27709
1	Commander US Army Tank Automotive Research and Development Command ATTN: DRDTA-UL Warren, MI 48090	1	Commander US Naval Air Systems Command ATTN: AIR-604 Washington, DC 20360
1		1	Commander David W. Taylor Naval Ship Research and Development Command ATTN: Aerodynamics Laboratory Bethesda, MD 20084

DISTRIBUTION LIST

<u>No. of Copies</u>	<u>Organization</u>	<u>No. of Copies</u>	<u>Organization</u>
1	Commander Naval Surface Weapons Center ATTN: Dr. T. Clare Dahlgren, VA 22448	3	Director Sandia Laboratories ATTN: Division 1342 Mr. W.F. Hartman Division 1331 Mr. H.R. Vaughn Mr. A.E. Hodapp Albuquerque, NM 87115
1	Commander Naval Surface Weapons Center ATTN: Code 730, Tech Lib Silver Spring, MD 20910	2	Massachusetts Institute of Technology ATTN: Prof. E. Covert Prof. C. Haldeman 77 Massachusetts Avenue Cambridge, MA 02139
1	Commander Naval Weapons Center ATTN: Code 233 China Lake, CA 93555	1	MIT/Lincoln Laboratories ATTN: Dr. Milan Vlajinac Mail Stop D-382 P. O. Box 73 Lexington, MA 02173
1	AFATL (Tech Lib) Eglin AFB, FL 32542	1	Rutgers University Mechanical, Industrial, and Aerospace Engineering Department ATTN: Dr. Robert H. Page New Brunswick, NJ 08903
1	AFELM, The Rand Corporation ATTN: Library-D 1700 Main Street Santa Monica, CA 90406	1	University of Virginia Department of Engineering Science and Systems ATTN: Prof. I. Jacobson Thornton Hall Charlottesville, VA 22904
1	Arnold Research Organization Inc. Project Support and Special Studies Section Aerodynamics Division Projects Branch ATTN: Dr. J.C. Adams, Jr. Arnold AFB, TN 37389	1	General Electric Company Armament Systems Department ATTN: Mr. R.H. Whyte Lakeside Avenue Burlington, VT 05401
1	Calspan Corporation P.O. Box 400 Buffalo, NY 14221		
2	Honeywell, Inc. ATTN: Mr. G. Stilley Mr. W. George 600 Second Street, N. Hopkins, MN 55343		

DISTRIBUTION LIST

<u>No. of Copies</u>	<u>Organization</u>
2	Aerojet Electrosystems Company ATTN: Mr. W.J. Fray Mr. D.S. McDonald 1100 W. Hollyvale Street Azusa, CA 91702

Aberdeen Proving Ground

Director, USAMSAA
ATTN: DRXSY-D
DRXSY-MP, H. Cohen
Commander, USATECOM
ATTN: DRSTE-T0-F
Dir, USACSL, Bldg. E3516
ATTN: DRDAR-CLB-PA

USER EVALUATION OF REPORT

Please take a few minutes to answer the questions below; tear out this sheet, fold as indicated, staple or tape closed, and place in the mail. Your comments will provide us with information for improving future reports.

1. BRL Report Number _____

2. Does this report satisfy a need? (Comment on purpose, related project, or other area of interest for which report will be used.)

3. How, specifically, is the report being used? (Information source, design data or procedure, management procedure, source of ideas, etc.)

4. Has the information in this report led to any quantitative savings as far as man-hours/contract dollars saved, operating costs avoided, efficiencies achieved, etc.? If so, please elaborate.

5. General Comments (Indicate what you think should be changed to make this report and future reports of this type more responsive to your needs, more usable, improve readability, etc.)

6. If you would like to be contacted by the personnel who prepared this report to raise specific questions or discuss the topic, please fill in the following information.

Name: _____

Telephone Number: _____

Organization Address: _____

